ACTur: Active Turbulent Boundary-layer Control for Skin Friction Drag Reduction

AIRBUS AIRNet funded activity at the University of Toronto

Final Report: November 2017 (M48)

Pieter D. Boom[1], Randy Belanger,[2] Ronald E. Hanson,[3]
Philippe Lavoie[4], and David W. Zingg[5]

University of Toronto Institute for Aerospace Studies
4925 Dufferin Street, Toronto, Ontario, M3H 5T6, Canada

[1]Postdoctoral Fellow, University of Toronto Institute for Aerospace Studies
[2]Doctoral Candidate, University of Toronto Institute for Aerospace Studies
[3]Assistant Professor, Lassonde School of Engineering, York University (Present Position)
[4]Associate Professor, Associate Director, University of Toronto Institute for Aerospace Studies; Associate Director, Center for Research in Sustainable Aviation
[5]University of Toronto Distinguished Professor of Computational Aerodynamics and Sustainable Aviation; Director, Center for Research in Sustainable Aviation; Director, Center for Computational Science and Engineering

Executive Summary

Reducing aircraft fuel burn can have a positive impact on the long term economic and environmental sustainability of commercial aviation. Fuel burn is directly related to drag. A large percentage of aircraft drag comes from skin friction, most of which comes from the turbulent boundary layers on the wings, tail, and fuselage. This research aims to investigate the use of synthetic jet actuators to manipulate the large coherent structures found in the logarithmic region of the boundary layer. The structures in the logarithmic region of the boundary layer become increasingly dominant with Reynolds number and are considered to be important if turbulent skin friction drag reduction is to be realised at fight scale Reynolds numbers.

Data is collected from both experimental campaigns, primarily through detailed hot-wire and hot-film anemometry, and implicit large-eddy numerical simulation. The two sources of data complement each other well, adding additional insights into the response of the boundary layer and the resulting impact of skin friction. The data shows that the boundary layer is most receptive to low-frequency actuation, enabling effective and dynamic manipulation of the boundary layer properties. It also shows that lower-frequency actuation can modulate the streamwise turbulence intensity in the near wall and achieve skin friction reduction. In contrast, higher frequencies tend to generate more spatially and temporally persistent features, but do not influence the lower frequencies in the logarithmic layer as desired. The limited number of experimental measurement locations is likely to have created a distorted view of the forcing conditions that yield the highest drag reduction. This is shown through spatial maps of change in skin friction generated from the numerical datasets, which indicate that drag reduction is likely overestimated in the experiments.

This research advances our understanding of the interaction of spanwise oriented synthetic jets with turbulent boundary layers. The use of both experimental and computational techniques provides complementary data which adds confidence to the results and broadens the scope of the understanding acquired. Taken together, the experiments and simulations suggest that the lower forcing conditions that are most likely to yield drag reduction; however, drag reduction from open loop control is limited. Therefore, it is proposed to extend the current work by adding a feedforward element to the control system. This is en-

abled by the experimental techniques and simulation capabilities which have been developed and validated in the present work.

Contents

Chapter 1

Introduction

Fuel has become one of the dominant operating costs for commercial airlines. Furthermore, the burning of fossil fuels has a negative impact on both local air quality and global climate change. The amount of fuel burned by aircraft is directly related to their drag. Around 50% of total aircraft drag is due to skin friction caused by the interaction of the turbulent boundary layer with the aircraft surface. Active turbulent boundary layer control for skin friction drag reduction is a relatively new research theme made possible through advances in computational simulation capabilities - that have improved our understanding of the flow structures of turbulence - and micro technology - that enables the fabrication of actuation systems capable of manipulating these structures. Taken together these advances offer new opportunities to significantly increase fuel efficiency.

The structures in the logarithmic part of a turbulent boundary layer become increasingly dominant with Reynolds number. The control of these structures is considered to be important if turbulent skin friction drag reduction is to be realised at flight scale Reynolds numbers. This report summarizes the research at the University of Toronto investigating the use of spanwise oriented synthetic jets to manipulate the large coherent structures in the logarithmic region of the boundary layer. The primary objective of this work is to develop a better understanding of the effect of synthetic jets on turbulent boundary layers and to develop numerical and experimental tools for their study. Further goals are to quantify the effect of the synthetic jet flow control on skin friction and to make recommendations for future work.

Chapter 2

Experimental Studies

Randy Belanger, Ronald Hanson and Philippe Lavoie

List of Symbols

A Area of synthetic jet orifice

a Synthetic jet slot width

B Log law constant

c Speed of sound

c_f Skin-friction coefficient

c_{f_0} Baseline skin-friction coefficient

f Frequency of synthetic jet actuation

H Shape factor

k Peak height of boundary layer trip

k_x Streamwise wavenumber

L Length of straight narrow part of synthetic jet neck

L' Effective neck length of synthetic jet

r blowing ratio

Re_θ Momentum thickness Reynolds number

Re_τ Friction velocity Reynolds number

Re_x Streamwise co-ordinate Reynolds number

St Strouhal number

T Period of synthetic jet forcing

T_s Sampling time

f_H Helmholtz frequency

u, v, w Velocity fluctuation components in the streamwise, wall-normal and spanwise directions, respectively

u' Phase-averaged velocity fluctuations

u_0 Baseline boundary layer streamwise velocity fluctuations

u_j Instantaneous synthetic jet velocity

U, V, W Mean velocity components in the streamwise, wall-normal and spanwise directions, respectively

U_∞ Freestream streamwise velocity

U_0 Baseline boundary layer streamwise velocity

U_j Half of the average jet velocity over the blowing half of the cycle

U_p Maximum phase-averaged synthetic jet velocity over one cycle

U_τ Friction velocity

U^+ Inner-scaled streamwise velocity

V Synthetic jet cavity volume

x, y, z Coordinate directions in streamwise, wall-normal and spanwise directions, respectively

x^+, y^+, z^+ Inner-scaled distances in each coordinate directions: streamwise, wall-normal and spanwise directions, respectively

δ Boundary layer thickness

δ^* Displacement thickness

Δ Center-to-center sythetic jet orifice spacing

Δc_f Change in skin-friction coefficient

θ Momentum thickness

κ Log law constant

λ_x Streamwise characteristic length/wavelength

ν Kinematic viscosity

ρ Density

σ Standard deviation

τ_w Wall shear stress

ϕ Phase

ϕ_{uu} Spectra of streamwise velocity fluctuations

$\bar{\square}$ Averaged quantity

$\tilde{\square}$ Phase-averaged quantity

$\square^+$ Inner-scaled quantity

2.1 Introduction

The results detailed below comprise two separate experimental campaigns. The first measurement campaign began in mid-March of 2016 and focused on the characterization of the velocity response of a pair of synthetic jets. The objective was to acquire time-resolved measurements (hot-wire anemometry) of the boundary layer subject to the influence of synthetic jets. These measurements provide spatial characteristics of the disturbance and temporal characteristics using phased-locking procedures whereas the hot-wire data reach sufficiently near the wall where the near-wall turbulence cycle is dominant and inherently provide access to how the disturbances manifest energetically. For the cases considered, skin friction measurements are included by means of oil-film interferometry. The results from this experimental campaign were included in a previous report, and are repeated here for completeness.

The second measurement campaign began in mid-July of 2017 and focused on the effect of synthetic jet parameters on wall shear stress, and hence skin friction. The objective was to determine the optimal synthetic jet parameters whereby significant skin friction reduction could be achieved. These measurements invoked the use of wall-mounted hot film sensors placed at six locations downstream of a pair of synthetic

jets to measure the wall shear stress quickly at a large number of forcing conditions and three separate jet spacings. Previous skin friction measurements had only been done at a few cases, so these measurements sought to map out a larger region of the parameter space and identify conditions of interest for future studies.

Results from other detailed hot-wire measurements with low frequency forcing from a single jet will also be presented. These measurements were taken during the Fall of 2016.

2.2 Experimental Setup

Experiments were performed in the closed-loop return wind tunnel at the University of Toronto, Institute for Aerospace Studies. The test section of the wind tunnel is nominally 0.8×1.2 m^2 in cross section and 5 m in length. The corners of the test section have adjustable fillets, which are used to modify the pressure gradient. Upstream of the test-section is a 9:1 contraction preceded by flow straighteners and conditioning screens. Downstream of the test-section is a diffuser. Typical measurements of the turbulence intensity at the centre of the test section are $\approx 0.05\%$ at freestream velocities less than 13 m/s.

2.2.1 Boundary Layer Plate

A boundary layer plate was used to establish a turbulent boundary layer. The plate was nominally 12.7 mm thick, made from aluminum, and spanned the 1.2 m width of the test section. The plate was mounted between 1/4 and 1/3 of the test-section height to minimize potential effects of secondary flows [40]. The pressure gradient along the plate was controlled by adjusting the angle of attack of the plate, the flap angle, and the corner fillets of the test section. A machined aluminum insert 200×200 mm^2 was fit flush with the plate along the centre line to support the removable actuator assembly that was flush mounted with the aluminum plate. The boundary layer plate was equipped with an asymmetric leading edge, which was designed to minimize adverse pressure gradients at the leading edge as well as the length of the pressure gradient region [17]. The location of the stagnation line was controlled using a 0.4 m long flap at the downstream end of the test plate. The boundary layer was tripped with zig-zag roughness tape located 40 mm downstream of the leading edge. Two layers of the 0.5 mm thick tape were laid across the span to ensure a sufficient trip strength to transition the boundary layer to turbulence. Practically, the effectiveness of the trip can be ensured by achieving $U(y = k)k/\nu > 300$, where k is the peak height of the trip, and $U(y = k)$ is the stepwise velocity at this roughness height [29].

2.2.2 Instrumentation and Data Acquisition

For single component hot-wire measurements, single probes were used that had 10 mm long prongs spanned by a 3 mm long, 5 μm diameter tungsten wire with a central 1.3 mm active region shouldered on either side by copper-plated sections. The single probe had a length to diameter ratio of 260. The hot-wire probes were operated using a constant temperature anemometer (CTA) with an overheat ratio of 1.8. The CTA was developed at The University of Newcastle [30]. All data were acquired at 25 kHz during boundary layer measurements, although data was sampled at 100 kHz for jet calibration purposes. The data from each CTA were passed through a low-pass filter with a cut-off frequency of 9.6 kHz. All data were sampled with a 16-bit National Instruments PCI-6259, A/D data acquisition card, connected to a PC. Temperature corrections were applied to the hot-wire data using measurements from a T-type thermocouple located in the freestream to account for the ambient temperature variation, which remained within ± 1 °C. Calibrations of the hot-wires were performed immediately before and after each boundary layer profile (or jet calibration) to quantify the drift of the hot-wires over the time and for linear correction. The hot-wires were statically calibrated in situ against a Pitot-static tube connected to a MKS Baratron 120AD 10 Torr pressure transducer over a range of velocities between 1.2 m/s and $1.2U_\infty$, where U_∞ is the freestream velocity of the experiments (10 m/s). King's Law was fitted to the calibration data; the exponent was included in the fit parameters to improve the accuracy of the fitted curve [7].

For the boundary layer profiles, two single component hot-wires were attached to a purpose-built device that was used to position the probes in the boundary layer. Note that this setup has been replaced by a custom designed holder to mount four probes to reduce total measurement time. The probes were separated by 13 mm in the span. The reason for employing more than a single sensor was to reduce total measurement time demand on the facilities. The traverse system that positioned the dual hot-wire probes comprised Velmex Bi-Slides operated by stepper motors, which automated positioning of the probes in the spanwise (z) and wall-normal (y) directions. Profiles of the boundary layer typically contained 42 points, initially spaced linearly then distributed logarithmically up to $0.93U_\infty$, followed by linear spacing up to twice the boundary layer thickness. The normalized sampling time, TU_∞/δ, where T is the sampling time and δ the boundary layer thickness, was typically more than 40 000 to support convergence of phase-averaged statistics of the turbulent fluctuations.

For the second experimental campaign, skin friction measurements were performed over a wide range of forcing conditions. Boundary layer profiles for shear stress calibration were performed with a single probe hot-wire and CTA as described above. The overheat ratio for the hot-wire for these measurements was set at 1.6. Six hot-films were also used to perform the skin-friction measurements. The hot-films were each either a Senflex SF9902 or a mirror-image SF9902M sensor. These sensors consist of a 0.2μm

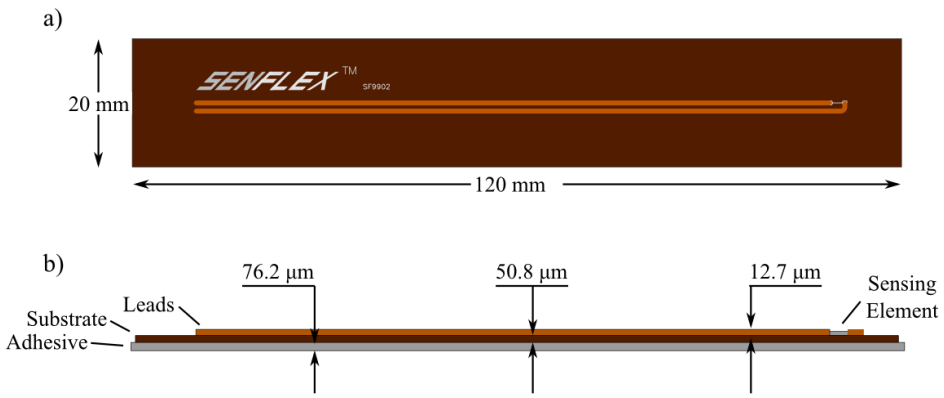

Figure 2.1: a) Top-view, and b) side-view of a Senflex SF9902 hot-film sensor that was used for shear stress measurements.

thick nickel sensing element that is 0.10 mm wide by 1.45 mm long, attached to two 0.76 mm-wide, 12.7 μm-thick copper leads, and deposited on a polyimide substrate measuring 20 mm $\times$ 120 mm, and having a thickness of 50.8 μm, as in Figure 2.1. The sensor substrate was adhered to the flat plate model using a 76.2 μm-thick MACtac IF-2043 pressure sensitive adhesive. Thus, the entire height of the sensor and adhesive above the model at the location of the sensing element is 0.127 mm. The hot-films were controlled on six separate channels of two four-channel Newcastle CTAs described above, operating at overheat ratios of 1.4$-$1.6. Similar to hot-wire measurements, the hot-films were also acquired at a sampling rate of 25 kHz and passed through a low-pass filter at 9.6 kHz.

2.2.3 Synthetic Jets

A pair of synthetic jets have been designed, each with an outlet rectangular orifice of 13 mm$\times$1 mm, as shown in Figure 2.2. The jets are nominally spaced 26 mm apart, such that the dual jet forms the basis for a regular array; however, a single jet can also be operated such that the 13 mm dimension extends in the streamwise direction. Two other jet spacings are also investigated where the jets are separated 19.5 mm and 32.5 mm apart. An assembly, exploded, and section view (left to right) of the pair of jets is shown in Figure 2.3. As shown, a single jet is composed of a loud speaker, a main cavity that also includes a mounting structure, an internal cavity to feed the jet nozzle, and a printed nozzle. The loud speakers are a Visaton model SC8N - 8 Ohm. The main cavity depth is 6.35 mm, followed by a 1.27 mm depth of the internal nozzle supply cavity, each with a diameter of 68 mm. The resonant frequency of the speaker supplied by the manufacturer is $\approx$ 110 Hz whereas the Helmholtz frequency of the synthetic jet can be estimated [28], viz.

$$f_H = \frac{c}{2\pi}\sqrt{\frac{A}{VL'}}, \tag{2.1}$$

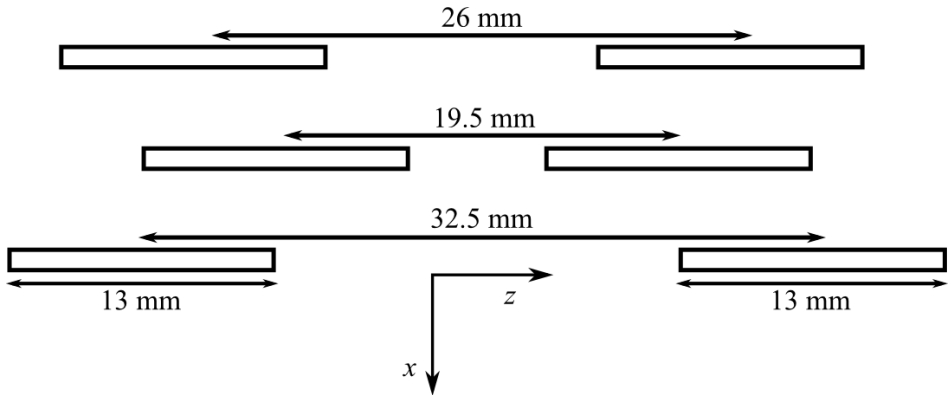

Figure 2.2: Coordinate frame and jet layout for the three different jet spacings that will be used in this report; nominal 26 mm, narrow 19.5 mm, and wide 32.5 mm.

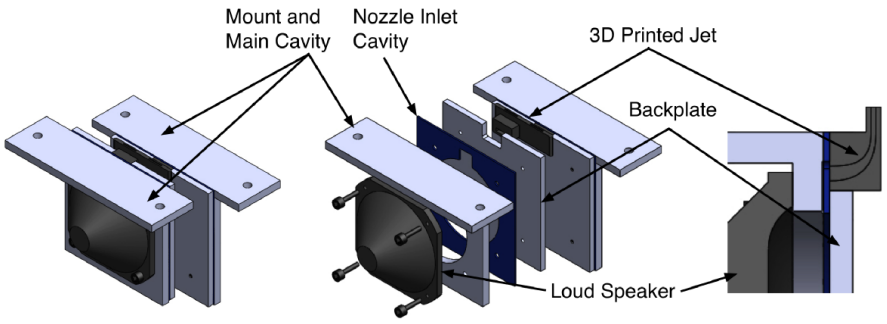

Figure 2.3: Assembly and exploded view of the jet assembly with a section view of one of the jet nozzles (from left to right).

where c is the speed of sound, A the area of the jet orifice, V the cavity volume and L' the effective neck length. To estimate f_H we assume the cavity volume from the geometry of the jet parts and exclude effects of the loud speaker geometry. The effective neck length is estimated as $L' = L + 1.4a$, where L is the length of the narrow straight portion of the neck (5.1 mm) with a width of dimension $a = 1$ mm, leading to $f_H = 450$ Hz.

The excitation signal provided to each jet was produced by a Rigol DG1000 2-Channel function generator. This signal was amplified by a Crown XTi 2002, 2-channel amplifier. The excitation signal was monitored along with measurements to facilitate phase-averaging of statistics detailed later. Each jet was driven independently, which is necessary given differences in jet output and phase associated with minor variations in the assembled components and speakers. As such, jet calibrations were required individually for each jet, and new calibations were required each time a new jet insert with a different jet spacing was used.

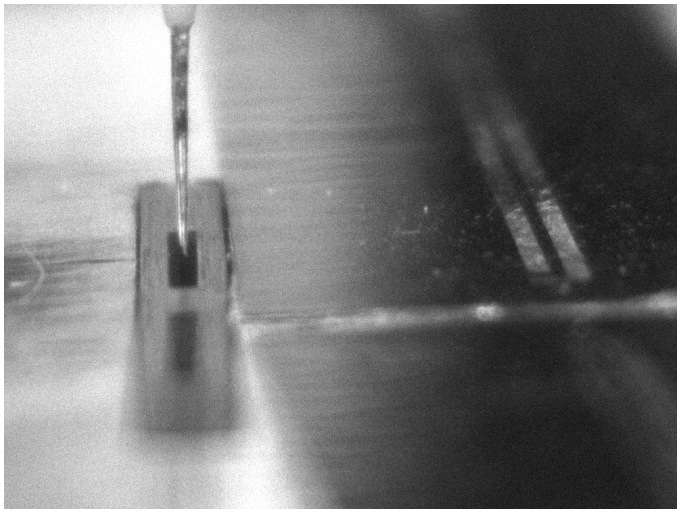

Figure 2.4: Approximate side view (+ 10 degrees) of the jet and hot-wire probe at the jet exit.

2.2.4 Synthetic Jet Calibration

The synthetic jet calibration was performed using a single hot-wire probe positioned at the exit of the jet in quiescent air. The probe was approximately centred within the dimensions of the jet exit cross-section by visual inspection using a CCD camera; an example image is shown in Figure 2.4. Because of the nature of a synthetic jet, having no net mass transfer, inside the jet orifice the flux of air in and out is equal over a complete cycle. Therefore the probe was positioned slightly away from the jet, in the direction normal to the outlet orifice, until the expulsion portion of the cycle was clearly visible from the injection portion. Practically this amounts to a very small distance on the order of 0.1 mm. Several preliminary tests were performed to validate that the expulsion velocity obtained with the hot-wire probe exhibits no quantifiable difference over this small distance. Furthermore, a phase shift over this distance could not be quantified, although practically an extremely small phase shift must exist.

Each of the jets was calibrated across a range of excitation frequencies and voltage amplitudes. The gain of the audio amplifier (described previously in Section 2.2.3) was determined by driving the amplifier at several input voltages and determining the linear relationship. Frequencies were varied from $100 - 900$ Hz, typically spaced in 50 Hz increments with 25 Hz increments about the resonant peak, resulting in 21 frequencies for measurements. The voltage was varied from 2 to 30 volts (peak-to-peak), where these voltages are at the output of the audio amplifier directly input to the speakers. Voltage was varied at increasing step size to improve resolution at lower voltages such that the non-linear velocity output with driving voltage was well resolved across a range of 17 voltage conditions. This resulted in a calibration surface made up of $17 \times 21 = 357$ point measurements. The jet calibrations for the hot-film measurements were extended down to 1 Hz, and spaced in 2.25 Hz increments between 1 and 10 Hz, 22.5 Hz increments between 10 and 100 Hz. Further, the voltage was also extended down to 0.05 V (peak-to-peak) in order to

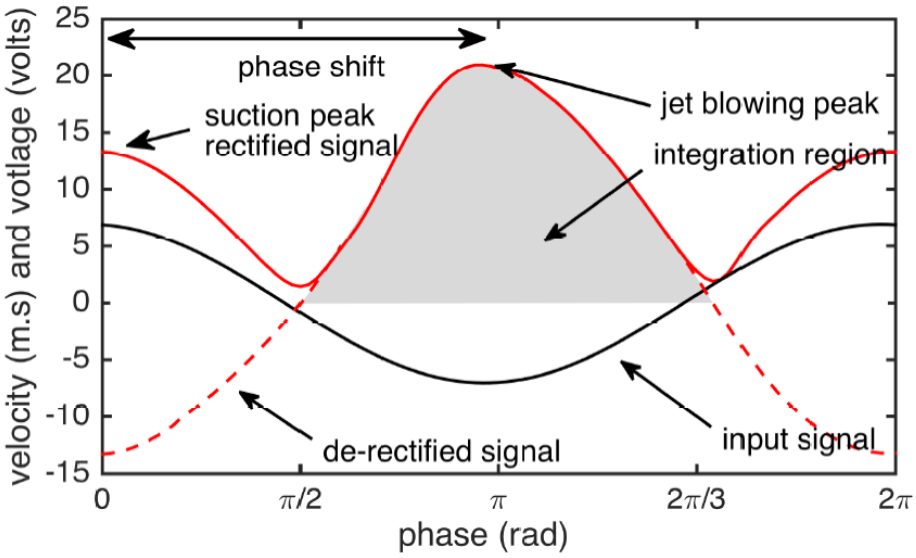

Figure 2.5: Example phase-averaged data from a jet calibration with descriptions

ensure the largest possible parameter space.

The velocity scale of a synthetic jet, U_j, is given as half of the average velocity of the blowing portion of the actuation cycle, *viz*.

$$U_j = \frac{1}{T}\int_0^{T/2} u(t)\mathrm{d}t, \tag{2.2}$$

where T is the time period of the actuation cycle $(1/f)$, $u(t)$ is the phase-averaged velocity signal at the exit of the jet. An example calibration point is shown in Figure 2.5. For this case the peak-to-peak voltage of the input signal was approximately 14 volts, and the frequency of the excitation was 250 Hz. Typically $1500 - 2500$ cycles of the jet were sampled for these phase averages, which were locked to the input voltage signal supplied by the function generator; however, data appeared to converge within a few hundred cycles. Identified in this figure is the excitation signal supplied to the actuators and the resulting rectified hot-wire signal. The hot-wire signal is rectified since it cannot distinguish direction. Because the hot-wire was placed $0.1 - 0.15$ mm above the jet exit the expulsion peak is the greater of the two peaks. Therefore the hot-wire signal can be de-rectified as shown in Figure 2.5, where a spline was fit to the data surrounding the regions between the suction and expulsion peak, and the fitted curve was resampled in the region about $\pm\pi/16$, which was difficult to correct otherwise. The grey shaded region represents the expulsion peak that was integrated following Equation 2.2. The phase shift represents the lag between the input and output velocity signal of the jet. This phase was captured by the cross-correlation between the input and de-rectified velocity signal. In this particular example the expulsion peak lags by a phase of approximately π radians.

Example jet output calibration surfaces for the two jets are shown in Figure 2.6 (a, b) for Jet 1 and

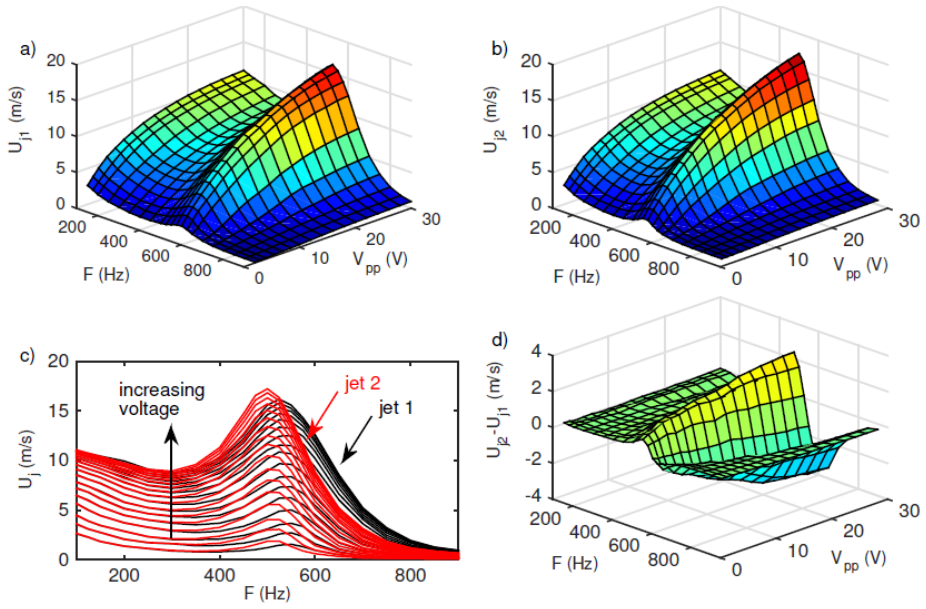

Figure 2.6: Average velocity of the blowing portion of the actuation cycle determined from Eqn. for a) Jet 1, b) Jet 2, c) comparable line plots, and d) the difference.

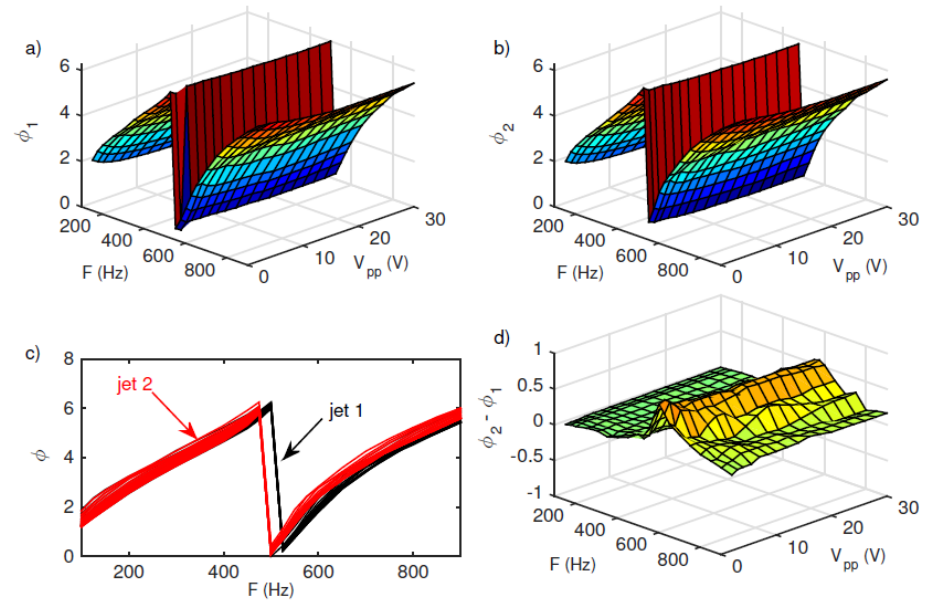

Figure 2.7: Phase of the actuation cycle relative to the input velocity signal a) Jet 1, b) Jet 2, c) comparable line plots, and d) the difference.

Jet 2, respectively. The peak in the output of the jets corresponds to the Helmholtz resonance frequency. For Jet 1, this peak occurs at approximately 500 Hz and 475 Hz for Jet 2. It is evident from inspection of Figure 2.6 (a, b) that the two jets, although having the same design, give slightly different output. From Figure 2.6 (c, d) the output of Jet 2 at resonance is higher than that of Jet 1. The peak difference in U_j is approximately 2 m/s; however, at higher frequencies this difference is greater, likely owing to a difference

Case	Frequency (Hz)	Mean expulsion velocity (m/s)	Strouhal number	Blowing ratio
1	119	8.8	0.5	0.88
2	238	8.8	1	0.88
3	548	8.8	2.3	0.88
4	548	4.5	2.3	0.45
5	548	13.5	2.3	1.35

Table 2.1: Summary of cases.

in damping, which may be inferred from the peak width about the resonant frequency from Figure 2.6 (c). Several factors may affect the synthetic jet behaviours. First from examining Equation 2.2, slight difference in manufacturing can vary the estimated Helmholtz resonant peak such as the orifice dimensions or those of the cavity. Differences in damping may be related to the nozzle, such as internal roughness or sharpness of the nozzle outlet. Furthermore, differences from speaker to speaker may play a role. In either instance, the variation of jet performance is primarily greatest about the Helmholtz resonant peak, as found from the phase relationships shown in Figure 2.7. Prior to the Helmholtz resonance the synthetic jets exhibit similar performance characteristics as can be found from Figures 2.6(d) and 2.7(d). This shows the importance of obtaining a detailed calibration for each jet and whenever a new jet insert was used. Differences are compensated by independently determining the driving conditions to match actuator output and phase during experiments.

2.3 Hot-Wire Measurements of Boundary Layers Actuated at High Frequency

Following from the experimental parameters summarized in Ref. [16] there are 5 main forcing conditions that the synthetic jets are activated and tested at, which are summarized in Table 2.1. The major parameters considered are the blowing ratio, r, and the synthetic jet Strouhal number, St. The blowing ratio was defined here as the ratio of the mean expulsion velocity, defined in Equation 2.2, and the freestream velocity, *viz.* $r = U_j/U_\infty$. The Strouhal number is a non-dimensional frequency given by $St = \delta f/U_\infty$, where δ is the boundary layer thickness and f is the frequency of actuation.

2.3.1 Baseline Flow Field

The turbulent boundary layer occurring over the plate was measured in the absence of forcing by the synthetic jets. The resulting boundary layer is shown with outer scaling by the freestream velocity, U_∞, and boundary layer thickness, δ, in Figure 2.8. The mean streamwise velocity of the boundary layer shown in Figure 2.8(a) exhibits a decreased velocity in the near-wall region, consistent with the viscous region, and a linear region in the semi-log plot, which indicates the presence of a logarithmic region. Another feature

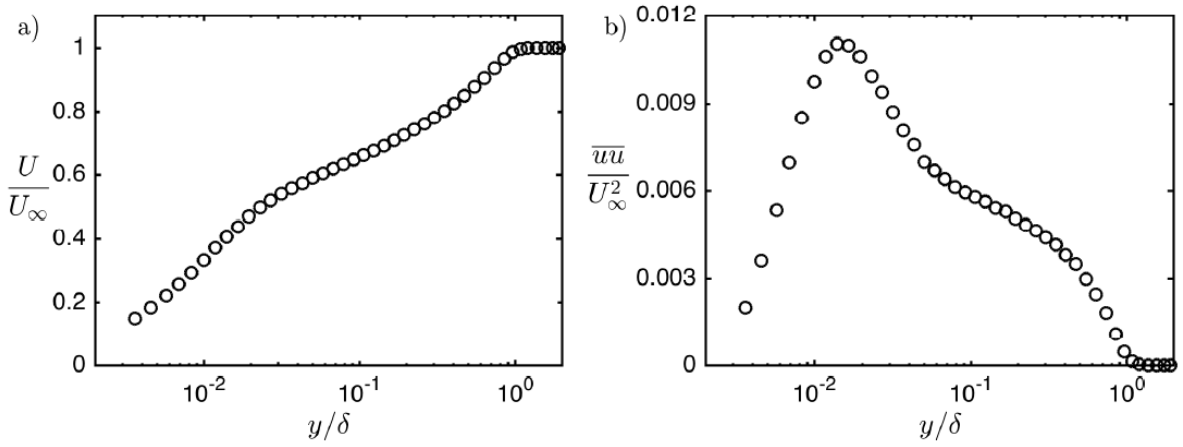

Figure 2.8: Outer scaling of the baseline boundary layer including (a) the mean streamwise flow velocity and (b) the streamwise Reynolds stress.

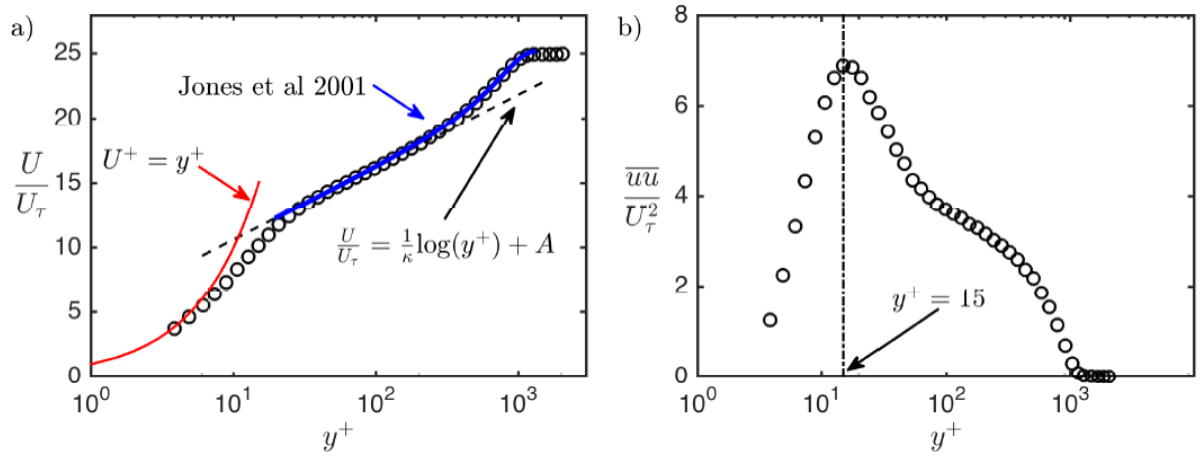

Figure 2.9: Inner scaling of the baseline boundary layer (a) mean streamwise velocity showing the nearwall viscous region, log region, and wake region fits and (b) the inner scaled streamwise Reynolds stress.

visible is the peak in the near wall turbulence intensity shown in Figure 2.8(b), which is associated with the near-wall production of turbulence. The location of this feature, however, does not scale with outer variables because it depends on the near-wall viscous influences. Therefore we consider inner normalizations to compare the boundary layer profiles with documented behaviour in the literature.

The resulting inner-normalized boundary layer mean streamwise flow velocity (U) and streamwise Reynolds stress is shown in Figure 2.9(a, b), respectively. For the inner normalization by the skin friction velocity, U_τ, this parameter was calculated from the logarithmic region of the boundary layer between approximately $y^+ = 60$ and $y^+ = 200$. The Clauser method was employed such that U_τ is chosen to optimize the fit of $U/U_\tau = (1/\kappa)\log(yU_\tau/\nu)+B$, where $\kappa = 0.41$ and $B = 5.0$, as indicated in Figure 2.9(a). Thus an iterative method was employed to verify that data points used are within the logarithmic region. From this scaled data it is evident that the near-wall satisfies $U^+ = y^+$. Furthermore, the composite

δ	U_∞	δ^*	θ	H_{12}	U_τ	c_f	Re_θ	Re_τ
42.5 mm	10.01 m/s	7.19 mm	5.16 mm	1.395	0.401 m/s	0.00322	3230	1070

Table 2.2: Boundary layer properties 10 mm upstream of the jets.

profile of Jones *et al.* [26] was included to model the wake region, where the wake factor is found to be approximately 0.55.

A summary of the measured and calculated parameters of the baseline boundary layer determined from the data shown in Figure 2.8 and Figure 2.9 is given in Table 2.2. The shape factor is typical of a zero pressure gradient turbulent boundary layer, and the skin-friction coefficient based on the calculated skin friction velocity is within 1.4% of the empirical relationship reported by Osterlund *et al.* (2000), which is well within the range of scatter of the tabulated data forming the basis of that relationship, $c_f = 2((1/\kappa)\log(Re_\theta)+B)^{-2}$. Further evidence of the reliability of the inner scaling is given by Figure 2.9(b) where the near-wall peak in turbulence occurs around 15 wall units, which is consistent with the expected location of $y^+ = 15 \pm 1$ [23].

2.3.2 Spatial Response of Forced Boundary Layers

The spatial response of the boundary layer is considered by comparing the time-average of the actuated and baseline unactuated boundary layer at the same streamwise location. Practically this requires measurement of the actuated and unactuated case to limit uncertainty of the spatial growth of the boundary layer documented at the streamwise location of the jets. The time-averaged mean velocity is given by U, where U is the ensemble average of the instantaneous streamwise velocity signal. The ensemble average of the baseline boundary layer streamwise velocity is given by U_0. The discrepancy between the perturbed and baseline boundary layer is quantified by $U - U_0$ and normalized in outer units by U_∞, the freestream velocity. This gives insight into the net increase/decrease in streamwise velocity of the boundary layer affected by the jets. The time averaged spatial response to forcing for the cases summarized in Table 2.1 is shown in Figure 2.10, where the final case is omitted at $x/\delta = 5$. The red and blue colours of these figures represent the cases where the actuated time-averaged velocity is either greater than or less than the baseline, respectively.

Examining Figure 2.10 there are a number of interesting features to remark on. First, changes in mean streamwise velocity, U, are prevalent for a greater portion of the boundary layer thickness at $x/\delta = 5$ compared to $x/\delta = 1.5$, which is attributed to the trajectory of the disturbance, as shown in Gomit *et al.* [16]. The spatial signature of the flow appears most similar for the two lowest Strouhal numbers of 0.5 and 1. A pair of low speed streaks appear in the boundary layer at approximately $y/\delta = 0.3$ and $x/\delta = 1.5$ directly downstream of the centre of each jet $z/\delta = \pm 0.3$. Farther downstream at $x/\delta = 5$, these streaks appear

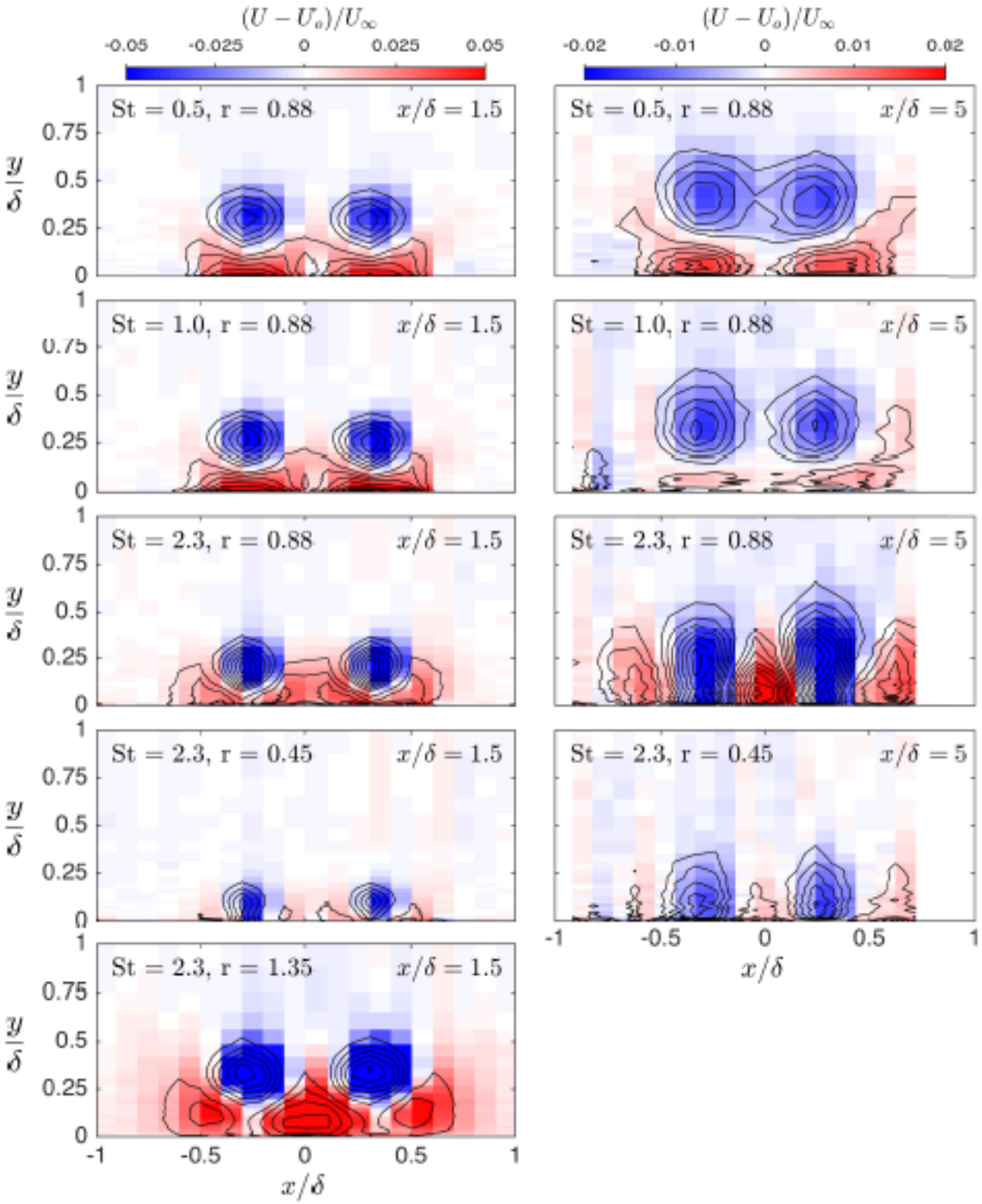

Figure 2.10: Difference between the actuated and baseline boundary layer mean flow $(U - U_0)/U_\infty$ for the cases summarized in Table at $x/\delta = 1.5$ and $x/\delta = 5$.

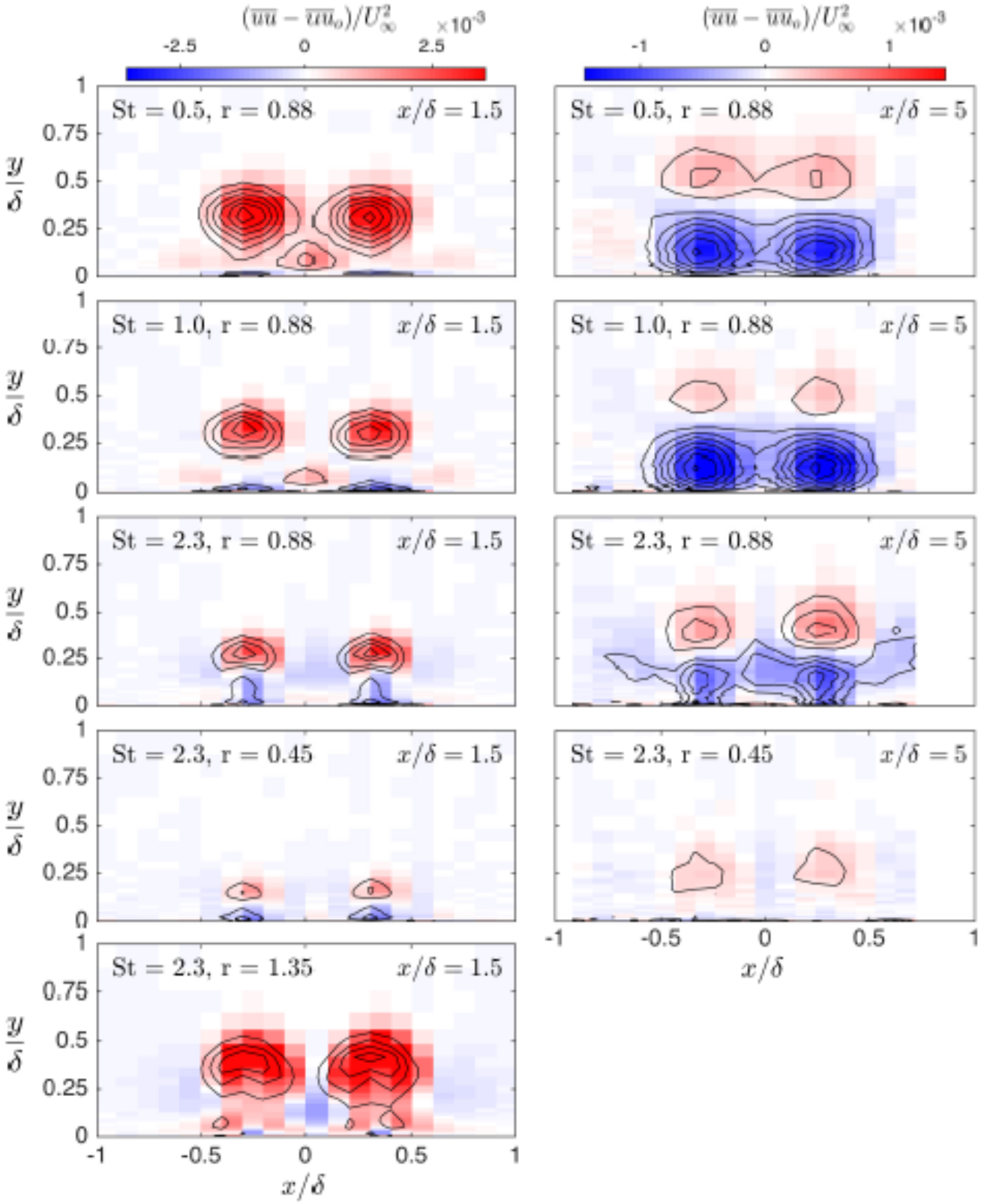

Figure 2.11: Difference between the actuated and baseline boundary layer streamwise normal Reynolds stress $(\overline{uu} - \overline{uu_0})/U_\infty^2$ for the cases summarized in Table 2.1 at $x/\delta = 1.5$ and $x/\delta = 5$.

slightly higher and centred between $y/\delta = 0.3$ and 0.4. Comparatively, for St= 2.3 at $x/\delta = 5$, the flow field contains only regions of low and high velocity extending to the wall such that the low velocity appears as an effective wake downstream of the synthetic jets. For increasing Strouhal number, this suggests that the behaviour of the actuated flow is markedly different. The low speed streaks having regions of excess velocity near the wall is characteristic of the presence of pairs of streamwise counter-rotating vortices. Near the wall, for increasing Strouhal number at $x/\delta = 1.5$, the pair of low-speed steaks are concentrated nearer the wall, suggesting a change in the underlying dynamics. The spatial response of the turbulence intensity in the boundary layer is considered by comparing the ensemble average of the actuated and baseline un-actuated boundary layer at the same streamwise location as shown in Figure 2.11. In this figure it is shown that the low speed regions observed in Figure 2.10 correspond with regions of increased fluctuation intensity. As shown in Figure 2.10 the streamwise velocity is modified by the presence of pairs of streamwise counter-rotating vortices and confirmed by the stereo PIV results shown in Gomit *et al.* [16]. Therefore the modification of the streamwise turbulence by the jets can be caused by the rearrangement of the boundary layer in the presence of streaks, but also by the inherent fluctuations induced by unsteady actuation of the jets.

2.3.3 Properties of Turbulent Spectra

Statistics of the streamwise velocity fluctuations (u) represent the combined influence caused over all flow scales. The spectra of the streamwise fluctuations, ϕ_{uu}, are examined to investigate the scales of motion within the turbulent boundary layer following actuation by the synthetic jets. In addition to the mean statistics reported previously, the spectra offer information on how the near-wall and outer regions of the boundary layer manifest energetically. The local convective velocity is employed using Taylor's hypothesis to express the temporal spectra as a function of streamwise wavenumber, $k_x = 2\pi f/U$, and wavelength, $\lambda_x = 2\pi/k_x$. Spectra at each wall-normal location were pre-multiplied by the wavenumber, k_x, and normalized by the outer scale, $k_x(\phi_{uu}/U_\infty^2)$. Contours of the pre-multiplied spectra are assembled from the spectra obtained at each wall-normal location following the methodology of Hutchins & Marusic [22], which provides a physical sense of the distribution of the energetic composition across the boundary layer.

The variation of the pre-multiplied spectrogram of $k_x\phi_{uu}/U_\infty^2$ for the 5 actuation cases are shown along the right column in Figure 2.12, and along the left column the corresponding mean flow velocity and fluctuations $\overline{uu}$ are included for comparison. The labels in Figure 2.12 from $a - e$ correspond to cases $1 - 5$ from Table 2.1, respectively. For each of the pre-multiplied spectrograms, a solid line shows the corresponding actuator frequency which is plotted as $k_x = 2\pi f/U$, where f is the physical actuator frequency in Hz and then $\lambda_x = 2\pi/k_x$ for these lines. Examining the spectra reveals that although the

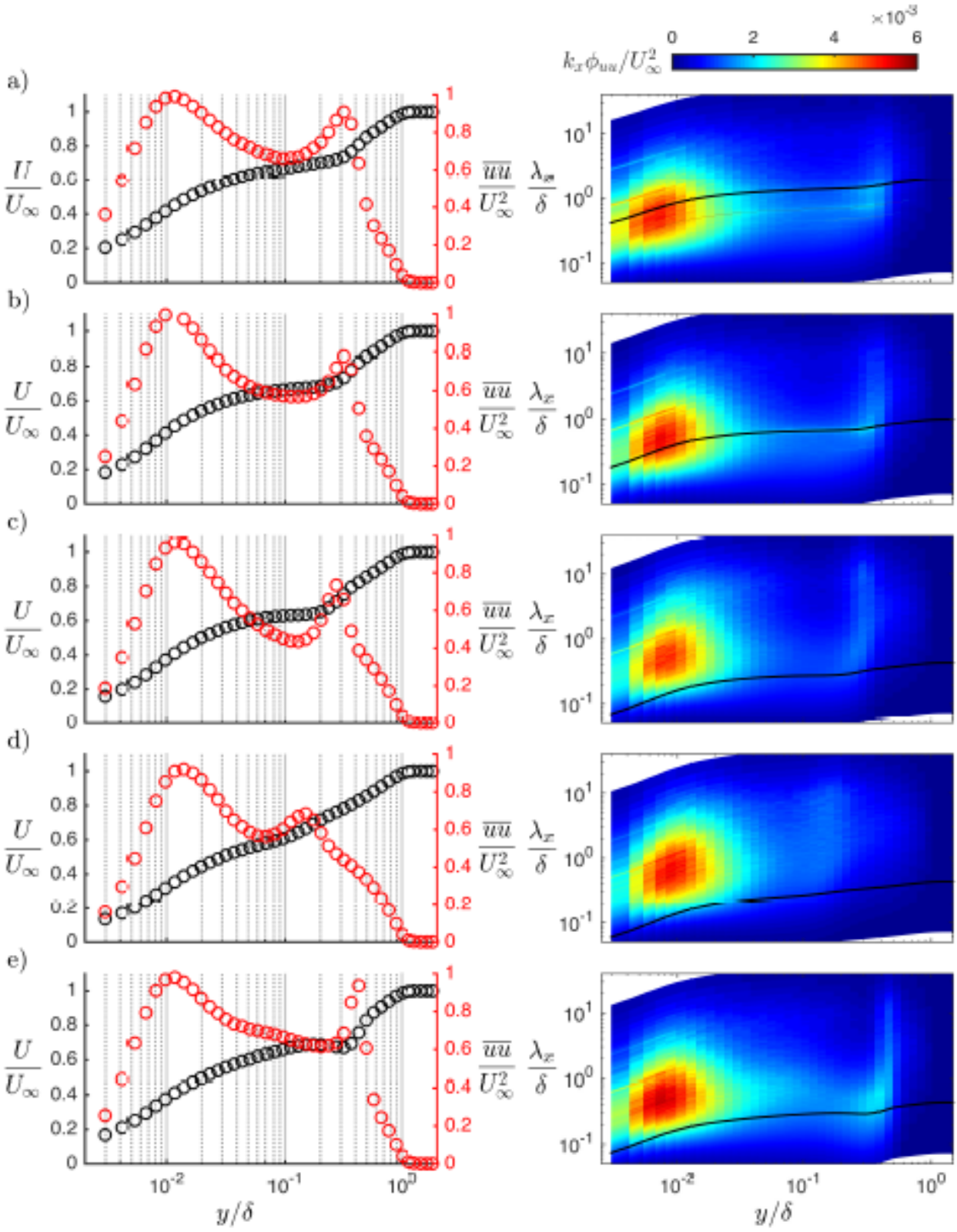

Figure 2.12: The variation of the pre-multiplied spectrogram of $k_x\phi_{uu}/U_\infty^2$ for the 5 actuation cases along the right and corresponding mean flow and broad-band turbulence statistics.

synthetic jets are operated at a discrete frequency the resulting response of the boundary layer appears to occur over a range of frequencies. For example, see Figure 2.12(a) where aside from the solid line indicating the driving frequency of the jets there are signatures of both lower and higher harmonics. Ultimately the output of the synthetic jets is not a perfect sinusoidal wave; see for example Figure 2.5 where the output velocity signal is clearly distorted from a fundamental sine wave, notably at the peak blowing. Furthermore, for synthetic jets the boundary layer does not experience the effect of a pure sinusoidal input. Consider that the effect of the expulsion cycle and injection cycle on the boundary layer is markedly different; this point will be made clear in Section 2.3.5.

Another feature shown in Figure 2.12 is that the frequency of the synthetic jet actuation is similar to, or at a higher frequency (or shorter wavelength λ_x) than, the near wall turbulent dynamics. For the lowest Strouhal number case, the scale separation is minimal or non-existent, here $f = 118$ Hz for $U_\infty = 10$ m/s. This also shows that $\lambda_x/\delta \approx 1$ in the outer region of the boundary layer. If we consider the scaling by U_τ of the baseline boundary layer from values given in Table 2.2, then the inner peak will be centered about $\lambda_x^+ \approx 1000$ and $y^+ \approx 15$. For $\lambda_x^+ \approx 1000$, and knowing U_τ, we can estimate the central frequency of the near wall frequency energy peak (assuming that the log region can be used to provide a velocity, which is a reasonable assumption for this estimate), *viz*.

$$f(\lambda_x^+ = 1000) = \frac{U(y^+)}{1000} U_\tau/\nu, \tag{2.3}$$

where $U(y^+) = ((1/\kappa)\log(y^+) + B)U_\tau$, and we assume $y^+ = 15$ for the near wall peak in the spectra. This leads to $f(\lambda_x^+ = 1000) \approx 85$ Hz, which appears underestimated in Figure 2.12(a) where the peak in the near wall energy is at a slightly higher frequency than that of the forcing at 118 Hz. However, at $x = 1.5\delta$ the boundary layer is far from equilibrium and the usage of the baseline value of U_τ is not directly applicable, but serves as an estimate. Regardless, even at these Reynolds numbers the driving frequency of the synthetic jets appear high in comparison to natural large scales associated with turbulent boundary layers, often occurring in the range of three-dimensional large-scale structures of approximately 6δ *superstructures*, see for example Hutchins & Marusic [22]. Note also that Hutchins & Marusic [21] observed that superstructures can be much longer than 6δ (up to 20δ); however spanwise meandering results in the signature in the energy spectrum to appear at shorter scales.

2.3.4 Temporal Response at Fixed Spanwise Locations

The synthetic jets are operated periodically at a fixed frequency, which lends naturally to a phase-locked analysis where the phase reference is the excitation signal applied to the jets. For the boundary layer under

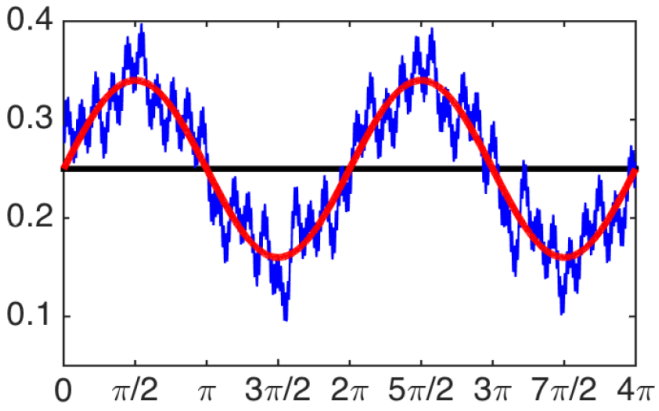

Figure 2.13: Graphical description of the phase-locked decomposition where the solid black line represents the mean velocity at a location, y, the red line represents the ensemble average of the phase-referenced velocity about this mean, and the blue line represents instantaneous variations about the phase-averaged flow.

the influence of forcing by the synthetic jets, the streamwise velocity can be decomposed as follows, viz.

$$U(y) + \tilde{U}(y, \phi) + u'(y, \phi), \tag{2.4}$$

where U is the time-averaged flow velocity at a location y in the boundary layer, $\tilde{U}(y, \phi)$ is the phase-locked variation of the flow that is ensemble-averaged over a number of synthetic jet cycles, and $u'(y, \phi)$ is the variation in the turbulence about $U(y) + \tilde{U}(y, \phi)$ over the phase-locked cycle, see for example Hussain & Reynolds [20]. An example figure of this description is shown in Figure 2.13. Note that instantaneous fluctuations are shown about the phase-locked mean flow for purely illustrative purposes. The quantity $u'(y, \phi)$ actually represents statistics of the fluctuations.

The variation of the phase-locked streamwise velocity is shown in Figure 2.14 at $x/\delta = 1.5$ for cases 1, 2, 3, where $St = 0.5$, 1.0 and 2.3, respectively. For these cases the maximum and minimum scales of each subfigure are modified and by definition the mean over a phase of 2π is zero. For each of the cases the strength of the disturbance and phase variation is similar directly downstream of jet 1 and jet 2, which suggests that the calibration and implementation procedure for two jets described previously was adequate. Between the cases, however, the characteristic shape of the disturbance for $St = 0.5$, see Figure 2.14a, and $St = 1$, see Figure 2.14b, is similar, whereas for the case where $St = 2.3$, see Figure 13c, the phase-locked disturbance variation does not appear to be comparable with the former cases. This indicates a fundamental change in the dynamical response of the boundary layer to the forcing at the Strouhal numbers considered.

The aforementioned difference between the phase-locked behaviour of the $St = 2.3$ and the other cases becomes more apparent at $x = 5\delta$, where cases 1 and 3 with $St = 0.5$ and 2.3, respectively, are

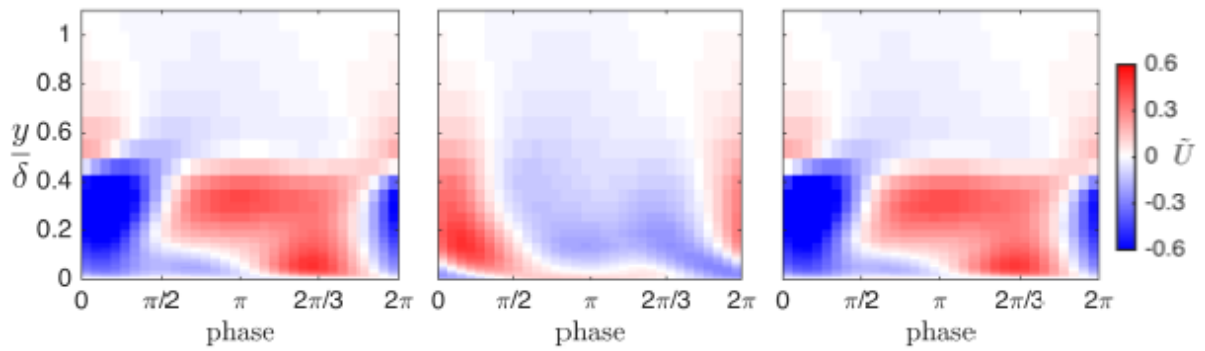

(a) $St = 0.5, r = 0.88.$

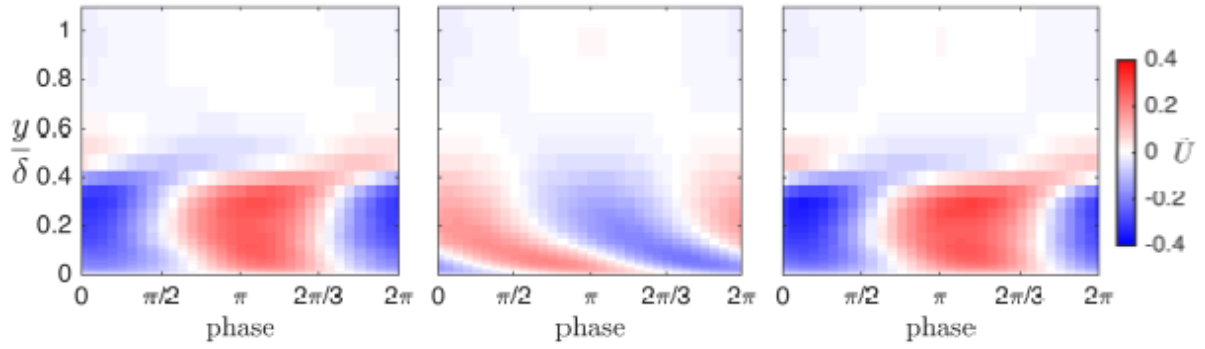

(b) $St = 1, r = 0.88.$

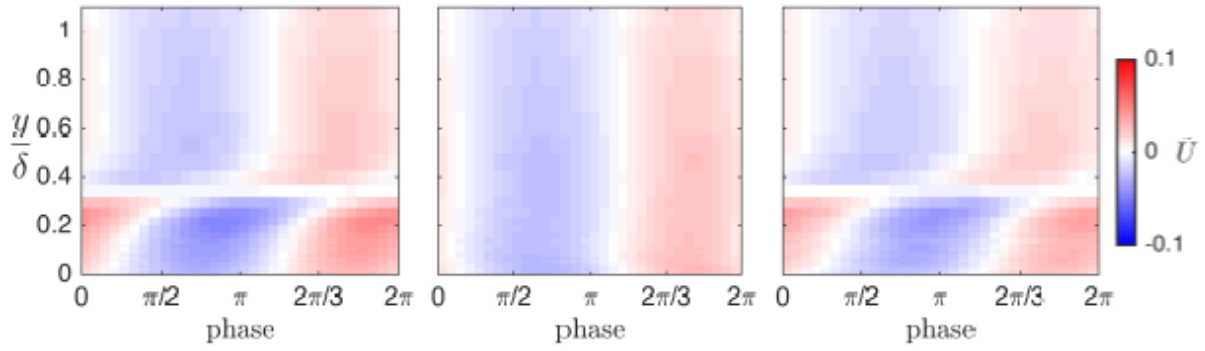

(c) $St = 2.3, r = 0.88.$

Figure 2.14: Variation of the phase-locked velocity at $x = 1.5\delta$. From top to bottom, $St = 0.5$, 1, 2.3 for $r = 0.88$. From Left to Right, $z = -13$, 0 13 mm, or directly downstream of jet 1, between jet 1 and 2, and directly downstream jet 2. Note the change of max/min scale for each.

shown in Figure 2.15. Comparing Figure 2.15b and 2.14c suggests that the dynamics visible at lower Strouhal numbers becomes highly damped, and in the case of the latter the three dimensional time-varying behaviour does not exist. Interestingly the phase-locked behaviour for this case is consistent across the span (z-coordinate), as shown in Figure 2.15b, suggesting that the impulse to the boundary layer by the synthetic jets is felt; however, the unsteady dynamic of embedding streaks does not occur. Considering the spectrograms shown in Figure 2.12 for the higher Strouhal number, the physical frequency of the actuator

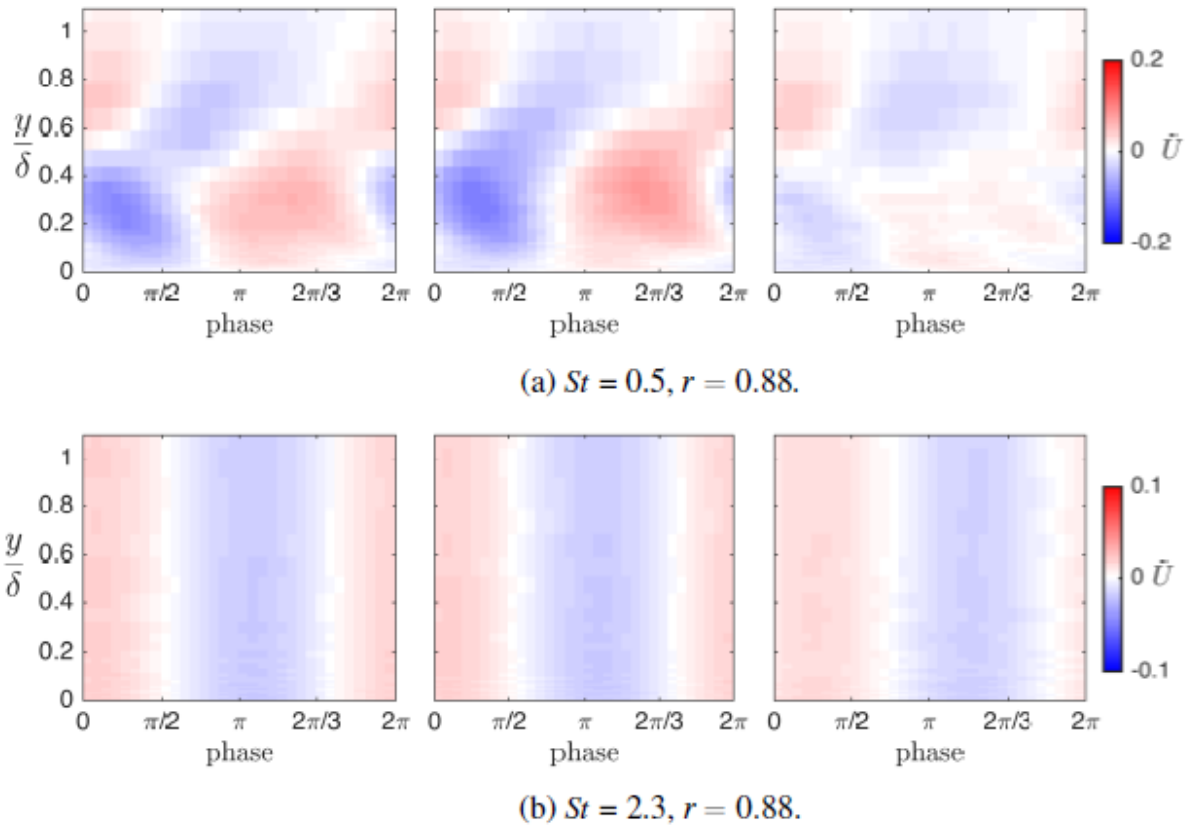

Figure 2.15: Variation of the phase-locked velocity at $x = 5/\delta$, otherwise similar to Figure 2.14.

is higher than the dynamics of the inner turbulence peak, which is confined to the wall where turbulence production is greatest at these Reynolds numbers. Likewise the inner site does not propagate outward with increasing shear stress. It is therefore thought that such high-frequency forcing is not resilient in the outer region of the boundary layer, which is typically characterized by large-scale structures both in space and time. These results suggest that large-scale (low-frequency or low St) forcing is required to have a significant impact on the outer region of the boundary layer that will be persistent over elongated regions downstream.

2.3.5 Temporal Response at $y - z$ Planes

For the temporal response over a $y - z$ plane we consider two streamwise locations at $x = 1.5\delta$ and $x = 5\delta$ within a region bounded by the boundary layer thickness and $\pm 1\delta$ along the span. As shown previously, the centre of one jet is at approximately -0.3δ and the other jet is at approximately 0.3δ in the spanwise (z) coordinates. A sample of the results pertaining to the temporal response is given in Figures 2.16 and 2.17 at $x = 1.5\delta$ and $x = 5\delta$, respectively. Only the two lowest Strouhal numbers, 0.5 and 1, are considered, since as shown previously the dynamics of the highest Strouhal number appear downstream simply as a periodic fluctuation of the streamwise velocity that is consistent along the span, see for example Figure 2.15b.

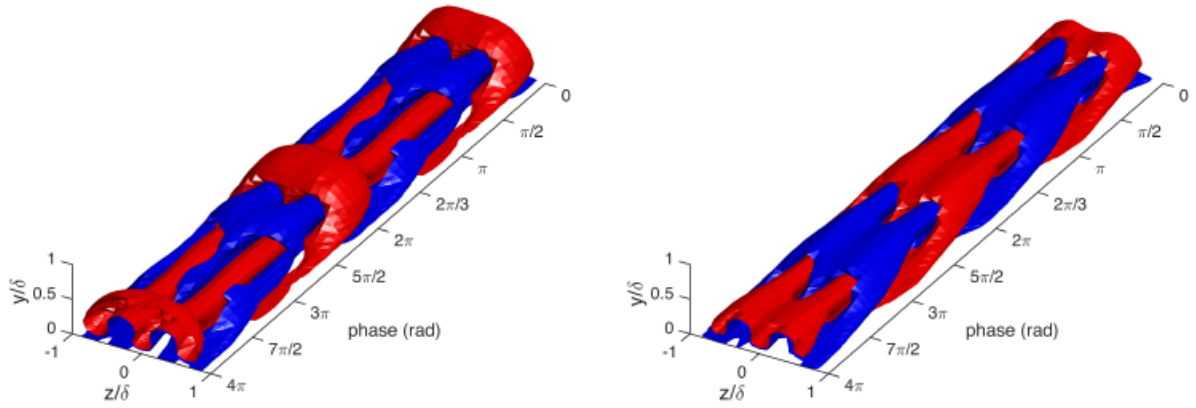

(a) $St = 0.5, r = 0.88$. (b) $St = 1, r = 0.88$.

Figure 2.16: Variation of the phase-locked velocity $\tilde{U}(y, z, \phi)$ normalilzed by the freestream velocity at $x = 1.5\delta$ over two complete cycles. Red and blue contours are set at $\pm\sigma/2$ of the fluctuations considered over the two-dimensional plane.

The isosurfaces shown in Figures 2.16 and 2.17 essentially represent the surface formed from points that have the same specified value, similar to contour lines of equal elevation for the phase-locked component, $\tilde{U}/U_\infty$. Note that the phase is given in a decreasing fashion to represent the convection of the disturbance through the measurement plane (i.e. equivalent to the fluid flowing from left to right.). The red (increased velocity, or excess) and blue (decreased velocity, or deficit) contours are drawn at $\pm\sigma/2$ of the fluctuations considered. This level was selected since it gives a clear picture of the dynamics throughout the boundary layer. From examining Figures 2.16a and 2.16b there are several remarkable features. The first is the regions of strong velocity excess at approximately 2π radians that appear to form legs that extend to $7\pi/2$ radians of the actuation cycle. This behaviour is consistent with the formation of a hairpin vortex structure during the blowing phase of actuation. It is also important to note that by definition, integration over the disturbance phase results in a zero mean. Such a vortical motion can induce a secondary vortex, another remarkable feature from these figures, which may be responsible for the legs of the deficit structure shown, for example between 4π and 3π.

Comparing the results of the two different Strouhal numbers, for example between Figures 2.16a and 2.16b, suggest a different receptivity. For example, the lower Strouhal number disturbance is spread over a greater region of the boundary layer, and this difference in strength is further supported by the results of Figure 2.12 and Figure 2.14, where the lower Strouhal number of actuation led to an increase in the disturbance level at comparable streamwise locations. This is also evident from Figure 2.17 where the level of noise appears greater for the case with $St = 1$. For comparison, the isosurfaces in Figure 2.17b are drawn at a level approximately 4 times lower in magnitude than for $St = 0.5$ in Figure 2.17a to maintain the condition of $\sigma/2$ levels of the periodic component of $\tilde{U}/U_\infty$.

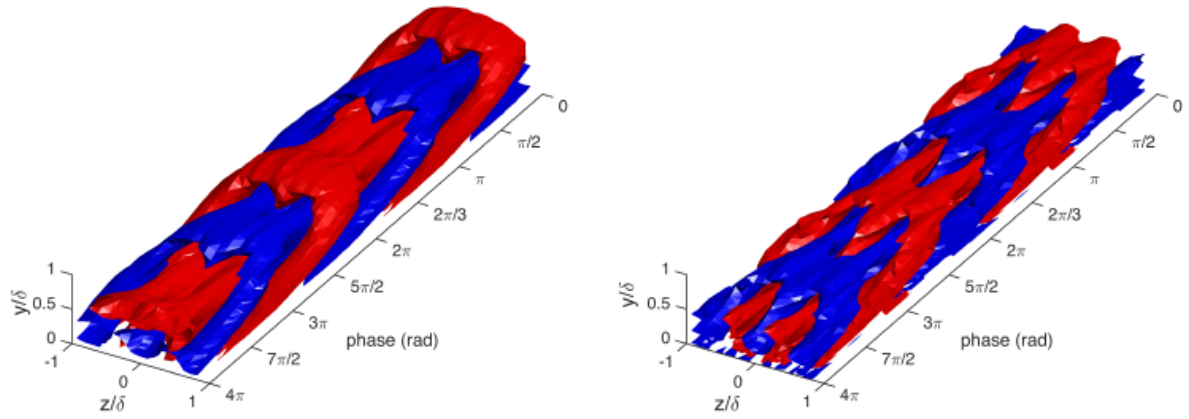

(a) $St = 0.5, r = 0.88$. (b) $St = 1, r = 0.88$.

Figure 2.17: Variation of the phase-locked velocity $\tilde{U}(y, z, \phi)$ normalilzed by the freestream velocity at $x = 5\delta$ over two complete cycles. Red and blue contours are set at $\pm\sigma/2$ of the fluctuations considered over the two-dimensional plane.

2.3.6 Skin Friction Measurements

The skin friction downstream of the synthetic jets was measured using two methods, oil film interferometry and by means of the Clauser chart. The first is a direct shear stress measurement technique. It is based on the motion of a film of oil applied to the boundary layer plate and the motion of the oil is quantified by measuring the height of the oil film by determining the spacing of light interference patterns, based on the methodology of Naughton [31]. However, it was found that this method requires a minimum quality of the fringes (light interference patterns), which was not met for the data obtained at $x/\delta = 5$. Alternatively, the skin friction coefficient can be determined by fitting

$$\frac{U}{U_\tau} = \frac{1}{\kappa} \ln\left(\frac{yU_\tau}{\nu}\right) + B, \tag{2.5}$$

to the logarithmic region of the boundary layer profile, see for example Figure 2.9. As shown by Hanson & Ganapathisubramani [18], such a method can apply to a perturbed boundary layer, albeit with caution. The skin friction coefficient, c_f, is related to the friction velocity by $c_f = \tau_w/(0.5\rho U_\infty^2)$, where $U_\tau = (\tau_w/\rho)^{1/2}$.

At $x/\delta = 1.5$, the results of the oil film interferometry method are shown in Figure 2.18a. It is evident that the boundary layer exhibits a net increase in skin friction. The Clauser chart method was not attempted at this location since the boundary layer distortion was large, and specifically the logarithmic region was highly disrupted. The increase in shear stress appears to be consistent with the increase in near-wall velocity excess, as shown in Figure 2.10. Comparatively, the behaviour of the skin friction is drastically different at $x/\delta = 5$, as shown in Figure 2.18b. The Clauser chart method was employed here. The trends shown in Figure 2.18b correlate well with the observation of the near-wall change in velocity

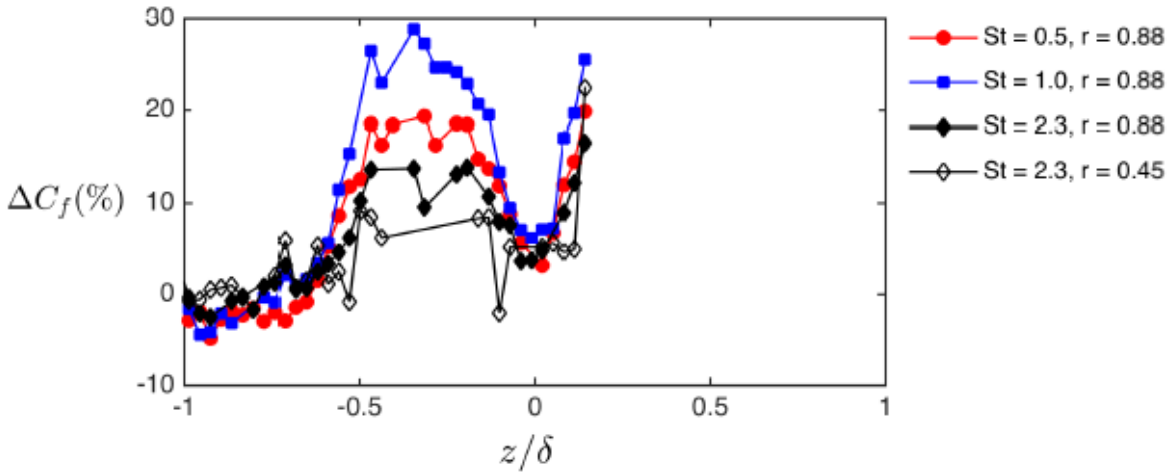

(a) $x/\delta = 1.5$ oil film interferometry data.

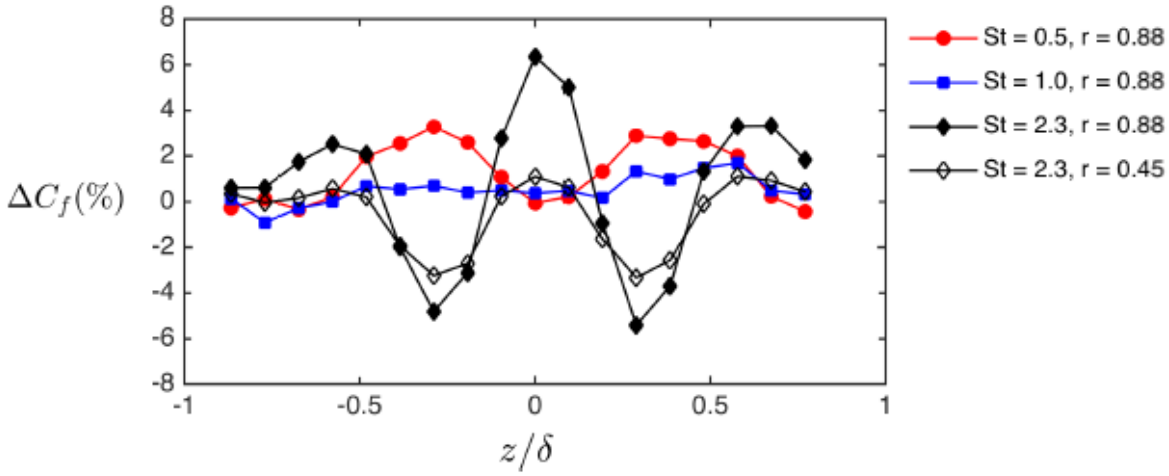

(b) $x/\delta = 5$ Clauser chart measurements of the skin friction.

Figure 2.18: Variation of the skin friction downstream of the pair of synthetic jets. Oil film interferometry data is considered at $x/\delta = 1.5$ where the boundary layer is highly distorted. At $x/\delta = 5$ the skin friction was determined using the Clauser chart method.

shown in Figure 2.10. For example, an excess in velocity was found near the wall and above the jets at $z = \pm 0.3\delta$, corresponding with the increased shear shown in Figure 2.18b for $St = 0.5$ and 1. Conversely at $St = 2.3$, a velocity deficit occurred at this location and a corresponding decrease in skin friction was observed; see Figure 2.18b. An interesting point observed is that for the case having $St = 2.3$ and $r = 0.45$ there appears to be a net drag reduction at $x/\delta = 5$. It will be shown in Section 2.4.3 that this case does not in fact result in a net skin friction reduction when considering the entire region downstream of the jets.

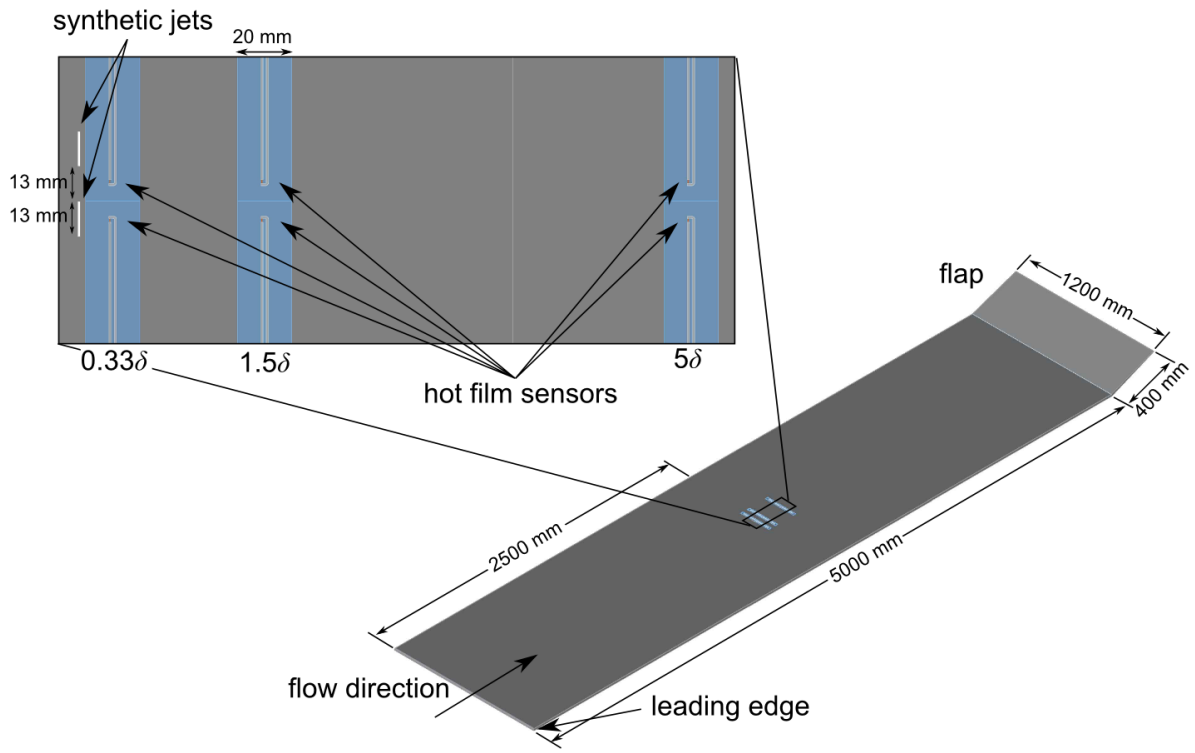

Figure 2.19: Locations of the 6 hot film sensors on the flat plate.

2.4 Skin-Friction Parameter Mapping Experiments

To determine the optimal forcing conditions of a synthetic jet on a turbulent boundary layer for skin friction reduction, a large parameter space was measured. In particular, we investigated the effect of three parameters; Strouhal number, St, blowing ratio, r, and jet spacing, Δ, on skin friction coefficient, c_f, where Δ here is the center-to-center spacing of the jets. In particular the Strouhal numbers tested ranged from 0.04 to 2.8, while the blowing ratios ranged from 0.1 to 1.4. Not all blowing ratios were achievable for a particular Strouhal number owing to the fact that the synthetic jet has output limits that vary with frequency (i.e. Strouhal number; see the synthetic jet calibrations in Section 2.2.4). Aside from the nominal jet spacing of $\Delta = 26$ mm, two other jet spacings were also investigated, namely 19.5 mm, and 32.5 mm. These experiments were run with the same baseline flowfield as the detailed hot-wire measurements in Section 2.3.1 and resulted in similar conditions.

At each set of forcing conditions (St, r, Δ), the shear stress was measured, and the change in skin friction coefficient, Δc_f, calculated with respect to a baseline value recorded before and after each measurement with the actuation turned off. Hot-films were chosen for these experiments because they are inexpensive, have the flexibility to be placed anywhere on the flat plate without requiring any specialized equipment or modifications to the model, and can measure the mean shear stress quickly for a number of forcing

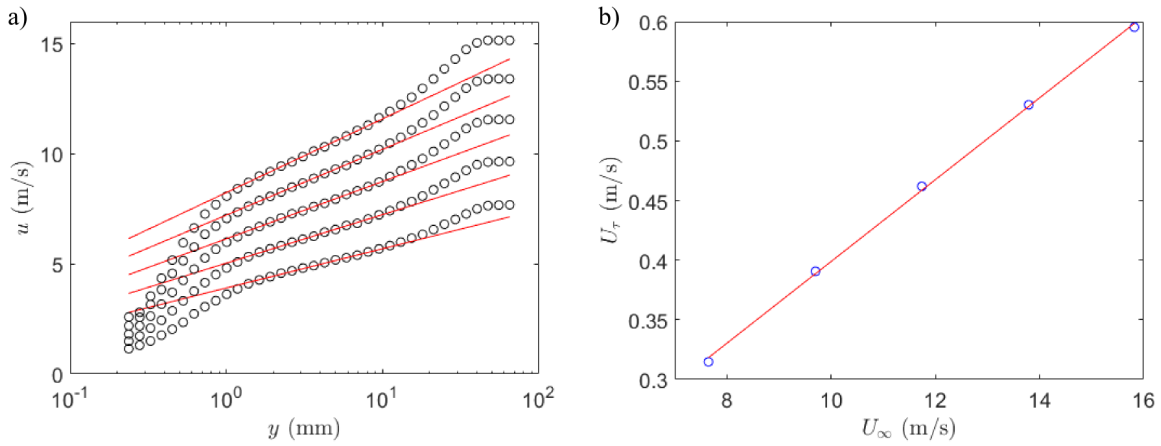

Figure 2.20: Shear stress calibration procedure. a) Boundary layer profiles are taken for a range of freestream velocities and fitted to extract U_τ. b) A calibration curve is created relating U_∞ to U_τ.

conditions. These hot-films were placed at 6 locations downstream of a pair of synthetic jets, consisting of 3 streamwise locations (0.33δ, 1.5δ, and 5δ downstream) by 2 spanwise locations (behind the jets, and behind the space between the jets), as is shown in Figure 2.19. Since hot-films are notorious for having a large thermal drift over time, they need to be recalibrated quite often. The procedure for calibrating the hot-films is detailed below.

2.4.1 Shear Stress Calibration

The first step in the hot-film calibration procedure is to calibrate the wall shear stress with the freestream velocity. To accomplish this, a boundary layer profile is taken with a hot-wire probe at a range of different freestream velocities from about 7 m/s to $1.5U_\infty$. Each boundary layer profile is then fit with the Clauser chart method shown in Section 2.3.6 and the skin-friction velocity, U_τ, is extracted as in Figure 2.20a. This gives the skin-friction velocity as a function of freestream velocity and we can create a calibration curve from a fit, as is seen in Figure 2.20b. The expected dependence for this curve can be determined from the empirical formula for c_f on a flat plate turbulent boundary layer; $c_f = 0.0592/Re_x^{1/5}$ [4], and using $U_\tau = U_\infty\sqrt{c_f/2}$, where $Re_x = xU_\infty/\nu$. At $x = 2.5$ m downstream of the leading edge, this results in $U_\tau = 0.052U_\infty^{9/10}$. Experimentally, we achieve a very similar fit; $U_\tau = 0.047U_\infty^{9/10}$. This procedure is done at the location of each hot-film to facilitate calibration of each hot-film individually. This shear-stress calibration is done once at the beginning of all measurements and then is not required again.

The lower bound of freestream velocities (i.e. 7 m/s) given above represents the lowest freestream velocity at which we obtained a turbulent boundary layer. Below this velocity, the zig-zag trip at the leading edge is no longer effective at tripping the flow to turbulence, and the flow remains laminar.

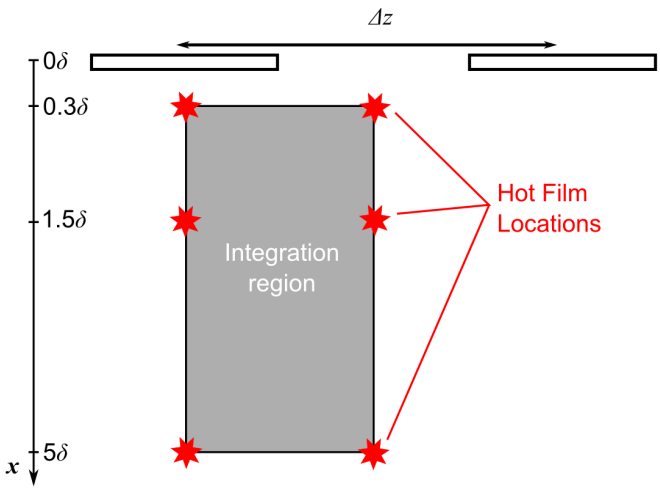

Figure 2.21: Integration region for caluclating the integrated Δc_f from the hot-films. The gray shaded area is the integration area bounded by the hot-film locations in red.

2.4.2 Hot-Film Measurement and Calibration

The output signal for a hot-film is the voltage required to keep the hot-films operating at a constant temperature. Calibration of the hot-films requires obtaining a relationship between the hot-film voltage and the shear stress. This is done by measuring the hot-film voltage at a range of freestream velocities, similar to what was done for the shear stress calibration. Since we have already determined the relationship between the shear stress and the freestream velocity, we can combine the two to plot the shear stress as a function of hot film voltage and extract the parameters of a linear fit. Such a calibration is done simultaneously for all of the hot-films directly before and after each measurement of the mean wall shear stress. Thus, for any hot-film voltage, we can determine the associated wall shear stress (practically we determine skin-friction velocity, but we can easily calculate wall shear stress from $\tau_w = \rho U_\tau^2$) from which we can extract the skin friction coefficient c_f from $c_f = \tau_w/(1/2\rho U_\infty^2) = 2(U_\tau/U_\infty)^2$.

Typical measurements of the hot film voltage at one set of actuation conditions were conducted before, during, and after actuation. The voltage time series before and after actuation were averaged to get the mean offset, and then converted to a c_f value, namely the offset skin friction coefficient c_{f_0}, which is the measured unactuated skin friction coefficient. The hot film voltage during actuation was also averaged and converted to a c_f value. We then simply calculated Δc_f from $\Delta c_f = (c_f - c_{f_0})/c_{f_0}$, and expressed the result as a percent. This procedure was done simultaneously for each of the 6 hot films on the flat plate, giving us the Δc_f at each location. To get an estimate of the drag reduction over the region bounded by the 6 points, a simple trapezoidal integration was used, giving the integrated Δc_f. This integration region is shown in Figure 2.21. Measurements and integrations were done for each set of actuation conditions, and a contour map of integrated Δc_f was constructed for each of the three jet spacings.

There are a number of limitations of using six points and using a trapezoidal integration. First, the trapezoidal rule is based on a linear approximation between points. While this may be a reasonable approximation between the four points at the furthest downstream locations ($x/\delta = 1.5$, and $x/\delta = 5$), this is certainly not true for the points at $x/\delta = 0.33$. The simulations below show that Δc_f can change very rapidly between $x/\delta = 0.33$ and $x/\delta = 1.5$ downstream of the jets and behind the jet centerline, as well as between the two points at $x = 0.33\delta$. Second, since the gradients of Δc_f are large close to the jet, having skin friction measurement points too far apart has the effect of overestimating the magnitude of the integrated Δc_f. This overestimation can become greater if the spacing between the jets is increased (i.e. increased spanwise distance between measurement points) and the Δc_f profile downstream of each jet remains unchanged. Third, since we only have six points, it is possible that we miss regions that have a significant effect on Δc_f. In particular, the simulations below show that the edges of the jets have a significant effect, as for $0 < x/\delta < 0.3$.

There is also a limitation to using hot films to calculate Δc_f. Since hot films measure wall shear stress by the transfer of heat at the wall, they are unable to distinguish whether fluid moving upstream or downstream is causing the shear stress. As a consequence, the hot-film signal is rectified. In most cases this is not an issue since τ_w, and hence c_f, point downstream. However, when the synthetic jets are actuating, it is possible for a small recirculation region to develop just downstream of the jet. Such a recirculation region is due to flow moving over the viscous blockage created by the jet, similar to a backward facing step. Thus, over one jet cycle, the τ_w, and hence c_f goes from a positive value (downstream) during the suction half of the cycle, to negative (upstream) during the blowing half of the cycle. Since the hot film signal is rectified, we end up with a positive c_f over the entire cycle. Thus, some Δc_f values associated with the nearest downstream sensor behind the jet will be overestimated, resulting in overestimated integrated Δc_f values.

2.4.3 Two jets, $Re_\Theta \approx 3230$, $\Delta = 26$ mm spacing

To deal with the rectification issue, we need to flip the sign of the c_f values that we get during the blowing half of the cycle where it is apparent that rectification has occured. Practically, this only occurs for the hot film at the nearest streamwise distance behind the jet, 0.33δ, and directly behind the jet. In Figure 2.22, we compare three different Strouhal numbers and notice that not all require derectification. We can clearly see the rectification if we look at phase-averaged hot film signals with increasing blowing ratio at low Strouhal numbers, as in Figure 2.22a for blowing ratios $r \geq 0.1$, while in Figure 2.22c, at higher Strouhal number it does not look like any of the cases require derectification. At intermediate Strouhal numbers, such as Figure 2.22b, the blowing half of the cycle has much more character than at either low Strouhal number or high Strouhal number. This could be due the presence of harmonics, as we are close to the speaker

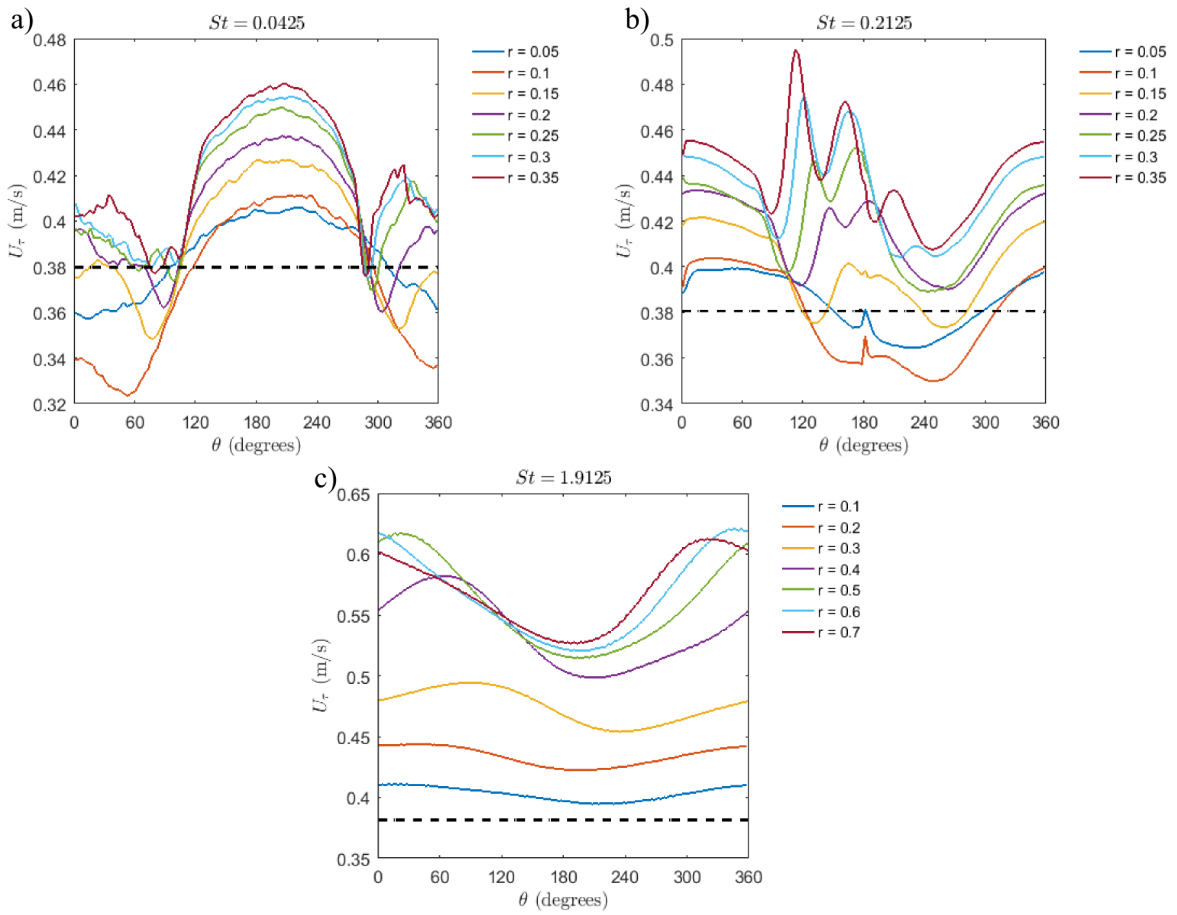

Figure 2.22: Phase-averaged U_τ for a range of blowing ratios at Strouhal numbers of a) 0.0425, b) 0.2125, and c) 1.9125.

resonance at these Strouhal numbers, or it could indeed be a physical effect of the jets on the shear stress. For these Strouhal number cases it is difficult to tell if derectification is required. Note that the suction peak is always the smoother of the two peaks in Figure 2.22(a-c), and occurs at $\phi \approx 180°$ for $St = 0.0425$, $\phi \approx 0°$ for $St = 0.2125$, and $\phi \approx 60°$ for $St = 1.9125$. In the contour plots that follow, we select the regions that appear to switch sign in c_f and derectify them before taking the time-average. While this is an inexact method, it likely gives a better indication of the actual integrated Δc_f. It should be noted here that strictly flipping the regions where rectification has occurred is not always accurate. Consider the case when the actual phase-averaged c_f goes to zero during part of the cycle. In this case, the individual data points making up particular phase-averaged points close to zero consist of both positive and negative values, but their average is zero. However, the rectified version of this contains a non-zero positive offset at those locations because all negative values in the average are made positive. Derectifying the rectified hot film data would result in a negative c_f value at these locations when it should, in fact, be zero.

As an initial test of the results of the hot films, we can compare with the skin friction results from both oil film interferometry and the Clauser chart method in Section 2.3.6. The Δc_f for the cases most

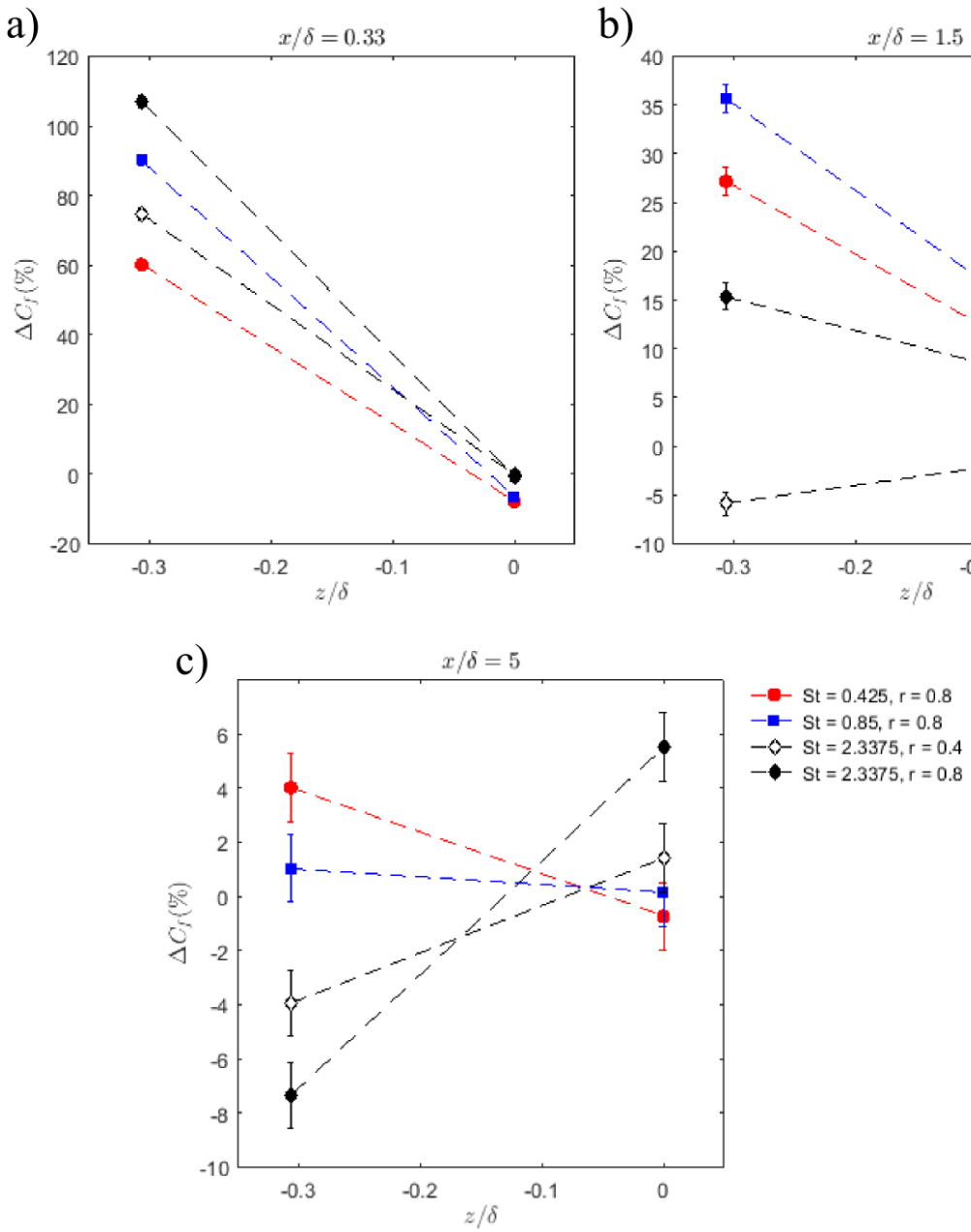

Figure 2.23: Hot film measured Δc_f at the three streamwise locations for the cases in Figure 2.18. The color and shape of the markers matches those in Figure 2.18

closely matching the cases in Section 2.3.6 are presented in Figure 2.23. As can be seen, the results show very good agreement with both the results from OFI at $x = 1.5\delta$ and the Clauser chart method at $x = 5\delta$; showing both the same trends, as well as similar magnitudes. The presence of a large increase in skin friction at the nearest streamwise station to the jets, $x = 0.33\delta$, results in all of these cases having a net skin friction increase over the integration area.

The contour map for the $\Delta = 26$ mm spacing is shown in Figure 2.24. Here, it is clear that there

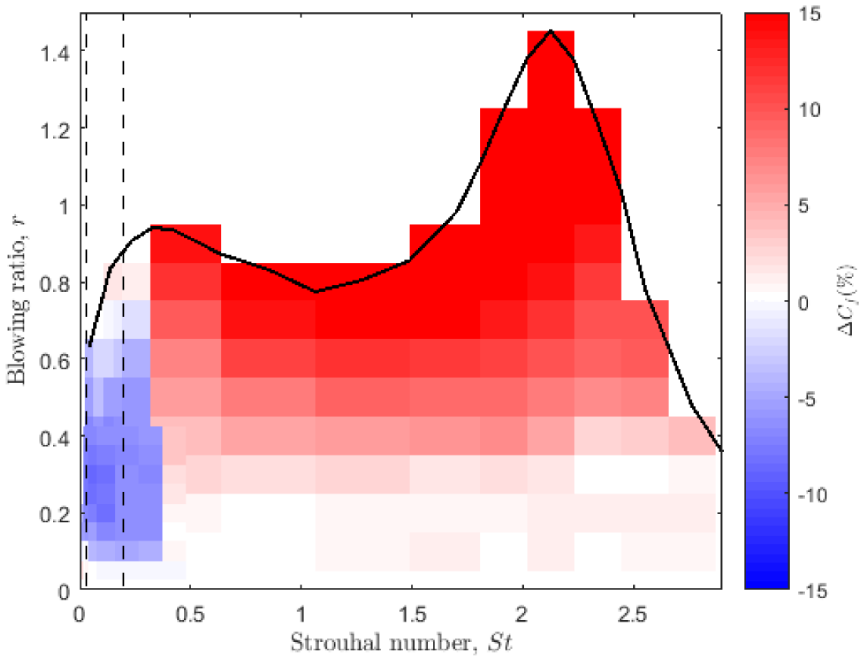

Figure 2.24: Contour map of derectified, integrated Δc_f for $\Delta = 26$ mm. The dashed lines roughly indicate the range of Strouhal numbers associated with large-scale motions in the log-layer. The thick black line indicates the maximum jet output.

is a region of skin friction drag reduction at both low Strouhal number and at low blowing ratio. This region is centered at St$\approx$ 0.04 and $r = 0.3$ with $\Delta c_f \approx -8\%$, and extends from $r = 0.1$ to $r = 0.7$ and from $St \approx 0.01$ to $St \approx 0.4$. Furthermore, we can see that Δc_f increases with increased blowing ratio, and increases slightly with Strouhal number above $St \approx 0.4$.

The outer site in the streamwise velocity spectrum associated with the large scale coherent structures has been shown to be situated at a wall-normal location of $y \approx 0.06\delta$ with a characteristic streamwise length scale of $\lambda_x \approx 6\delta$. Hutchins & Marusic have shown that this characteristic length scale is underestimated due to the spanwise meandering of these structures, and that they can extend up to $\sim 20\delta$ [21]. Since the convection velocity at a wall-normal height of $y = 0.06\delta$ is $U/U\infty \approx 0.6$, we can thus expect Strouhal numbers pertaining to the large scale turbulent motions in the log-region to be $St \approx 0.03 - 0.1$. These Strouhal numbers largely coincide with the region of skin friction reduction that we notice in the contour map, and are indicated by the black dashed lines in Figure 2.24. Further experimental work is required to dertermine the effect on the large scale motions at these forcing conditions.

2.4.4 Two jets, $Re_\Theta \approx 3230$, $\Delta = 19.5$ mm spacing

The contour map for the $\Delta = 19.5$ mm spacing is shown in Figure 2.25. This contour map appears very similar to the one for the $\Delta = 26$ mm case. Again, the region of reduced skin-friction is at low blowing

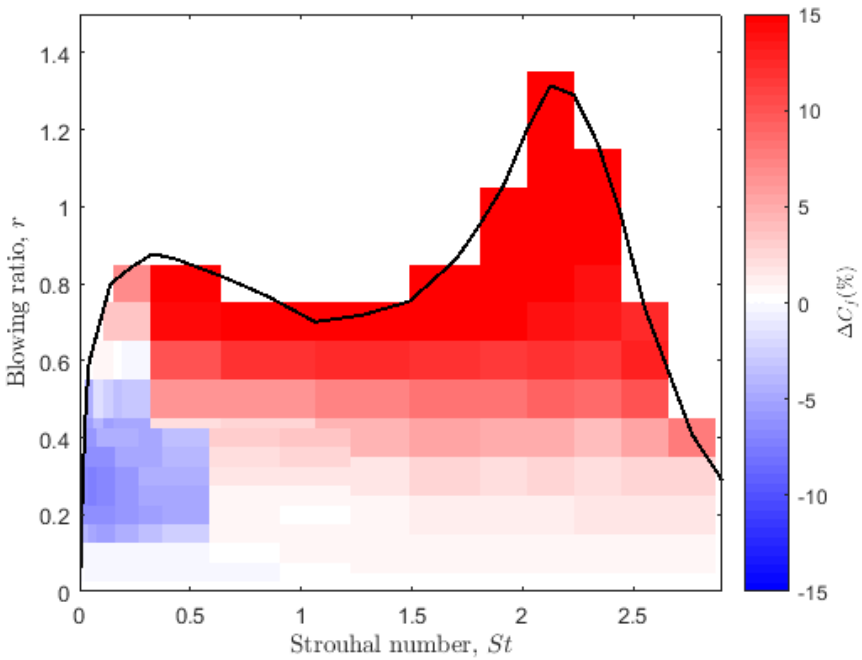

Figure 2.25: Contour map of derectified, integrated Δc_f for $\Delta = 19.5$ mm.

ratio and low Strouhal number, and there is also an increase in skin friction as blowing ratio increases. The lone differences are that the region of reduced skin frction extends to slightly higher Strouhal numbers and is centred at $St \approx 0.03$, and $r = 0.25$.

2.4.5 Two jets, $Re_\Theta \approx 3230$, $\Delta = 32.5$ mm spacing

The contour map for the $\Delta = 32.5$ mm spacing is shown in Figure 2.26. This contour map also appears very similar to those for the $\Delta = 26$ mm and $\Delta = 19.5$ mm cases. The region of reduced skin friction is largely the same as for the other two cases, but the location of largest skin friction reduction is $St \approx 0.4$ and $r = 0.25$ with a reduction of about $\sim 10\%$. There is now also a large region of slightly reduced skin friction at low blowing ratios across all Strouhal numbers.

With a trapezoidal integration, it is possible for magnitudes to be overestimated, as is discussed above. Furthermore, the main contribution to the integrated Δc_f for these cases is a reduction in c_f directly behind the jets at the nearest downstream location ($x = 0.33\delta$), which is not seen for the other two spacings. This is not intuitive, as one might expect the reduction to be related to the region between the jets.

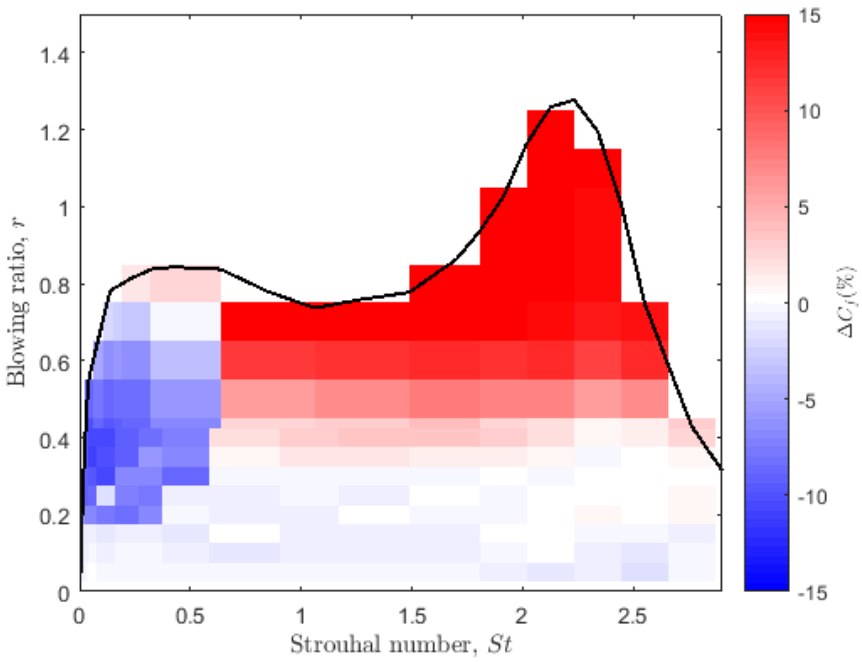

Figure 2.26: Contour map of derectified, integrated Δc_f for $\Delta = 32.5$ mm.

2.5 Hot-Wire Measurements of Boundary Layers Actuated at Low Frequency

Following the experimental results presented thus far, a change in the synthetic jet forcing frequency was made. Considering the spectrograms shown in Figure 2.12 and that low-frequency forcing was found to be more robust, the actuators were designed to accommodate lower forcing frequencies. Practically this required a larger diameter loud-speaker to produce a low frequency synthetic jet. A Visaton KT 100 V loud-speaker that had significant output response down to nearly 10 Hz was selected. The 3D-printed jet orifices could be kept, but new speaker mounts were manufactured to accommodate the large diameter loud-speakers. An example of the spectra obtained downstream of the jet for a case with $U_\infty/(f\delta) = 13$ ($St = 0.077$), and $r = 0.68$ is shown in Figure 2.27 at $x/\delta = 3$. From this figure it can be observed that the forcing frequency is lower than the frequency of the near wall peak, which allows isolation of the near wall dynamics using spectral filtering techniques.

An example of the isosurface produced by an isolated jet at low-frequency is shown in Figure 2.28. For this case $U_\infty/(f\delta) = 13$ ($St = 0.077$), and $r = 0.68$. The blue velocity deficit at 3π, for example, appears to be associated with the jet blowing cycle, whereas the region of velocity excess at approximately 2π appears to be caused by the suction cycle of the actuator where high-velocity fluid in the boundary layer is drawn toward the wall.

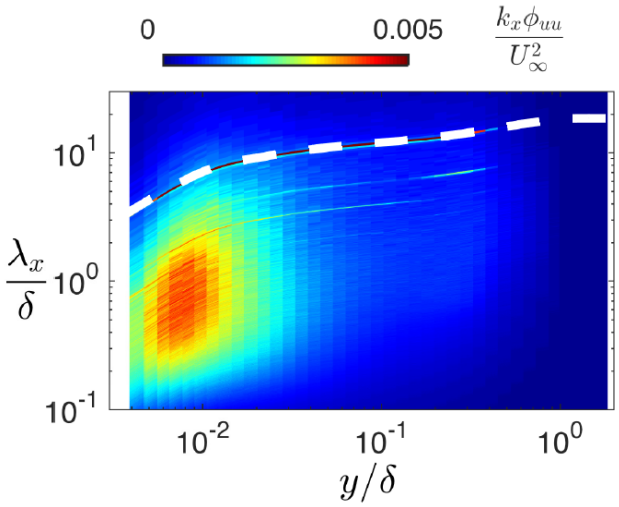

Figure 2.27: The pre-multiplied spectrogram of $k_x(\phi_{uu}/U_\infty^2)$ for the case with $U_\infty/(f\delta) = 13$, or $St = 0.077$, and $r = 0.68$. The dashed line highlights the forcing frequency in terms of the wavenumber across the boundary layer.

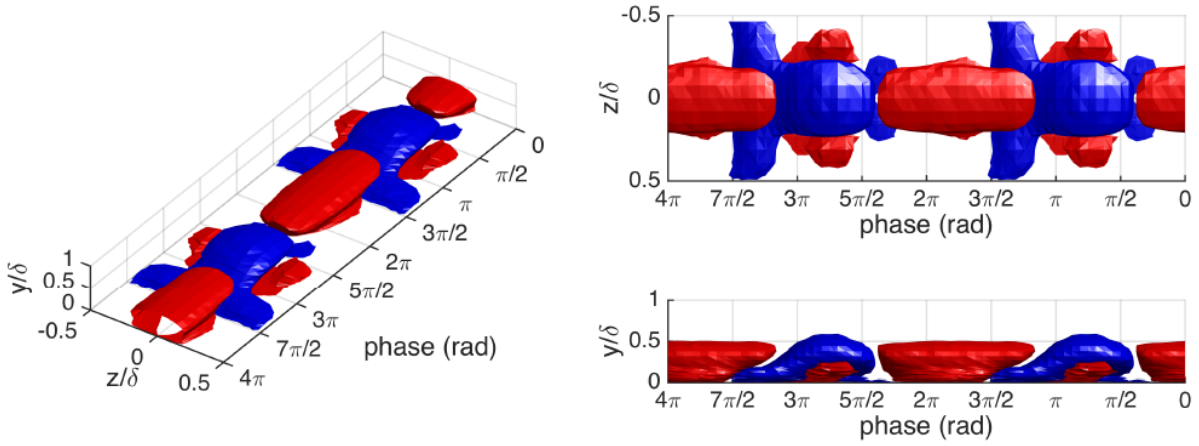

Figure 2.28: Variation of the phase-locked velocity $\tilde{U}(y, z, \phi)$ normalized by the freestream velocity at $x = 3\delta$ over two complete cycles. Red and blue contours are set at $\pm\sigma/2$ of the fluctuations considered over the two-dimensional plane.

By means of a spectral filter, the high-pass signal can be analyzed without including the unsteady dynamics input directly by the synthetic jets. The high-pass turbulent response is shown for two blowing ratio cases in Figure 2.29. It can be observed that the turbulent near-wall peak is essentially modulated by the large outer-region structures input by the synthetic jets. The dynamics of this structure are shown by the bottom plane included in this figure which plots velocity defect as a function of phase and wall-normal position, which is computed as shown previously in Figure 2.14. Examining Figure 2.29 shows that beneath the velocity deficit imparted by the synthetic jet the turbulent near-wall peak is suppressed, whereas this peak increases in magnitude with the passage of a velocity excess. Comparing the two different blowing

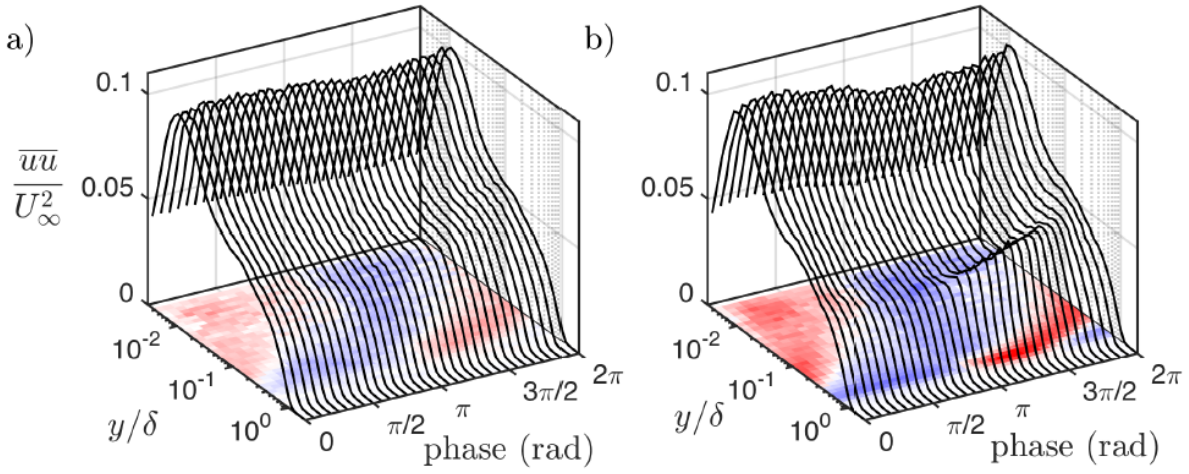

Figure 2.29: Variation of the phase-locked velocity $\tilde{U}(y, z, \phi)$ shown by the contours of excess (red) and deficit (blue) and line plots showing the variation of the high-pass turbulence intensity for a low (a) ($r = 0.3$) and high (b) ($r = 0.68$) blowing ratio.

ratios, it can be observed that this effect becomes enhanced with increasing blowing ratio.

2.6 Conclusion of Experimental Studies

Results from two experimental campaigns, were presented to show the effect of synthetic jet forcing on the flow fiield and, more importantly, the skin friction downstream. From the time resolved data, spectrograms were used to demonstrate the temporal dynamics of the boundary layer and features of the near-wall turbulence and phase-locked behaviour of the synthetic jet disturbance. It was shown that the flow is highly receptive to low-frequency (low Strouhal number) forcing. Comparatively, at a high Strouhal number, the dynamics found at low frequencies does not manifest in the far-field of the synthetic jets. This significant result suggests that low-frequency forcing is required to manipulate the boundary layer dynamically in an effective and persistent manner.

Furthermore, skin friction measurements at six locations downstream of the synthetic jets were presented to show the effect of Strouhal number, blowing ratio, and jet spacing on skin friction. These results show that for all jet spacings there is a region of skin friction reduction at both low to moderate blowing ratios, and low Strouhal numbers. These results also suggest that low-frequency forcing is necessary to effectively manipulate the boundary layer to achieve skin-friction reduction

Results from a third dataset have been presented to understand the forcing at low frequency or low Strouhal number. These measurements indicate that low frequency forcing causes an amplitude modulation on the near wall peak in the streamwise turbulence intensity.

Chapter 3

Numerical Studies

Pieter Boom and David Zingg

List of Symbols

A Forcing velocity amplitude

C Log law constant

C^0 Denotes a continuous function

e Energy

c_f Skin-friction coefficient

$\bar{f}$ Nondimensional forcing frequency

H Shape factor

j, k, m, n Array indices

K Acceleration parameter

M Mach number

N_x, N_y, N_z Number of computational nodes in each coordinate direction: streamwise, wall-normal and chordwise directions, respectively

N_{tot} Total number of computational nodes

q_1, q_2, q_3, q_4, q_5 Array dummy variable names

Q Vector of conservative flow variables

r blowing ratio

Re_θ Momentum thickness Reynolds number

Re_τ Friction velocity Reynolds number

St Strouhal number

Δt Time step size

$\bar{t}$ Nondimensional time

u, v, w Velocity components in the streamwise, wall-normal and chordwise directions, respectively

u', v', w' Fluctuation velocity components in the streamwise, wall-normal and chordwise directions, respectively

$|u'|_{\mathbf{rms}}$ Root mean square of streamwise fluctuation velocity

U, V, W Mean velocity components in the streamwise, wall-normal and chordwise directions, respectively

U_0 Freestream streamwise velocity

U_e Boundary layer edge velocity

u_τ Friction velocity

u^+ Turbulence scaled velocity

$\mathcal{W}$ Recycling weight function

x, y, z Coordinate directions in streamwise, wall-normal and chordwise directions, respectively

x^+, y^+, z^+ Turbulence scaled distances in each coordinate directions: streamwise, wall-normal and chordwise directions, respectively

δ, δ_{99} 99% boundary layer thickness

δ^* Displacement thickness

$\delta_\circ$ Reference 99% boundary layer thickness in computations

η Wall-normal distance scaled by 99% boundary layer thickness

κ Log law constant

ν Kinematic viscosity

ω_x, ω_y, ω_z Vorticity in each coordinate directions: streamwise, wall-normal and chordwise directions, respectively

ρ Density

θ Momentum thickness

ξ, η, ζ Computational coordinate directions

$\bar{\square}$ Averaged quantity

3.1 Introduction

The primary role of the computations is to support the experimental campaign, providing additional details of the flow and change in skin friction drag for a limited number of controlled and uncontrolled cases. Furthermore, it provides further insights and verification of the experimental results. Good agreement between experiments and computations increases the confidence in both. The results presented in this report are obtained primarily using implicit large-eddy simulation (LES). Direct numerical simulation (DNS) is presented at the lower Reynolds number, $Re_\theta = 1500$.

3.2 Diablo Flow Solver

Numerical simulations are carried out using the three-dimensional compressible Navier-Stokes flow solver developed in the Computational Aerodynamics group at UTIAS called DIABLO. The spatial discretization is obtained using high-order finite-difference summation-by-parts (SBP) operators on C^0 continuous structured multiblock grids. Boundary conditions and interblock coupling are weakly enforced with simultaneous approximation terms (SATs). The discretization is stabilized with high-order matrix artificial dissipation compatible with the SBP-SAT approach. The spatial discretization is globally fourth-order accurate in all simulations. Temporal integration is obtained with explicit-first-stage singly-diagonally-implicit Runge-Kutta (ESDIRK) methods. Both second and fourth-order variants are used in the simulations, depending on the case. Additional details of the flow solver can be found in [6, 10, 19, 33, 34].

3.3 Simulation Domain and Boundary Conditions

Figure 3.1 shows a schematic of the computational domain and boundary conditions. The reference length scale is the target 99% boundary-layer thickness at the beginning of the working region, $\delta_\circ$. Using this

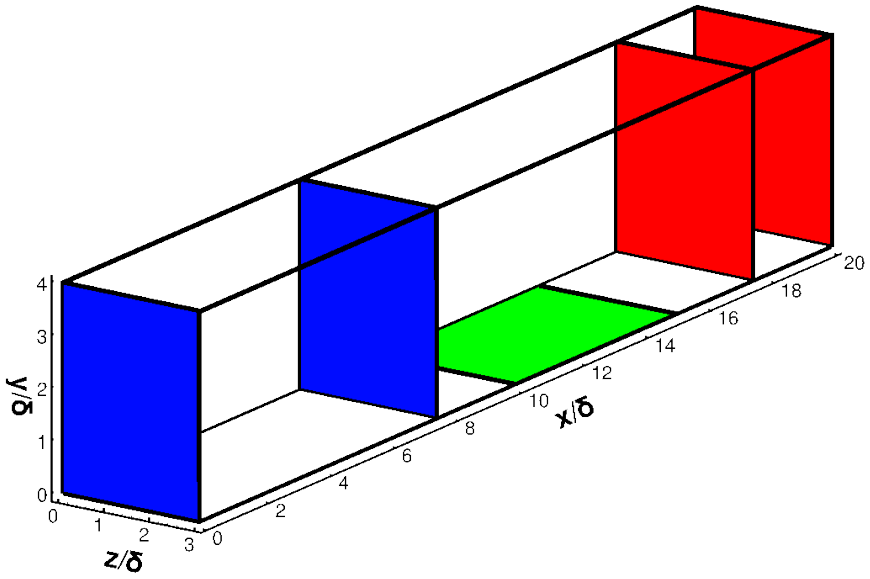

Figure 3.1: Computational domain and boundary conditions. Blue planes denote inflow and recycle planes. Red planes denote the convective outflow plane and the reference plane where the convection velocity is computed. The green region denotes the working region. The synthetic jets are placed at the beginning of this working region.

reference, the size of the computational domain is $(20\times4\times3)\delta_\circ$ in the streamwise, wall-normal, and spanwise directions, respectively. The working region spans $x \in [10, 15]\delta_\circ$ in order to minimize the influence of the artificial inflow and outflow boundary conditions. Likewise, the spanwise dimension was chosen to minimize the interaction of a pair of synthetic jets across the spanwise periodic boundaries.

The flat plate is simulated with a no-slip adiabatic wall boundary condition using a high-order SBP approximation of the temperature gradient. To avoid simulating the entire synthetic jet (Slot, cavity, and diaphragm), a velocity boundary condition is imposed at the base of the slot to model the diaphragm and cavity. The turbulent inflow data is generated using the recycle/rescale approach proposed by Lund *et al* [25] and the compressible extension for density and temperature presented in Stolz and Adams [47]. Based on the target Re_θ, empirical relationships are used to determine the simulation Reynolds number $Re_{\delta_\circ}$ and the inlet boundary-layer thickness for the rescaling procedure. The Re_θ realized during the simulations often differs a bit from the target Re_θ; however, this is not surprising given the empirical relationships used. The recycle plane is located between $x = 7\delta_\circ$ and $x = 7.5\delta_\circ$, depending on the simulation, to minimize errors introduced by the recycling procedure itself and disturbances created by the synthetic jets located at $x = 10\delta_\circ$. A convective boundary condition is imposed at the outflow (see for example [13]):

$$\frac{\partial Q}{\partial t} + U\frac{\partial Q}{\partial x}\bigg|_{\text{outflow}} = 0, \tag{3.1}$$

where Q is the vector of conserved flow variables, and U is the convection velocity obtained from the mean

Simulation	Nodes				Spacing		
	N_x	N_y	N_z	N_{tot}	x^+_{max}	y^+_{min}	z^+_{max}
Uncontrolled							
ILES ($Re_\theta = 1500$)	961	129	289	$\sim 39 \times 10^6$	13	0.5	6.5
DNS ($Re_\theta = 1500$)	961	289	289	$\sim 87 \times 10^6$	13	0.5	6.5
ILES ($Re_\theta = 3230$)	513	192	385	$\sim 41 \times 10^6$	45	0.3	9
ILES ($Re_\theta = 4210$)	513	161	289	$\sim 26 \times 10^6$	54	1	14
Controlled							
ILES ($Re_\theta = 3230$)	545	192	385	$\sim 44 \times 10^6$	45	0.3	9
-slot(x2)	13	65	40	$\sim 3.4 \times 10^4$	2	0.3	9
ILES ($Re_\theta = 4210$)	545	161	289	$\sim 27 \times 10^6$	54	1	14
-slot(x1)	13	65	33	$\sim 2.8 \times 10^4$	2	1	13

Table 3.1: Grid details for the uncontrolled and controlled simulations. Note that the number of nodes given in each direction is the number of unique computational nodes in that direction; whereas the approximate total number of nodes given includes repeated nodes at block interfaces.

flow upstream of the boundary between $x = 17.5\delta_\circ$ and $x = 18\delta_\circ$, depending on the simulation. This is done to decouple the outflow condition from the solution at the boundary itself, mitigating potential instabilities. The assumption is that the mean boundary-layer properties do not vary significantly between the reference and boundary planes. At the top of the domain the velocity and pressure are extrapolated from the interior. This enables the flow to exit the domain resulting from the growing boundary layer. Finally, the spanwise walls of the computational domain are made periodic.

3.4 Computational Grids

The computational domain is discretized into an orthogonal structured multiblock mesh. The grid is equally spaced in the streamwise and spanwise directions, and has hyperbolic tangent spacing in the wall-normal direction. The mesh is decomposed into blocks of 33^3 nodes, and the solution is computed in parallel. Details regarding mesh spacing and node counts are presented in Table 3.1. A sample of the resulting block topology is shown in Figure 3.2.

In the controlled case, the grid is refined in the vicinity of the synthetic jet(s) and additional blocks are added for the slot(s). Each slot in the present simulations has dimensions $0.3\delta_\circ$ wide, $\sim 0.023\delta_\circ$ long, and $0.075\delta_\circ$ deep. A sample block topology and grid distribution near a pair of jets is shown in Figure 3.3.

3.5 Uncontrolled Zero-Pressure-Gradient Flat-Plate Boundary-Layer Simulations

The purpose of the uncontrolled simulations is to provide a reference and a starting point for the controlled simulations, as well as to verify the code. The results presented in this section were obtained predominantly

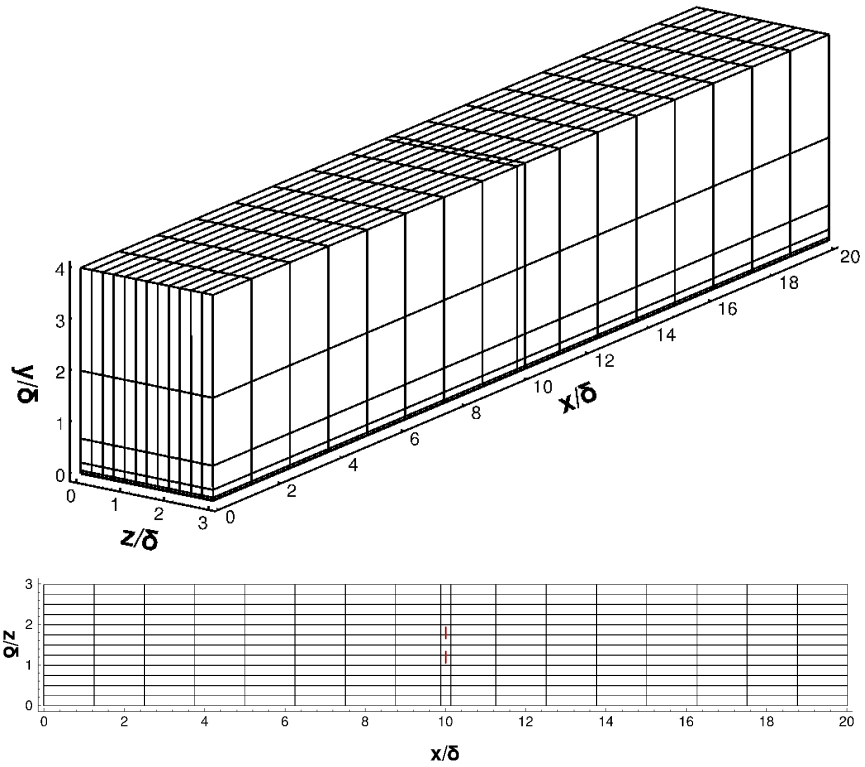

Figure 3.2: Block topology for controlled simulations.

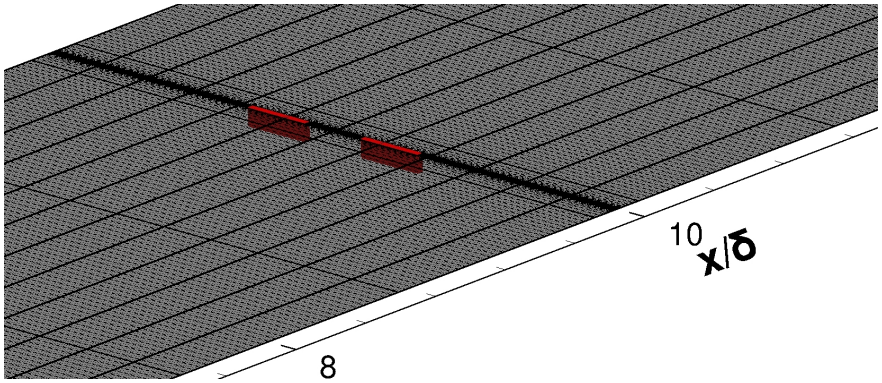

Figure 3.3: Block topology and grid near the pair of synthetic jets, with the additional blocks needed to simulate the slots shown in red.

with implicit LES. One DNS result is presented at the lower target Reynolds number of $Re_\theta = 1500$. This section evaluates a few aspects of the uncontrolled boundary layer to ensure it is replicating the intended flow. In all uncontrolled simulations the freestream Mach number is set to 0.2 to ensure that the numerical solution is well-conditioned without the use of low Mach number preconditioning. In this report we use a common decomposition of the velocity $u = u' + U$, where u' is the fluctuating component and U is the mean component of the velocity, respectively. The freestream velocity is denoted U_0.

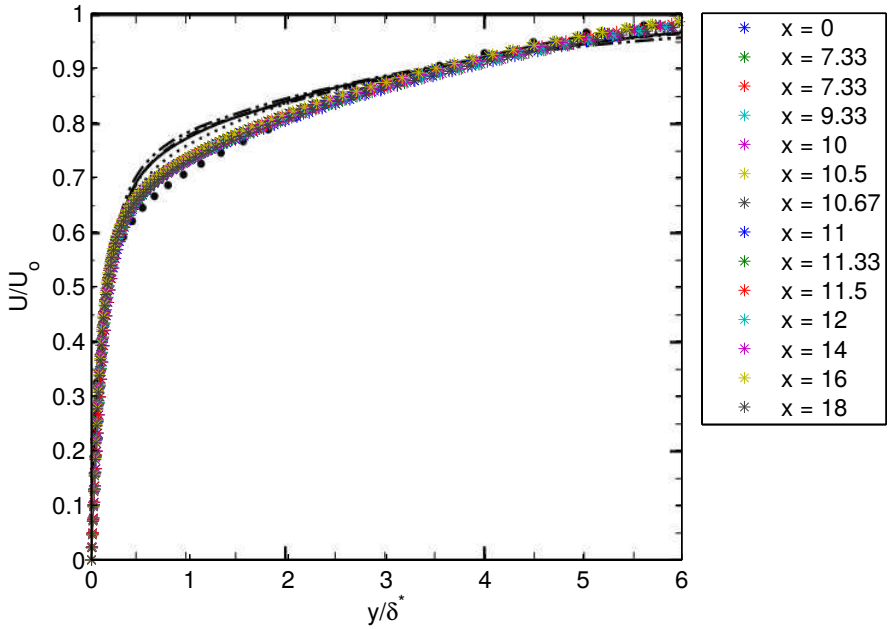

Figure 3.4: **Implicit LES -** $Re_\theta = 1500$**:** Streamwise velocity profile superimposed on the DNS of Sayadi et al. [41] at $Re_\theta = 1210$ (circles), as well as the LES of Sayadi and Moin [42] using: dynamic scale-similarity ($-\cdot-$), dynamic Smagorinsky (–), dynamic one equation kinetic energy ($-\cdots-$), global coefficient Vreman ($\cdots$), and dynamic Smagorinsky with a fine grid ($--$). The present results lie right on top of Sayadi and Moin's dynamic Smagorinsky results with a fine grid.

3.5.1 $Re_\theta = 1500$

The results in this section were obtained using fourth-order time marching and a time step of $\frac{\Delta t U_0}{\delta_\circ} = 0.04$. The Re_θ realized at the beginning of the working region is just over 1600, slightly higher than the target value set at $Re_\theta = 1500$. The Re_τ realized at the same location is over 650, the shape factor is about 1.45, and the friction velocity scaled by the freestream flow velocity is 0.0017.

Figure 3.4 shows the streamwise velocity profiles of the current simulation. These results are superimposed on the DNS results of Sayadi et al. [41] at $Re_\theta = 1210$, as well as the LES result of Sayadi and Moin [42] obtained using a variety of different subgrid models. Compared with the DNS results, the velocity in the present computations is slightly overpredicted at the knee in the curve. This behaviour was also observed in the LES results of Sayadi and Moin, affecting all of the subgrid models considered. Similar behaviour with LES models has been observed in other studies as well. Figures 3.5 and 3.6 show log-law velocity profiles from the present computations superimposed on the LES results of Schlatter [43] and Sagaut et al. [39]. The deviation in the velocity profiles begins in the buffer layer and continues through the logarithmic region, though the slope in the logarithmic region seems to be reasonably well predicted. Sayadi and Moin were able to improve the performance of the LES models, but only by significantly increasing the grid resolution. The results of the present implicit LES simulation lie very close to these fine

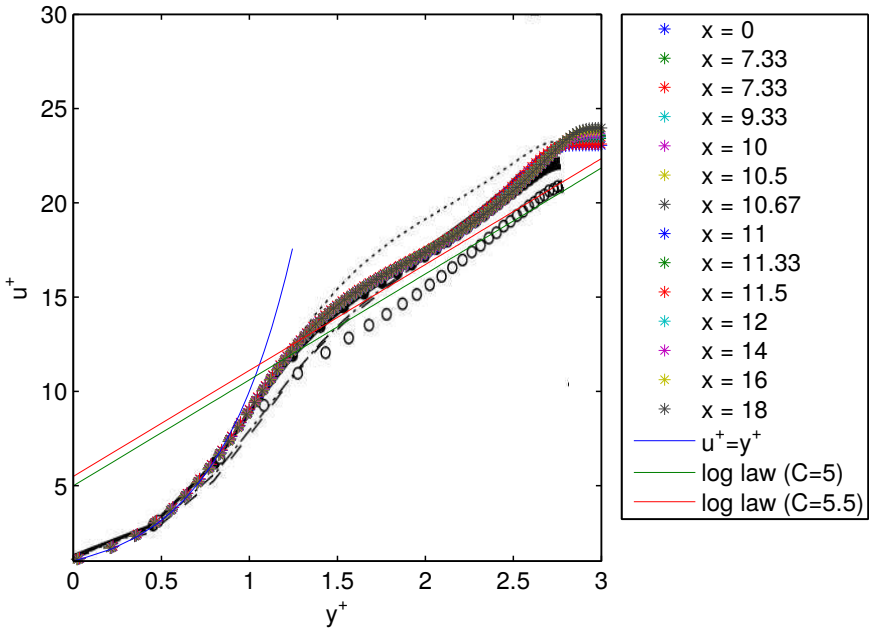

Figure 3.5: **Implicit LES -** $Re_\theta = 1500$**:** Streamwise velocity profile superimposed on the theoretical laws for the viscous sublayer and logorithmic region ($\kappa = 0.41$), along with channel flow results from Schlatter [43] at $Re_\tau \approx 500 - 600$ using: high-pass filtered structure function (thick line), high-pass filtered Smagorinsky (thin line), Smagorinksy ($--$), dynamic Smagorinsky ($\cdots$), filtered structure function ($-\cdot-$), DNS (closed circles), and implicit LES (open circles).

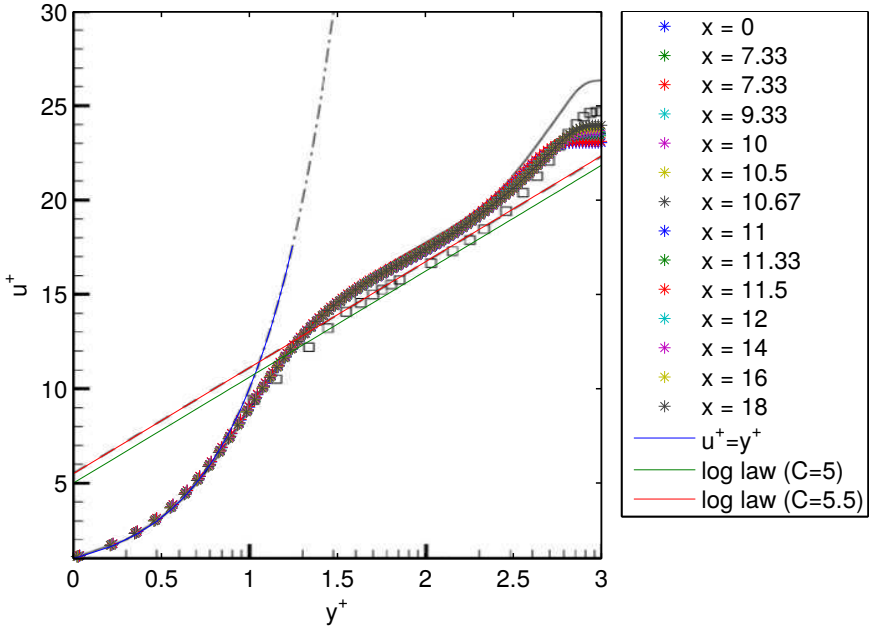

Figure 3.6: **Implicit LES -** $Re_\theta = 1500$**:** Streamwise velocity profile superimposed on the theoretical laws for the viscous sublayer and logorithmic region ($\kappa = 0.41$ with $C = 5$ and $C = 5.5$), along with the van Driest transformed supersonic flat plate LES results of Sagaut et al. [39] (thin line) and experimental results of Laurent [24] (squares).

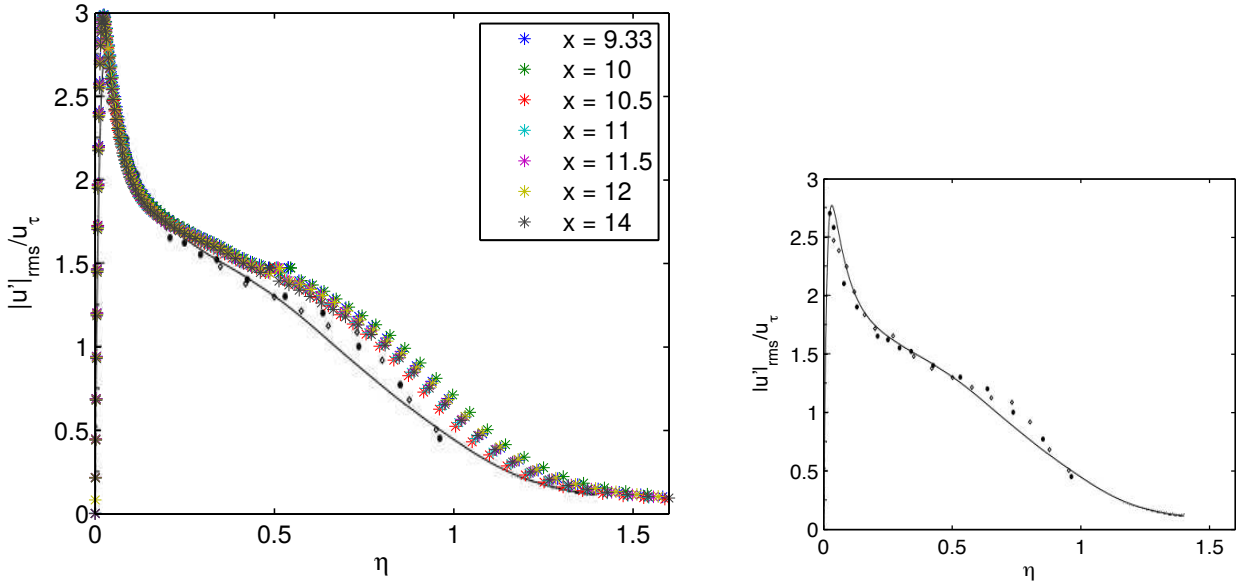

Figure 3.7: **Implicit LES -** $Re_\theta = 1500$**:** Streamwise velocity fluctuation profiles superimposed on the DNS results from Wu and Moin [49] at $Re_\theta = 900$ (thin line), the experimental results of Purtell et al.[37] at $Re_\theta = 1340$ (closed symbols), and the experimental results of Erm and Joubert [12] at $Re_\theta = 697$ (open symbols). Reference shown on the right.

grid results from Sayadi and Moin.

Consider the streamwise velocity fluctuations shown in Figure 3.7 as a function of the wall normal distance $\eta = y/\delta_{99}$. These results are superimposed on the DNS results from Wu and Moin [49] at $Re_\theta = 900$, the experimental results from Purtell et al. [37] at $Re_\theta = 1340$, and the experimental results of Erm and Joubert [12] at $Re_\theta = 697$. The present simulations overpredict the magnitude of the peak fluctuations (See the reference plot to the right). This behaviour continues through the logarithmic region, similar to the mean velocity profiles discussed above. The fluctuating velocity profile eventually reunites with the reference at the edge of the boundary layer. Note here the difference in Reynolds numbers between the reference experiments and computations, and the present implicit LES simulation. This will affect the expected profile to some extent and is discussed further in the next section.

Figure 3.8 shows the streamwise velocity fluctuations as a function of the mean velocity profile. These are referred to as diagnostic plots [1]. The top plot highlights the observed linear region in the outer part of the boundary layer superimposed on the linear fit presented in Alfredsson et al. [2]. The fluctuations exhibit the correct slope, but are a little over predicted. The plot on the bottom highlights the linear region observed near the wall superimposed on the linear fit presented in Alfredsson et al. [1]. Note the different axes. The present simulations match well with the linear fits.

The results presented above match reasonably well with experimental data and direct numerical simulations. The observed deviations are consistent with the use of LES modelling observed in the literature.

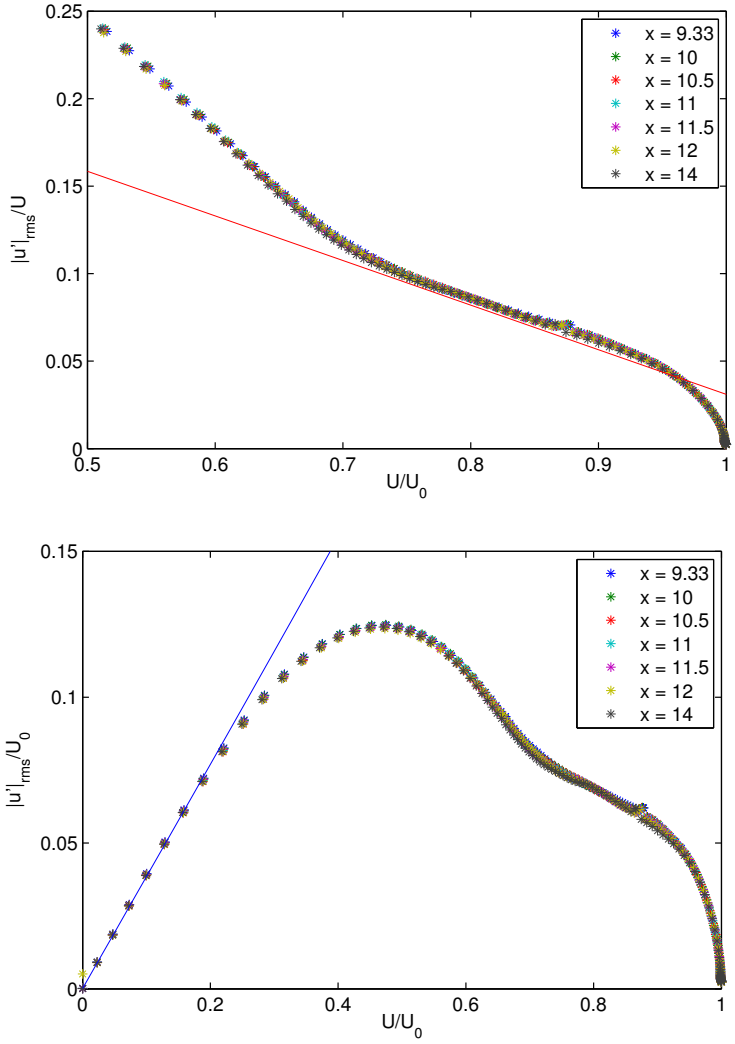

Figure 3.8: **Implicit LES -** $Re_\theta = 1500$**:** Streamwise velocity fluctuation profiles with linear fits from Alfredsson et al. [2] [top], and Alfredsson et al. [1] [bottom].

To eliminate other possible sources of error which can cause a shift in velocity profiles, we also investigated compressibility effects and the strength of any pressure gradients in the present simulations.

Compressibility can have a significant impact on the expected boundary-layer profiles, causing a shift in the law of the wall (see for example [9]). This is primarily a concern with supersonic boundary layers, but can influence subsonic flows as well (for example [48, 8]). The present simulations are performed at a higher Mach number than the experiments, $M = 0.2$, but within the incompressible regime. The influence of compressibility is expected to be negligible. Indeed the density and temperature vary by less than 2% throughout the whole domain. As further verification, the van Driest transformed log-law velocity profile was computed. Comparing the transformed and untransformed profiles yields a difference on the order of 1%. This supports the assumption that compressibility effects are negligible in the present simulations.

Favourable and adverse pressure gradients can also have a significant impact on the resulting boundary-

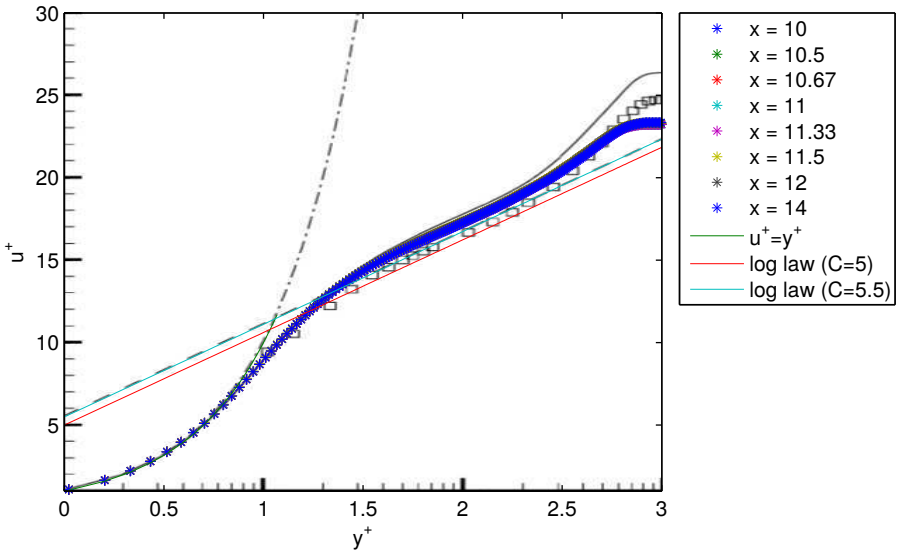

Figure 3.9: **DNS -** $Re_\theta = 1500$**:** Streamwise velocity profile superimposed on the theoretical laws for the viscous sublayer and logorithmic region ($\kappa = 0.41$), along with the van Driest transformed supersonic flat plate LES results of Sagaut et al. [39] (thin line) and experimental results of Laurent [24] (squares).

layer properties. Several artificial numerical techniques are employed in the present simulations to minimize computational effort. Any one of these approaches could introduce a pressure gradient. To ensure that little or no pressure gradient is present in the simulations, the acceleration parameter:

$$K = \frac{\nu}{U_e^2}\frac{dU_e}{dx}, \tag{3.2}$$

is computed. Probing along the entire length of the domain, the acceleration parameter was found to be less than 3×10^{-8}. This is below the threshold where the mean flow becomes affected by a pressure gradient [44, 35] and supports the assumption that the pressure gradient is negligible in the present simulations.

3.5.2 Direct Numerical Simulation - $Re_\theta = 1500$

The primary source of error in the simulation presented above is thought to come from the use of the implicit LES technique. To gain greater confidence in this conclusion a DNS simulation was performed at the same Reynolds number. The primary difference between the implicit LES and DNS simulations was increased spatial resolution in the offwall direction and increased temporal resolution by a factor of eight. The DNS was warm started from the implicit LES simulation discussed above to minimize the computational cost.

Figure 3.9 compares the mean streamwise velocity profiles of the present implicit LES and DNS simulations. Agreement with the log law is improved slightly with the DNS simulation, approaching the expected log law with constant $C = 5.5$. A more significant improvement is observed in the fluctuating velocity pro-

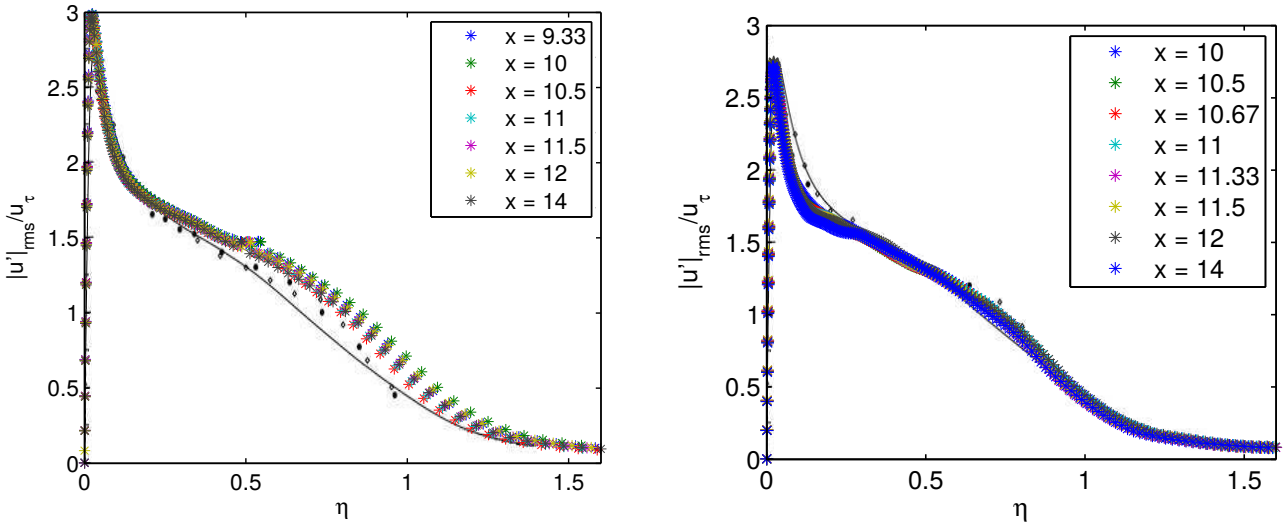

Figure 3.10: **DNS -** $Re_\theta = 1500$**:** Streamwise velocity fluctuation profiles from the implicit LES [left] and DNS [right] superimposed on the DNS results from Wu and Moin [49] at $Re_\theta = 900$ (thin line), the experimental results of Purtell et al. [37] at $Re_\theta = 1340$ (closed symbols), and the experimental results of Erm and Joubert [12] at $Re_\theta \approx 697$ (open symbols).

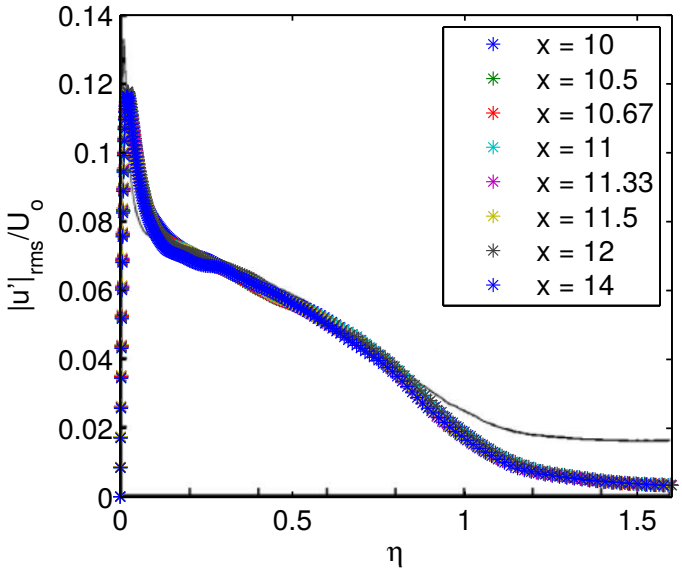

Figure 3.11: **DNS -** $Re_\theta = 1500$**:** Streamwise velocity fluctuation profiles of the DNS simulations superimposed on the present experimental data at $Re_\theta = 3800$ (thin line).

file shown in Figure 3.10. The DNS simulation is able to capture the magnitude of the peak flucturations and the behaviour through the logarithmic region much better than the implicit LES simulation. The fact that the peak is narrower than the reference experimental and computational data is consistent with the higher Reynolds number used in the present simulations. Figure 3.11 shows the same comparison with present experimental data at $Re_\theta = 3800$. In this case, the peak fluctuations in the experimental data occur even closer to the surface of the flat plate[1].

[1]The deviation outside the boundary layer is due to the noise floor of the PIV measurements.

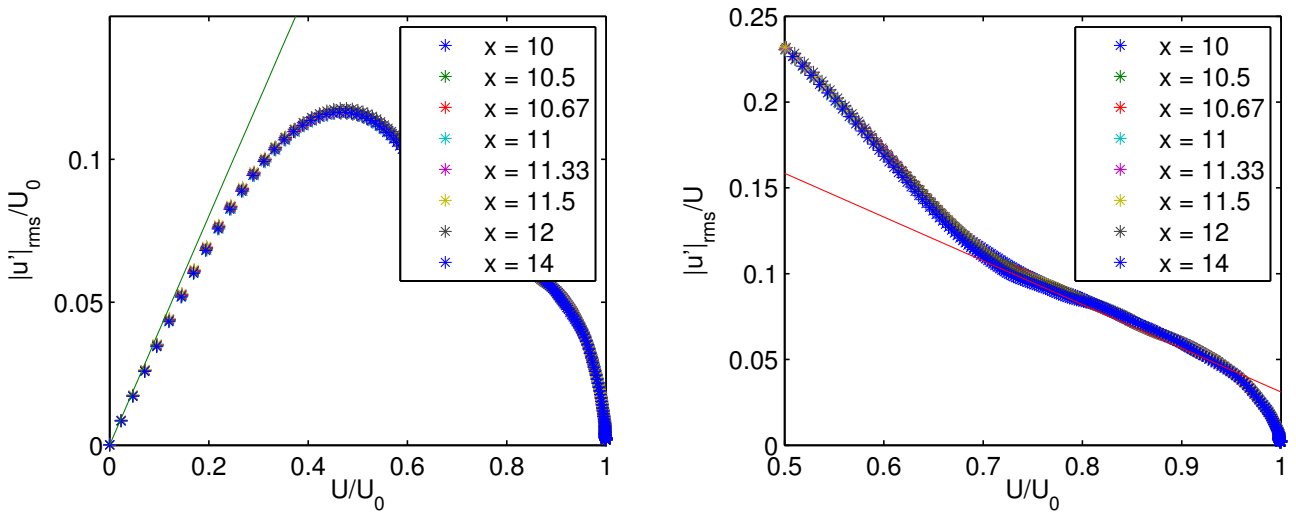

Figure 3.12: **DNS -** $Re_\theta = 1500$**:** Streamwise velocity fluctuation profiles with linear fits from Alfredsson et al. [2] [top], and Alfredsson et al. [1] [bottom].

We also recreated the diagnostic plots for the DNS simulation. These are shown in Figure 3.12. Once again, excellent agreement is found in the inner region of the boundary layer, and a slight improvement is observed in the outer part of the boundary layer with the DNS simulation.

The results presented in this section give us confidence that we are able to recreate the desired boundary layer to within the expected accuracy of the implicit LES technique. We conclude that there are no major sources of error in our simulations, and that if need be we can use DNS to get more accurate results. We also observe from the previous two sections, that while the implicit LES technique introduces some error into the velocity profiles, the relationship between the mean and fluctuating velocities throughout the boundary layer is well captured.

3.5.3 $Re_\theta = 3230$

The controlled experiments used to generate the parameter maps of change in skin friction were performed at a Reynolds number of $Re_\theta = 3230$. Hence we set the target Reynolds number for this uncontrolled implicit LES simulation to $Re_\theta = 3230$. After the flow transitioned to a stable fully-developed turbulent boundary layer, a fourth-order time-marching method was used with a time step of $\frac{\Delta t U_0}{\delta_\circ} = 0.01$. The value of Re_θ realized at the beginning of the working region is just over 3943, somewhat higher than the target value set at $Re_\theta = 3230$. The Re_τ value at the same location is about 1080, very close to the target of 1070.

Figures 3.13 and 3.14 show the mean velocity profile obtained from the present implicit LES simulation. As expected from the previous discussion, the present simulations overpredict the velocity, beginning in the buffer layer. Note the different axes used in Figure 3.14 to match the experimental data available. If

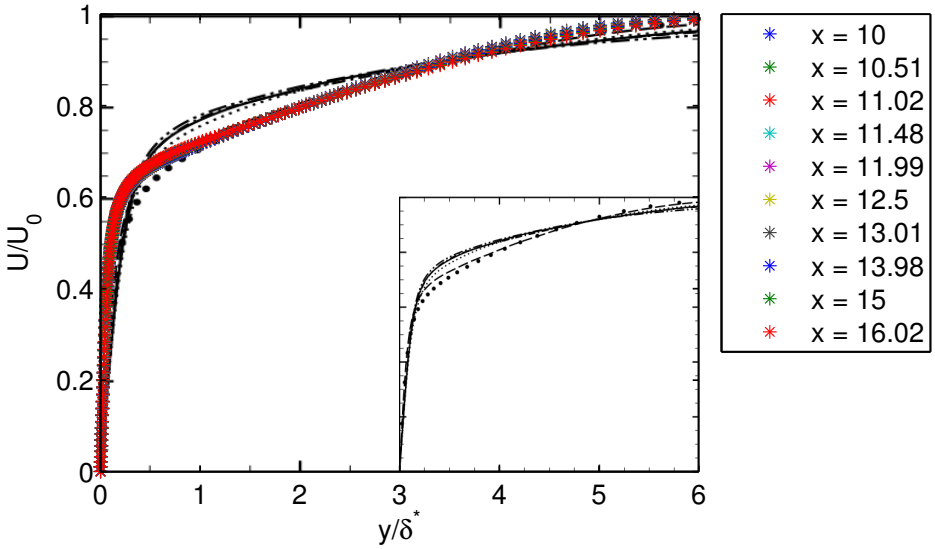

Figure 3.13: **Implicit LES -** $Re_\theta = 3230$**:** Streamwise velocity profile superimposed on the DNS of Sayadi et al.[41] at $Re_\theta = 1210$ (circles), as well as the LES of Sayadi and Moin [42] using: dynamic scale-similarity model ($- \cdot -$), dynamic Smagorinsky (–), dynamic one equation kinetic energy model ($- \cdot\cdot -$), global coefficient Vreman model ($\cdots$), and dynamic Smagorinsky with a fine grid ($-\ -\ -$). The prent results lie right on top of Sayadi and Moin's dynamic Smagorinsky results with a fine grid.

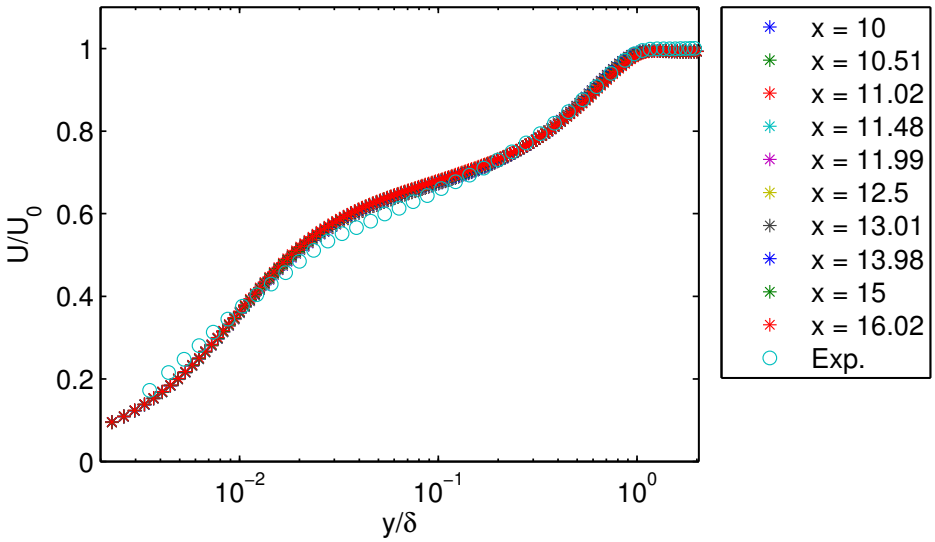

Figure 3.14: **Implicit LES -** $Re_\theta = 3230$**:** Streamwise velocity profile superimposed on the present experimental data at $Re_\theta = 4210$ (open circles).

we had plotted using u^+ and y^+, we would see that there is a deviation in mean velocity that continues through the logarithmic layer as before. The peak fluctuating velocity is likewise overpredicted, as shown in Figure 3.15. However, in contrast to the results at the lower Reynolds number, the fluctuating velocity is underpredicted to the right of the peak. This is reflected in the diagnostic plots shown in Figure 3.16. In the outer region, the numerical computations first dip below the curve before recovering the expected trend. A slight dip has been observed in other experimental and numerical data sets [2], but not to this

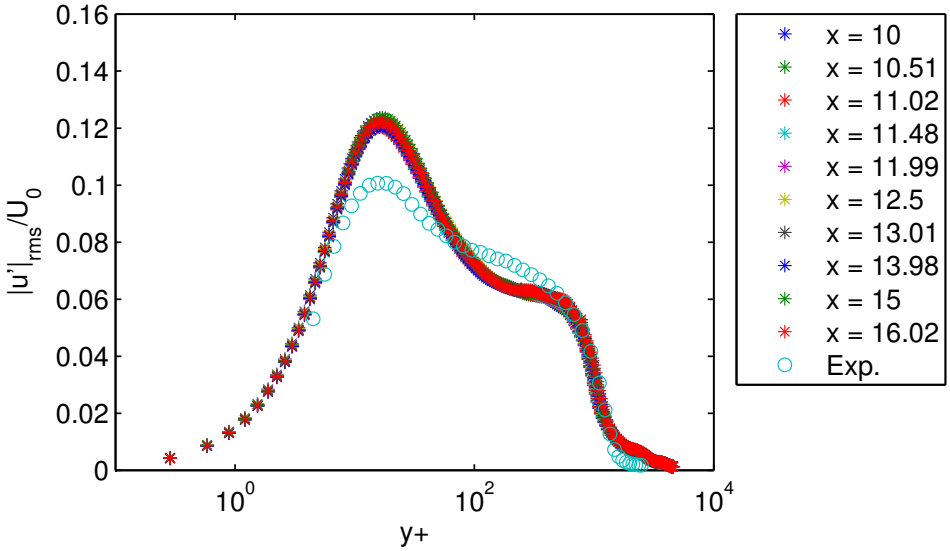

Figure 3.15: **Implicit LES -** $Re_\theta = 3230$**:** Streamwise fluctuating velocity profile superimposed on the present experimental data at $Re_\theta = 4210$ (open circles).

extent. The inner region matches well with the expected linear fit, as before.

In the controlled simulations presented below, the momentum thickness Reynolds number comes much more in line with the target value of 3230 both upstream and downstream of the jets. For example, with a Strouhal number of 0.0425 and blowing ratio of 0.3, the momentum thickness Reynolds number at $x = 9/\delta_\circ$ is about 3100. Likewise the agreement with the theoretical slope in the diagnostic plots is greatly improved in the controlled simulations as shown in Figure 3.17. We expect that the uncontrolled simulation would improve to a similar degree with a longer simulation time.

3.5.4 $Re_\theta = 4210$

To improve scale separation, some experimental data were obtained at a higher Reynolds number, $Re_\theta = 4210$. Here we present the implicit LES simulation used to match these experimental conditions. In this case, we used a second-order time-marching method with a time step of $\frac{\Delta t U_0}{\delta_\circ} = 0.2$. The value of Re_θ realized at the beginning of the working region is just over 3943, slightly lower than the target value set at $Re_\theta = 4210$. The Re_τ value at the same location is just under 1400.

Figure 3.18 shows the mean velocity profile superimposed on the experimental data. Significant over-prediction is observed beginning in the buffer layer and continuing throughout the logarithmic region. Large over prediction is also observed in the peak fluctuating velocity profile shown in Figure 3.19. Like with the $Re_\theta = 3230$ case, the fluctuating velocity is underpredicted to the right of the peak. Interestingly, despite the large deviations in both mean and fluctuating velocities, the diagnostic plots shown in Figure 3.20 look reasonably accurate.

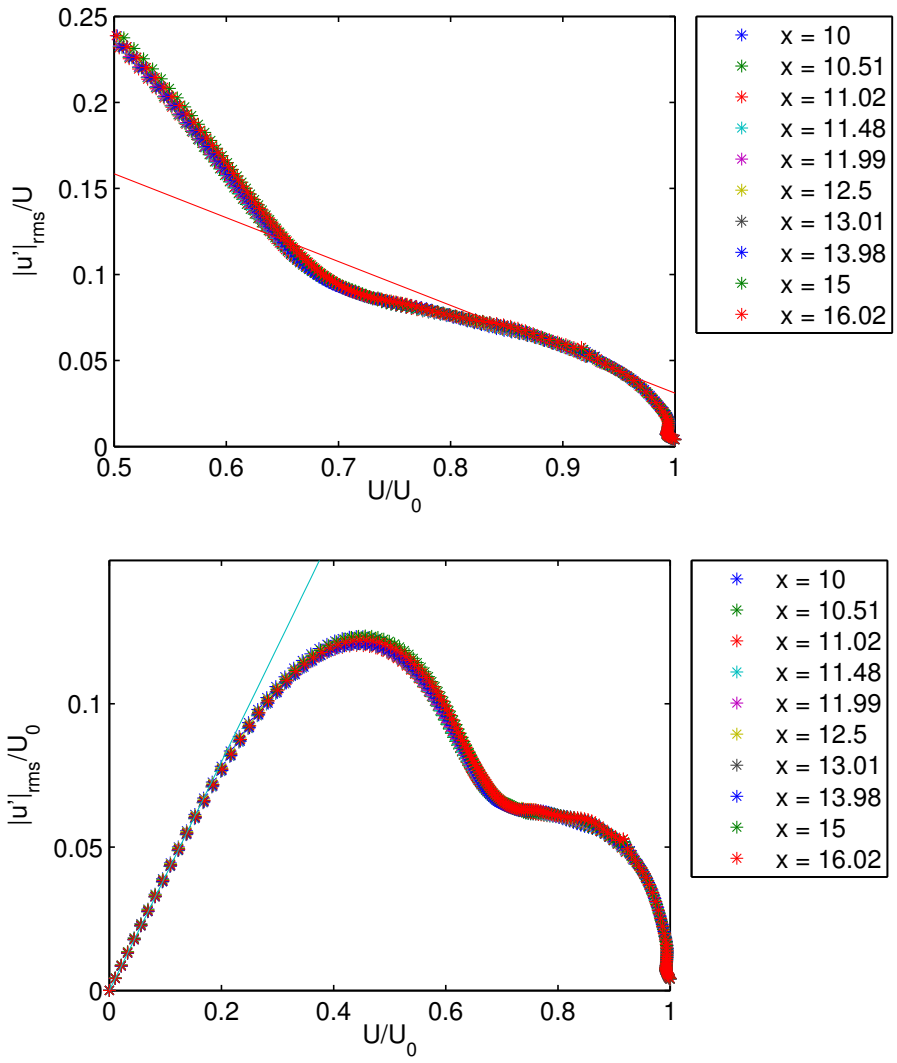

Figure 3.16: **Implicit LES -** $Re_\theta = 3230$**:** Streamwise velocity fluctuation profiles with linear fits from Alfredsson et al. [2] [top], and Alfredsson et al. [1] [bottom].

3.6 Controlled Simulations using Zero-Net-Mass-Flux Synthetic Jets

The controlled simulations are the primary interest of this work. The goal is provide additional information regarding the impact of actuation on skin friction drag for a limited number of parameters identified in the experimental campaigns. The majority of the parameters are taken from the skin friction parameter map for the 26mm spacing (See Figure 2.24). One is selected the original series of experiments presented in Section 2.3.2, and one which investigates scale separation between frequencies in the near wall peak and the forcing presented in Section 2.5. These simulations are carried out using the implicit LES technique. While the simulation parameters are selected to match the experiments, in practice there are some differences. For example, the simulations did not achieve the exact target Reynolds numbers or boundary-layer thicknesses at the beginning of the working region. Furthermore, slight variations in the location of the sensor can have a significant impact on the results as discussed further below.

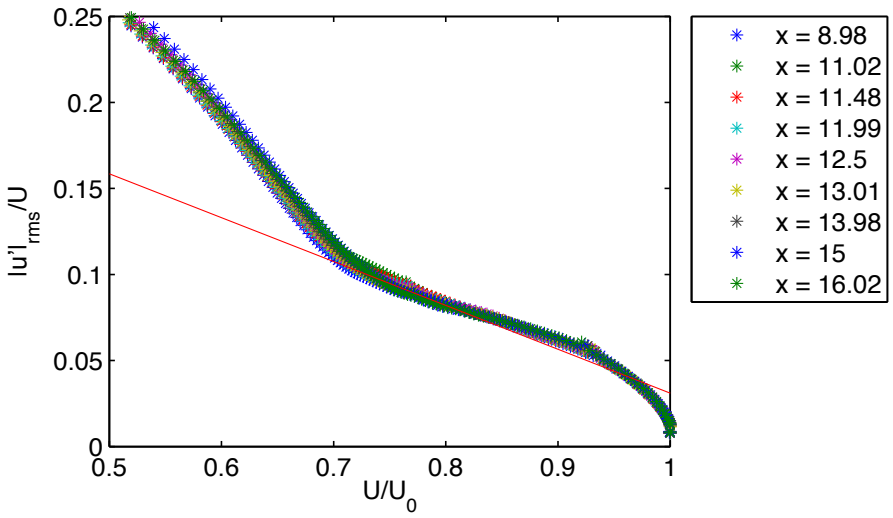

Figure 3.17: **Implicit LES -** $Re_\theta = 3230$**, St=0.0425, r=0.3:** Streamwise velocity fluctuation profile with linear fit from Alfredsson et al. [2].

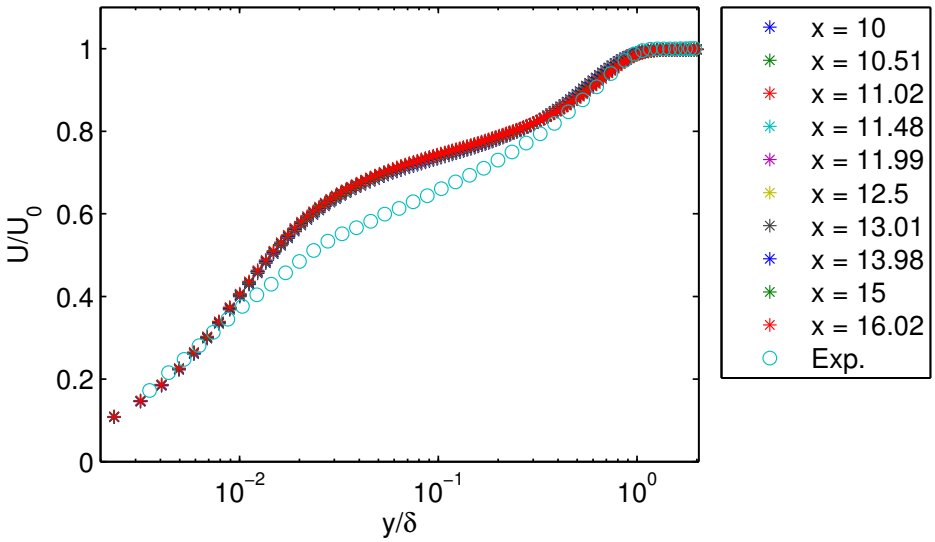

Figure 3.18: **Implicit LES -** $Re_\theta = 4210$**:** Streamwise velocity profile superimposed on the present experimental data at $Re_\theta = 4210$ (open circles).

In the controlled simulations, the jets are oriented in the spanwise direction with aspect ratio 13:1 and width $0.3\delta_\circ$. The jets are centered in the domain at $x = 10\delta_\circ$, and $z = 1.5\delta_\circ$ for one jet, or $z = 1.2\delta_\circ$ and $z = 1.8\delta_\circ$ for two jets. The initial flow solutions for the controlled simulations are linearly interpolated from the uncontrolled simulations. Note that the grids only differ in the region around the jet. The initial flow inside the jets is quiescent. A few jet cycles are allowed to pass at the beginning of the controlled simulations before averaging begins. This is done to eliminate any transients from the interpolation or the start of the actuation. The forcing at the base of the slot is sinusoidal $U = A\sin(\bar{f}\,\bar{t})$, where A is the maximum jet velocity computed from the blowing ratio r, the frequency $\bar{f} = 2\pi St$ is computed from the

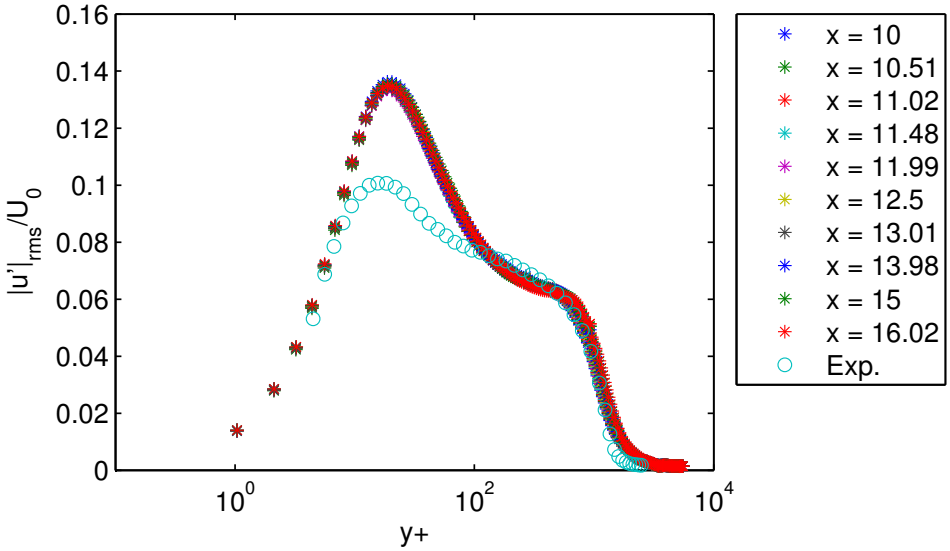

Figure 3.19: **Implicit LES -** $Re_\theta = 4210$**:** Streamwise fluctuating velocity profile superimposed on the present experimental data at $Re_\theta = 4210$ (open circles).

Strouhal number St, and the nondimensional time is $\bar{t} = \frac{tU_0}{\delta_\circ}$. As with the uncontrolled simulations, the Mach number in all of the controlled simulations is 0.2.

Figure 3.21 compares the integration regions considered in the numerical simulations, along with the quadrature points used in the experiments (See Section 2.4). The first integration region used in the computations matches the extreme values of the experimental quadrature points. The second region spans $\{x \times z\} = \{[5, 15] \times [0, 3]\}\delta_\circ$, excluding the spanwise strip where the jets are located $x = [9.99, 10.01]\delta_\circ$.

3.6.1 Effect of rectification in the experimental data

The experimental data presented in the following sections is all from locally rectified measurements (no derectification has been applied). In contrast, the numerical data presented is directional, unless specified otherwise. This difference has the most significant impact in areas of recirculation, which have been observed just behind the jet. This could also influence areas where the wall shear stress approaches zero.

Figure 3.22 compares the change in phase-averaged skin friction coefficient computed from rectified friction velocity and directional wall shear stress measurements. Both data sets are taken from the computations, but are used to illustrate the error incurred by the experimental measurement technique. The data is presented for Strouhal number 0.0425 and blowing ratios r=0.1, 0.2, and 0.3. As expected, the primary difference is observed just downstream of the jet where an area of recirculation forms during the blowing phase of the jets. The impact of the rectification increases with blowing ratio.

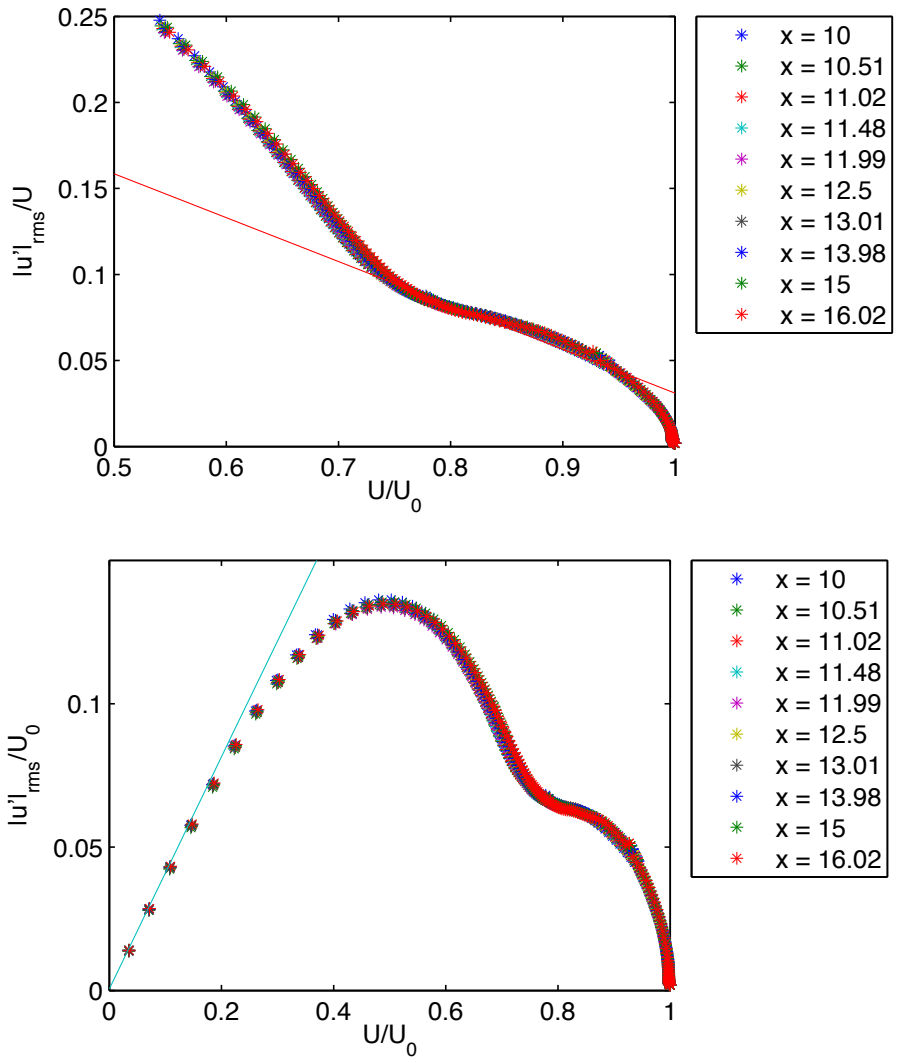

Figure 3.20: **Implicit LES -** $Re_\theta = 4210$**:** Streamwise velocity fluctuation profiles with linear fits from Alfredsson et al. [2] [left], and Alfredsson et al. [1] [right].

3.6.2 Two jets, $Re_\theta = 3230$, $St = 0.010625$, $r = 0.15$

A Strouhal number of 0.010625 and blowing ratio of 0.15 are parameters identified in the experimental campaign presented in Section 2.4.3 as potentially leading to skin friction drag reduction. The skin friction drag reduction computed from the experimental measurements is on the order of $-0.5 \pm 0.3\%$.

Comparison with experiment

Figure 3.23 shows the change in time-averaged skin friction coefficient along the jet centerlines and in between the jets, overlaid with the experimental measurements. The jet centerline plot shows a large increase in skin friction near the jet. This region of high skin friction decreases very rapidly away from the jet into small regions of skin friction reduction both upstream and downstream of the jet. The discrepancy between the experimental and computational results in this region may be due to the high gradients and

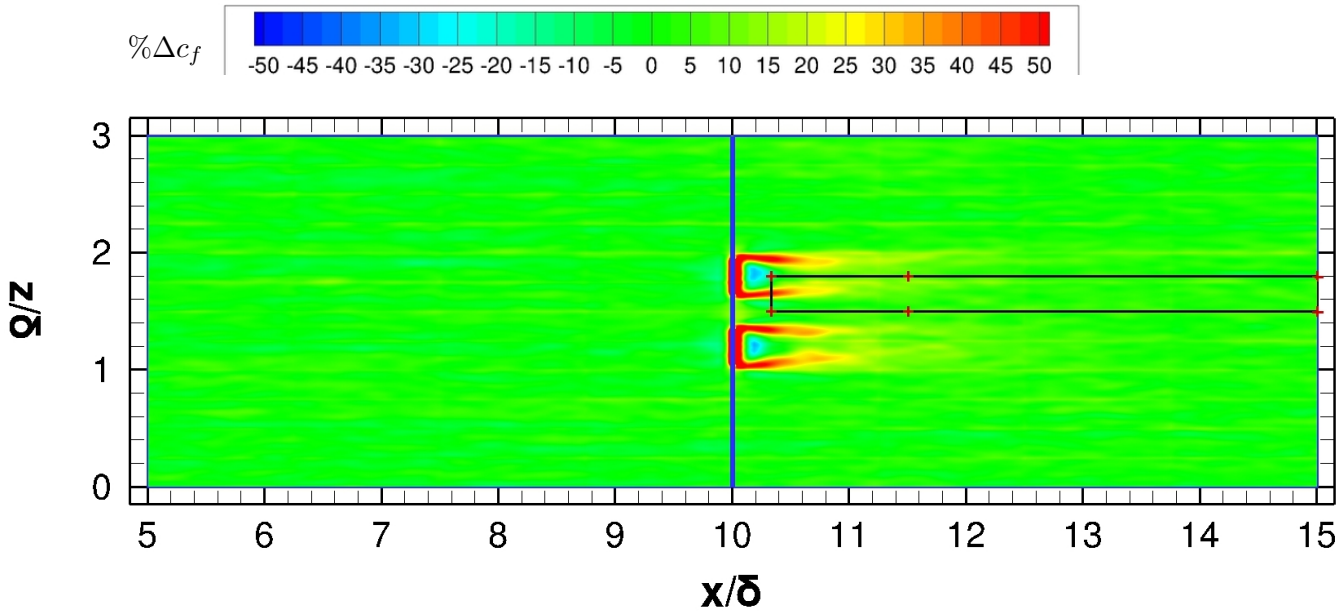

Figure 3.21: **Comparison with experiment:** Integration points for trapezoidal rule used in experiments $\{[10.33, 1.5], [10.33, 1.8], [11.5, 1.5], [11.5, 1.8], [15, 1.5], [15, 1.8]\}\delta_\circ$ (red); integration area for computations spanned by $\{x \times z\} = \{[10.33, 15] \times [1.5, 1.8]\}\delta_\circ$ (black); alternate integration area for computations spanned by $\{x \times z\} = \{[5, 15] \times [0, 3]\}\delta_\circ$, excluding the spanwise strip where the jets are located $x = [9.99, 10.01]\delta_\circ$ (blue).

the precise location of the sensor, or due to the rectification of the experimental measurements. Moving further downstream the computed skin friction rises again and then slowly decays back to zero.

At $1.5\delta_\circ$ downstream of the jet, the computations predict a slightly higher skin friction than the experiments. Figure 3.24 shows the spanwise variation at each of the downstream locations. The plot corresponding to $x = 11.5\delta_\circ$ shows that there may exist a small skin friction increase along the jet centerline; however, there is also a dip in the profile near the centerline. The limited number of cycles over which the numerical data is averaged could cause a variation in the location of this dip. The data could also be influenced by slight variations in the flow properties, for example the momentum thickness Reynolds number or boundary layer thickness, or the sensor placement in the experiments.

Along the streamwise line in between the two jets the skin friction increases slowly to just downstream of the jets, rises more rapidly, and then decays again. A similar overprediction is seen in the computational data at $x = 11.5\delta_\circ$. As with the centerline data, there is a dip in the profile just to the right of the measurement point in the computational data (Figure 3.24). This may explain the difference seen along the streamwise plots.

Mapping the change in skin friction

Figure 3.25 shows a spatial map of the change in time-averaged skin friction coefficient. As discussed above, there is a significant skin friction increase near the jet and a small pocket of skin friction reduction

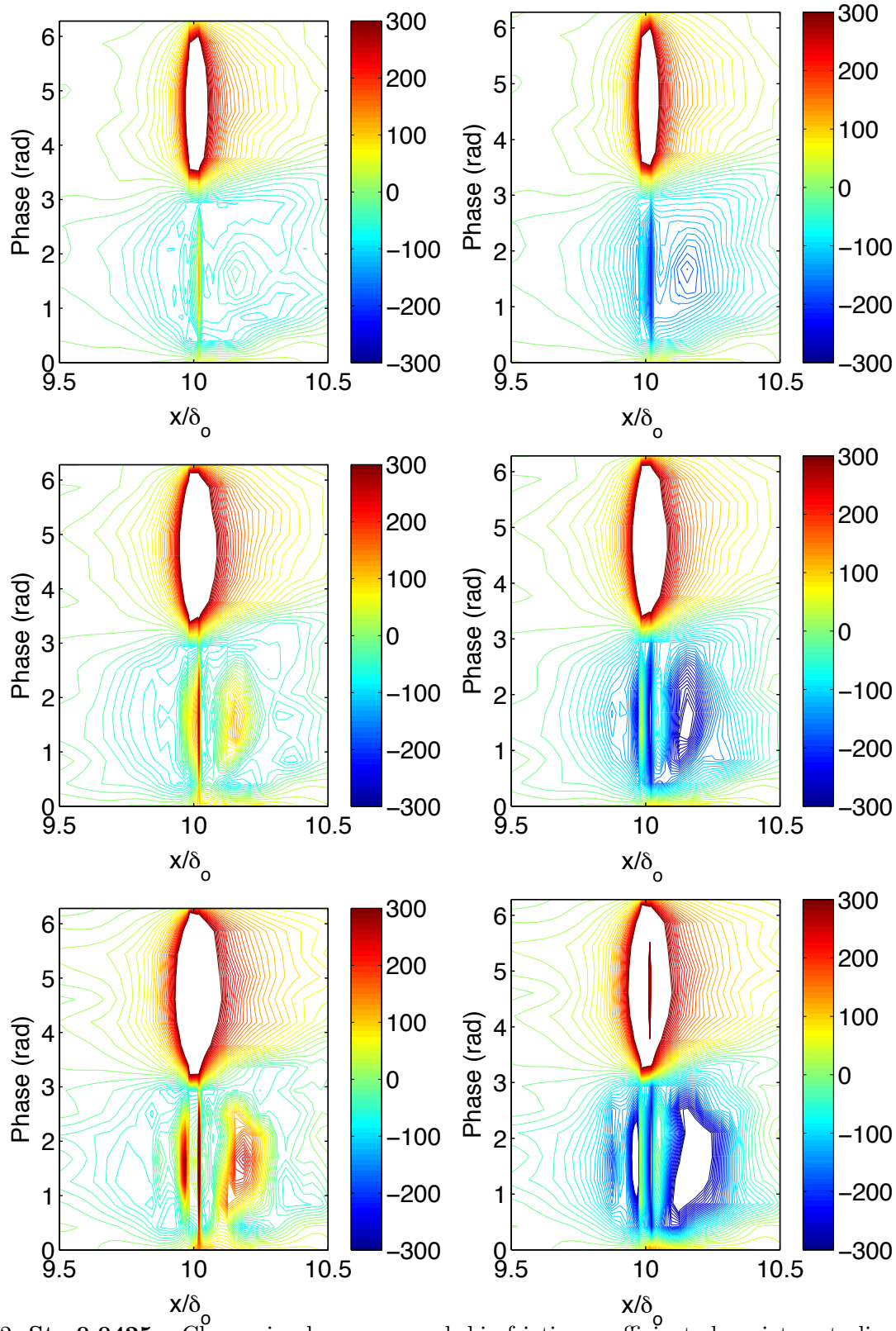

Figure 3.22: **St=0.0425:** Change in phase-averaged skin friction coefficient along jet centerline computed from rectified friction velocity [left] and computed from directional wall shear stress [right]. Blowing ratios are $r = 0.1$ [top], $r = 0.2$ [middle], and $r = 0.3$ [bottom].

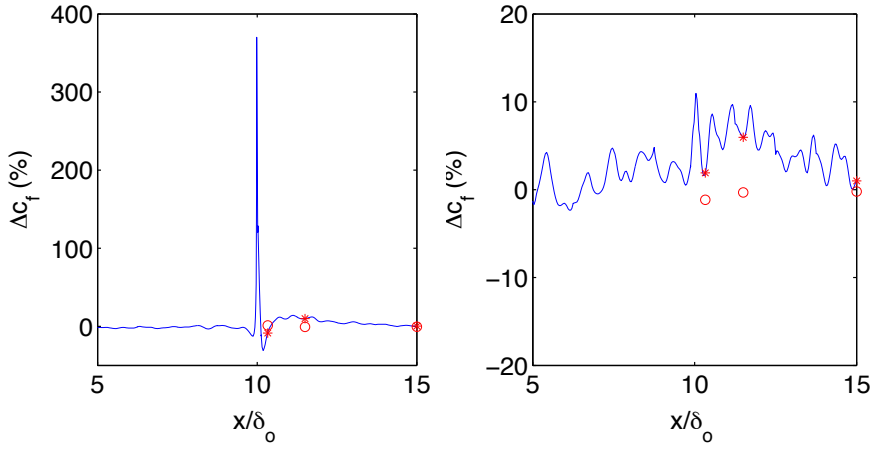

Figure 3.23: **St=0.010625, r=0.15:** Change in time-averaged skin friction coefficient along jet centerline [left] and along the streamwise line between the jets [right]. Open symbols are from the experimental data; asterisks are the same points from the computations.

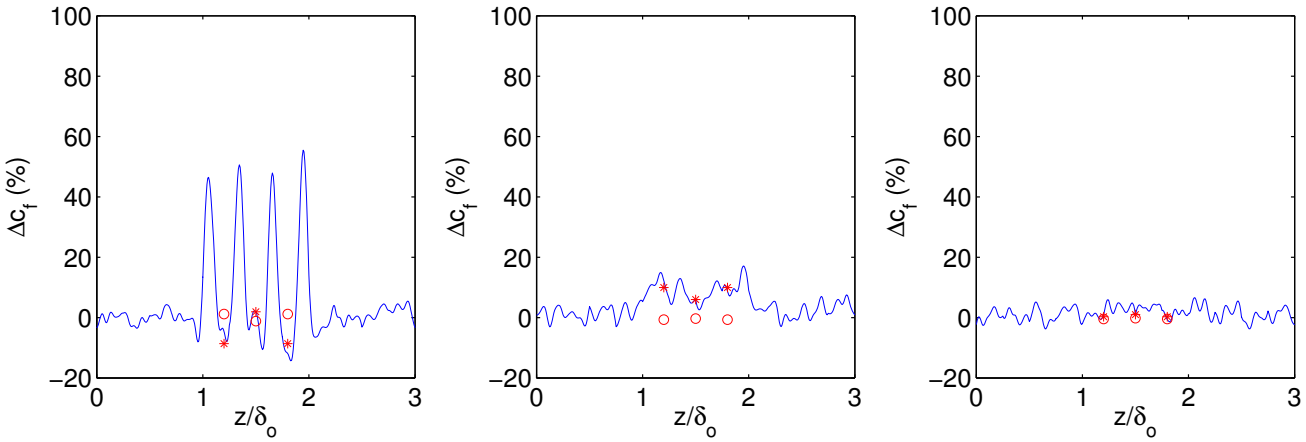

Figure 3.24: **St=0.010625, r=0.15:** Change in time-averaged skin friction coefficient along spanwise lines of $x = 10.33\delta_\circ$ [left], $x = 11.5\delta_\circ$ [center], and $x = 15\delta_\circ$ [right]. Open symbols are from the experimental data; asterisks are the same points from the simulations. The curves are also from the simulation data.

just behind the jet. The figure also shows two long strips of increased skin friction emanating from the edges of the jets. This can also be seen in the spanwise profiles shown above in Figure 3.24.

Using the computational data shown in this figure and integrating over the area spanned by $\{x \times z\} = \{[10.33, 15] \times [1.5, 1.8]\}\delta_\circ$, the area bounding the quadrature points used with the experimental data to create the parameter maps in Section 2.4.3, the change in skin friction coefficient is about 3%. The primary reason we obtain a drag increase, rather than the reduction seen in the experimental parameter map (Figure 2.24), is due to the large positive change in skin friction coefficient observed emanating from the edge of the jets. This is caused by the formation of streamwise vortices pulling high momentum fluid closer to the wall. Expanding the region of integration to $\{x \times z\} = \{[5, 15] \times [0, 3]\}\delta_\circ$, excluding the spanwise strip where the jets are located $x = [9.99, 10.01]\delta_\circ$, yields a drag increase of about 0.9%.

Additional information can be gleaned from the maps of change in phase-averaged skin friction coeffi-

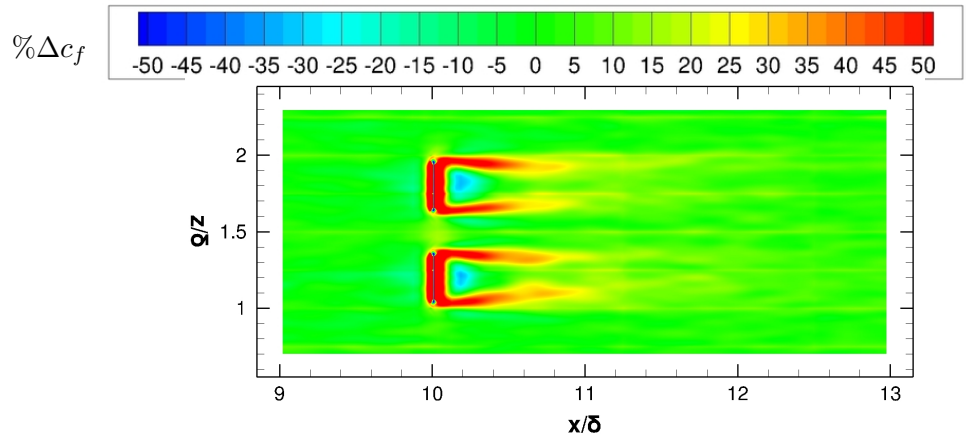

Figure 3.25: **St=0.010625, r=0.15:** Spatial map of change in time-averaged skin friction coefficient.

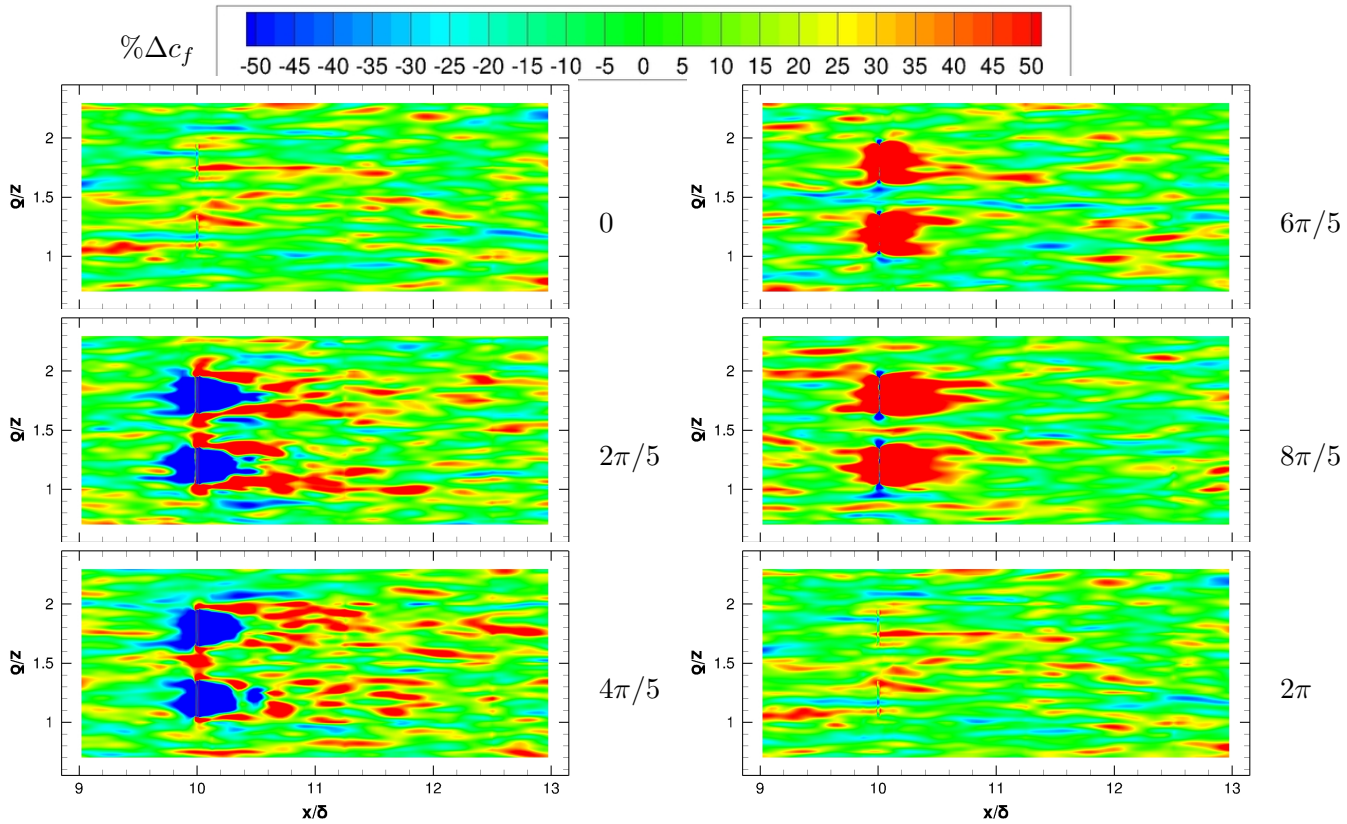

Figure 3.26: **St=0.010625, r=0.15:** Spatial maps of change in phase-averaged skin friction coefficient.

cient shown in Figure 3.26. During the first half of the cycle, the blowing phase, the flow is pushed away from the wall, causing a reduction in skin friction drag ahead of and behind the jet. This also causes a small region of recirculation to form behind the jets. The figure shows the formation of long strands of positive change in skin friction emanating from the edges of the jets during this phase. Some interaction right between the jets is also observed during the blowing phase. During the second half of the cycle, the suction phase, the flow is pulled towards the wall, creating an increase in skin friction ahead of and behind the jet.

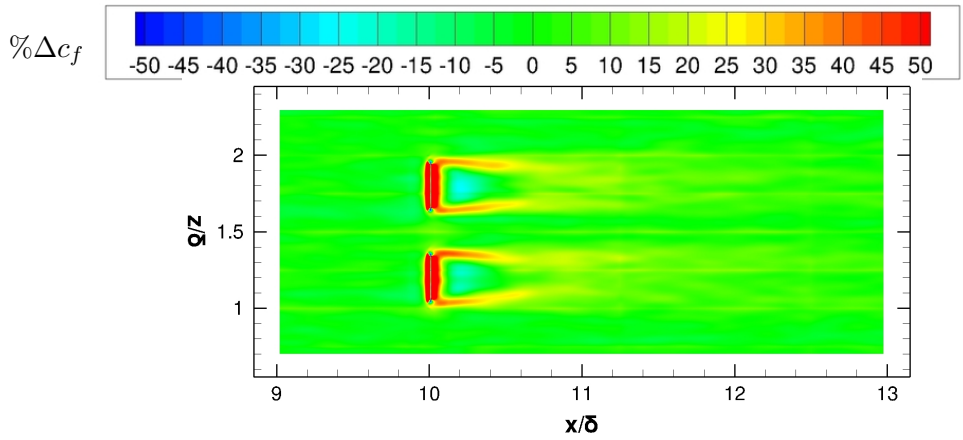

Figure 3.27: **St=0.0425, r=0.1:** Spatial map of change in time-averaged skin friction coefficient.

3.6.3 Two jets, $Re_\theta = 3230$, $St = 0.0425$, $r = 0.1$

A Strouhal number of 0.04625 and a blowing ratio of 0.1 are another set of parameters identified in the experimental campaign as potentially leading to skin friction drag reduction. The experimental campaign indicated a drag reduction on the order of $-0.9 \pm 0.3\%$.

Change in skin friction

Figure 3.27 shows a spatial map of change in time-averaged skin friction coefficient. The characteristics of the map are very similar to the Strouhal 0.010625 and blowing ratio 0.15 case, though slightly less pronounced. A large increase in drag is observed right around the jet, a small pocket of drag reduction is seen behind the jet, and two strands of increased drag emanate from sides of the jet. Integrating over the same region used with the experimental data to generate the parameter maps, the change in skin friction is about 2.9%. Using the larger integration area spanned by $\{x \times z\} = \{[5, 15] \times [0, 3]\}\delta_\circ$, excluding the spanwise strip where the jets are located $x = [9.99, 10.01]\delta_\circ$, the change in skin friction drag is roughly 1.2%. As before, the strands of positive change in skin friction emanating from the sides of the jets contribute the increase in skin friction computed. The measurement locations used in the experiments do not capture this feature.

Spatial maps of change in phase-averaged skin friction coefficient are shown in Figure 3.28. The characteristics of the maps are very similar to the Strouhal 0.010625 and blowing ratio 0.15 case. During the first half of the cycle, the blowing phase, the flow is pushed away from the wall causing a reduction in skin friction both ahead of and behind the jet. This also creates counter-rotating vortices emanating from the edges of the jets, bringing high momentum fluid close to the wall and increasing skin friction in this region. During the second half of the cycle, the suction phase, the flow is drawn toward the wall, yielding an overall increase of friction drag both upstream and downstream of the jets.

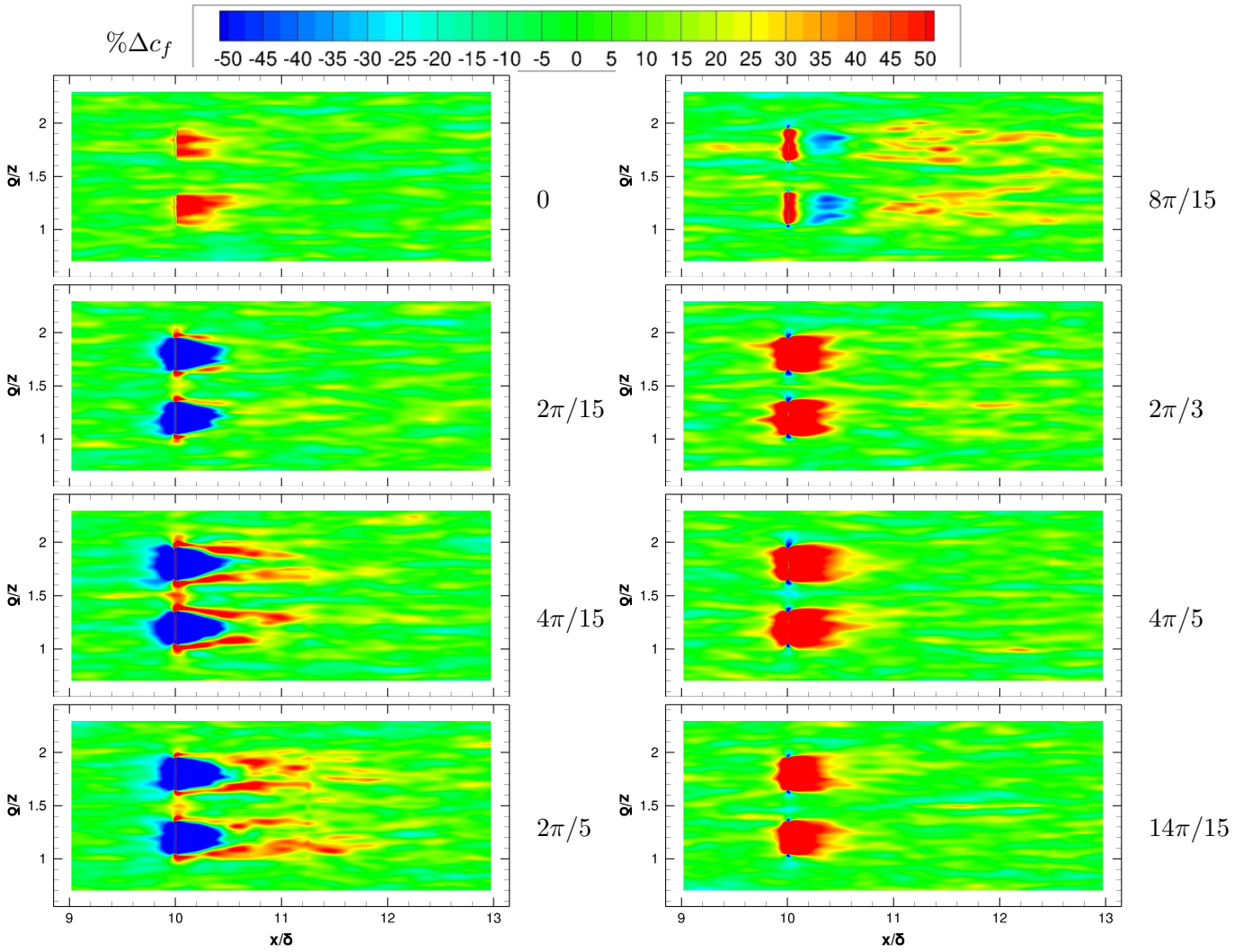

Figure 3.28: **St=0.0425, r=0.1:** Spatial maps of change in phase-averaged skin friction coefficient.

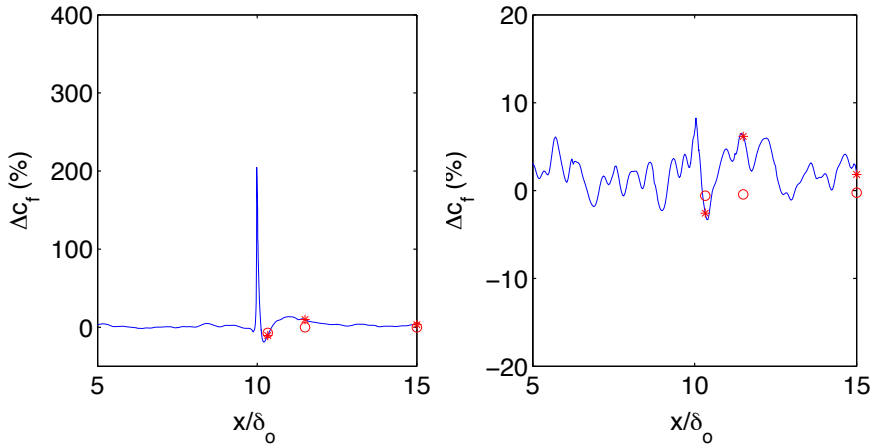

Figure 3.29: **St=0.0425, r=0.1:** Change in time-averaged skin friction coefficient along jet centerline [left] and along the streamwise line between the jets [right]. Open symbols are from the experimental data; asterisks are the same points from the computations.

Comparison with experiment

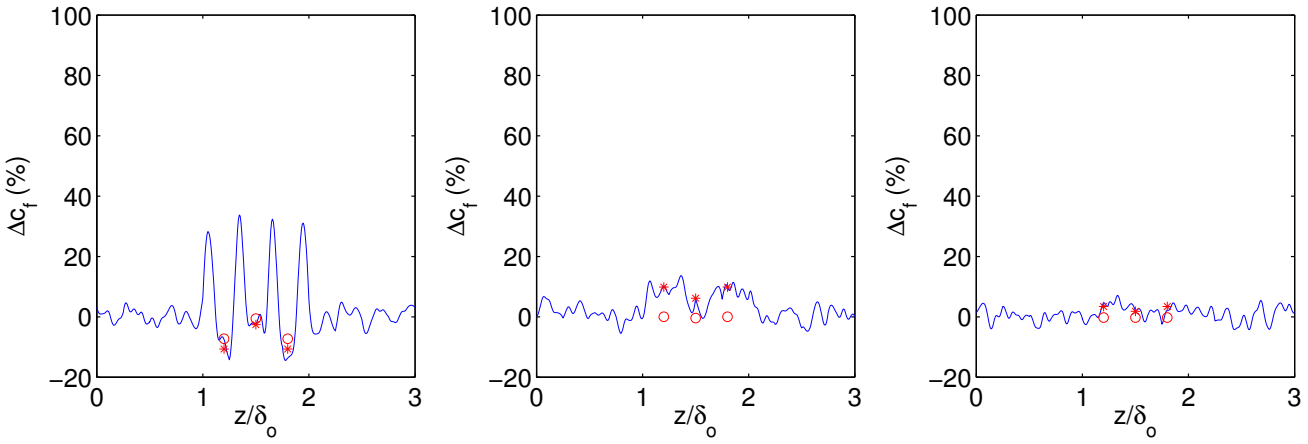

Figure 3.30: **St=0.0425, r=0.1:** Change in time-averaged skin friction coefficient along spanwise lines of $x = 10.33\delta_\circ$ [left], $x = 11.5\delta_\circ$ [center], and $x = 15\delta_\circ$ [right]. Open symbols are from the experimental data; asterisks are the same points from the simulations. The curves are also from simulation data.

Figures 3.29 and 3.30 show the change in time-averaged skin friction along streamwise and spanwise lines corresponding to the experimental measurement locations respectively. Good agreement with the experimental measurements is seen along the jet centerlines. The largest discrepancy between the experimental and computational results occurs $1.5\delta_\circ$ downstream of the jet. There is a noticeable drag increase shown in the computations, which is not present in the experimental results. Unlike the Strouhal number 0.010625 case, there are no dips in the curve to the right or left of the centerlines. Figure 3.27 shows the increased skin friction regions emanating from the edges of the jets merging along the jet centerline. Similar behaviour is observed in several cases discussed below. The experimental behaviour is recovered by $5\delta_\circ$ downstream of the jet.

3.6.4 Two jets, $Re_\theta = 3230$, $St = 0.0425$, $r = 0.2$

This case has the same Strouhal number 0.0425 as the previous case, but the blowing ratio is increased from 0.1 to 0.2. This is another set of parameters identified in the experimental campaign as potentially leading to skin friction drag reduction. The experiments found a drag reduction of $-1 \pm 0.3\%$.

Change in skin friction

Figure 3.31 shows a spatial map of the change in time-averaged skin friction coefficient. The features using the higher blowing ratio of 0.2 are much stronger than with the blowing ratio 0.1, though they have similar characteristics. This is also reflected in the maps of change in phase-averaged skin friction coefficient shown in Figure 3.32. Integrating over the area used with the experiments to generate the parameter maps, the skin friction drag increases by about 3.2%. While the region of reduced skin friction drag downstream of the jet grows, so does the strength of the drag increase in other regions. Thus a slightly higher increase in

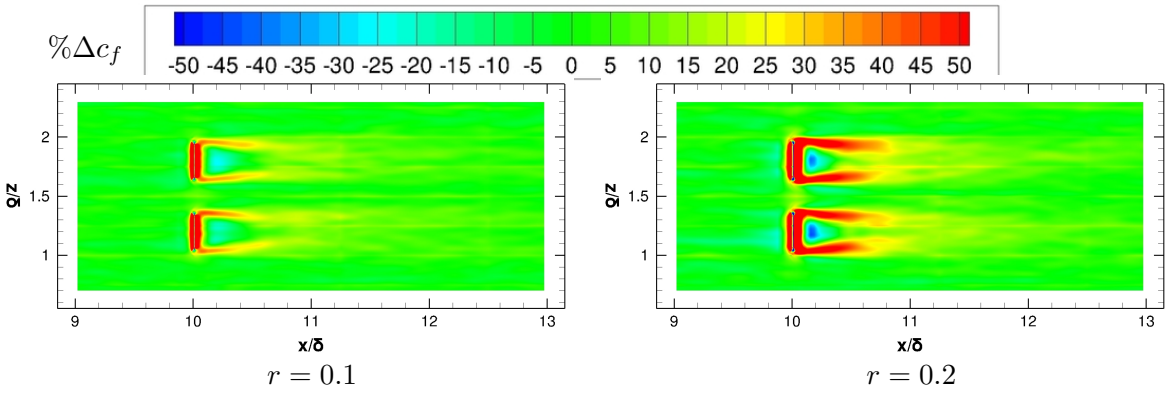

Figure 3.31: **St=0.0425, r=0.2:** Spatial map of change in time-averaged skin friction coefficient.

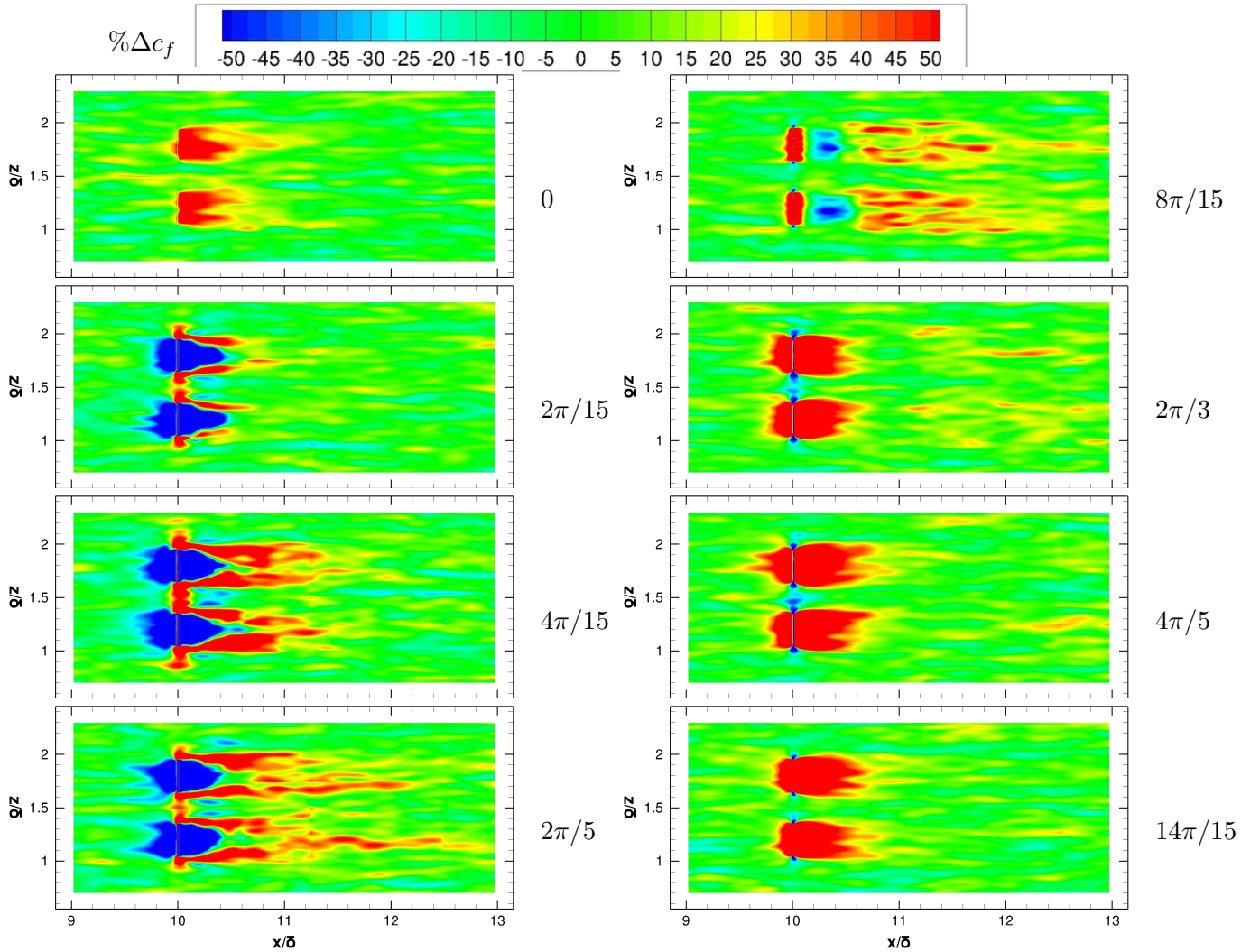

Figure 3.32: **St=0.0425, r=0.2:** Spatial maps of change in phase-averaged skin friction coefficient.

skin friction is computed in this region. Using the larger integration area, the skin friction drag increases by about 2%, noticeably higher than the previous case.

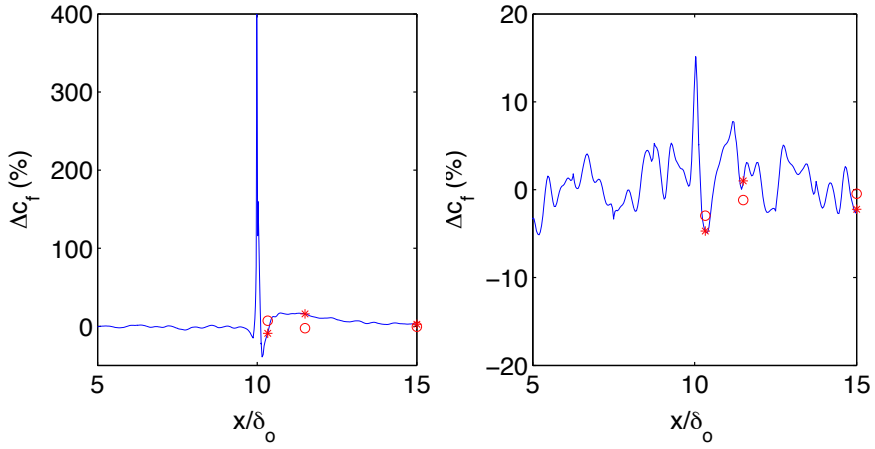

Figure 3.33: **St=0.0425, r=0.2:** Change in time-averaged skin friction coefficient along jet centerline [left] and along the streamwise line between the jets [right]. Open symbols are from the experimental data; asterisks are the same points from the computations.

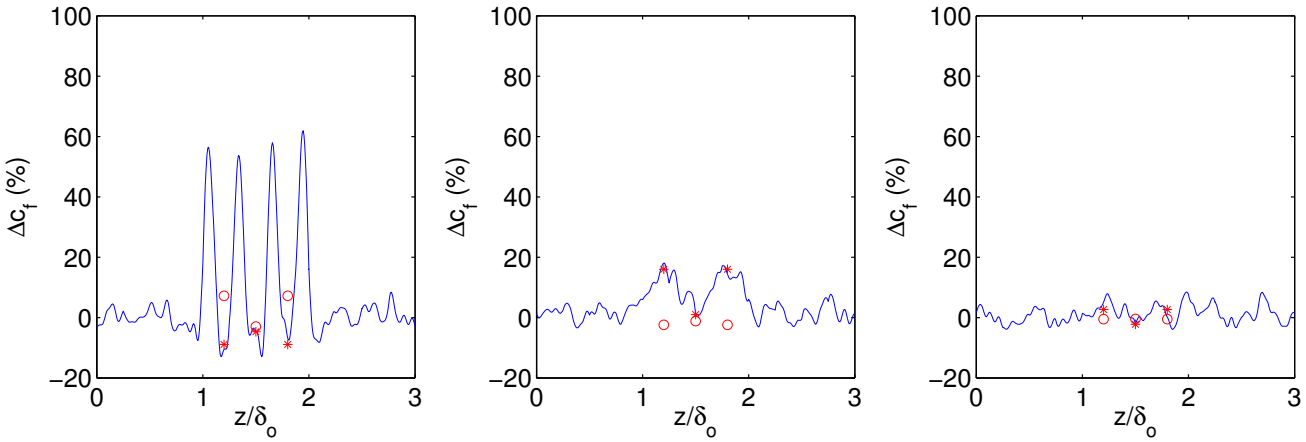

Figure 3.34: **St=0.0425, r=0.2:** Change in time-averaged skin friction coefficient along spanwise lines of $x = 10.33\delta_\circ$ [top left], $x = 11.5\delta_\circ$ [top right], and $x = 15\delta_\circ$ [bottom]. Open symbols are from the experimental data; asterisks are the same points from the simulations. The curves are also from simulation data.

Comparison with experiment

Figures 3.33 and 3.34 show the change in time-averaged skin friction coefficient along the streamwise and spanwise lines corresponding to the experimental measurement locations. The effect of rectification in the experimental measurements is clearly seen at the $x = 10.33\delta_\circ$ location, where the computational data predicts a significantly lower skin friction. The largest discrepancy between the experimental and computational results occurs along the jet centerline $1.5\delta_\circ$ downstream of the jet. This is similar to the previous case. The behaviour seen in the experiment is again recovered $5\delta_\circ$ downstream of the jet. Good agreement is observed between the computations and experiment along the streamwise line separating the jets.

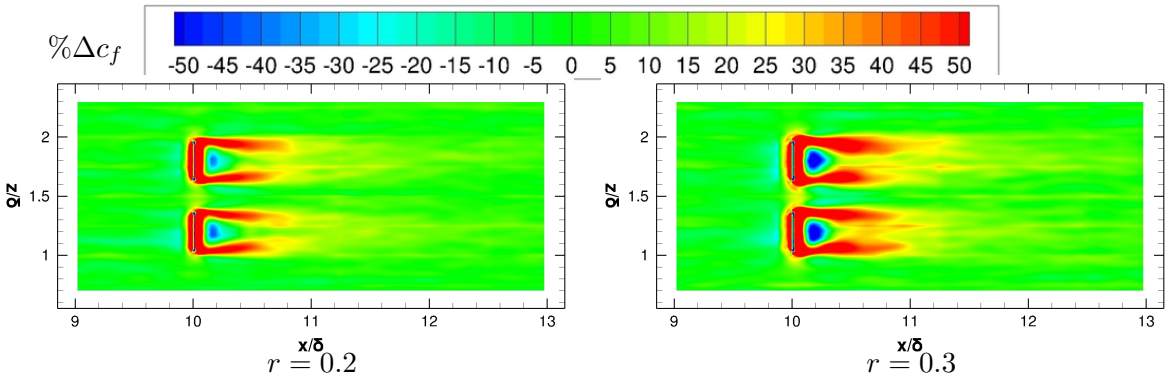

Figure 3.35: **St=0.0425, r=0.3:** Spatial map of change in time-averaged skin friction coefficient.

3.6.5 Two jets, $Re_\theta = 3230$, $St = 0.0425$, $r = 0.3$

Consider again the Strouhal number of 0.0425 with an increased blowing ratio of 0.3. This is another set of parameters identified in the experimental campaign as potentially leading to skin friction drag reduction. The experimental measurements give a drag reduction on the order of $-0.8 \pm 0.3\%$.

Change in skin friction

Figures 3.31 and 3.35 compare the maps of change in time-averaged skin friction coefficient for Strouhal 0.0425 between the blowing ratios 0.1 and 0.2, and 0.2 and 0.3, respectively. The features in these maps are very similar and increase in prominence with blowing ratio. This is also reflected in the phase-averaged maps shown in Figures 3.28, 3.32, and 3.36. At the highest blowing ratio of 0.3, the two jets begin to interact with each other in the time-averaged data, though similar interaction is visible in the phase-averaged data even at the lowest blowing ratio of 0.1. Integrating the spatial map of change in time-averaged skin friction with blowing ratio 0.3 over the same region used with the experiments to generate the parameter map yields an increase in skin friction drag of about 3.7%. Given the increasing strength of features producing a positive change in skin friction drag, it is not surprising that the highest blowing ratio also produces the greatest increase in drag. If we consider the larger region of integration spanning $\{x \times z\} = \{[5, 15] \times [0, 3]\}\delta_\circ$, excluding the spanwise strip where the jets are located $x = [9.99, 10.01]\delta_\circ$, the drag increases by about 2.5%.

Comparison with experiment

Figures 3.37 and 3.38 compare the change in time-averaged skin friction coefficient along the streamwise and spanwise lines corresponding to the experimental measurement locations. Similar features are present as with the lower blowing ratio cases. The effect of rectification in the experimental data near the jets and along their centerlines is most evident at this highest blowing ratio. The experimental measurements

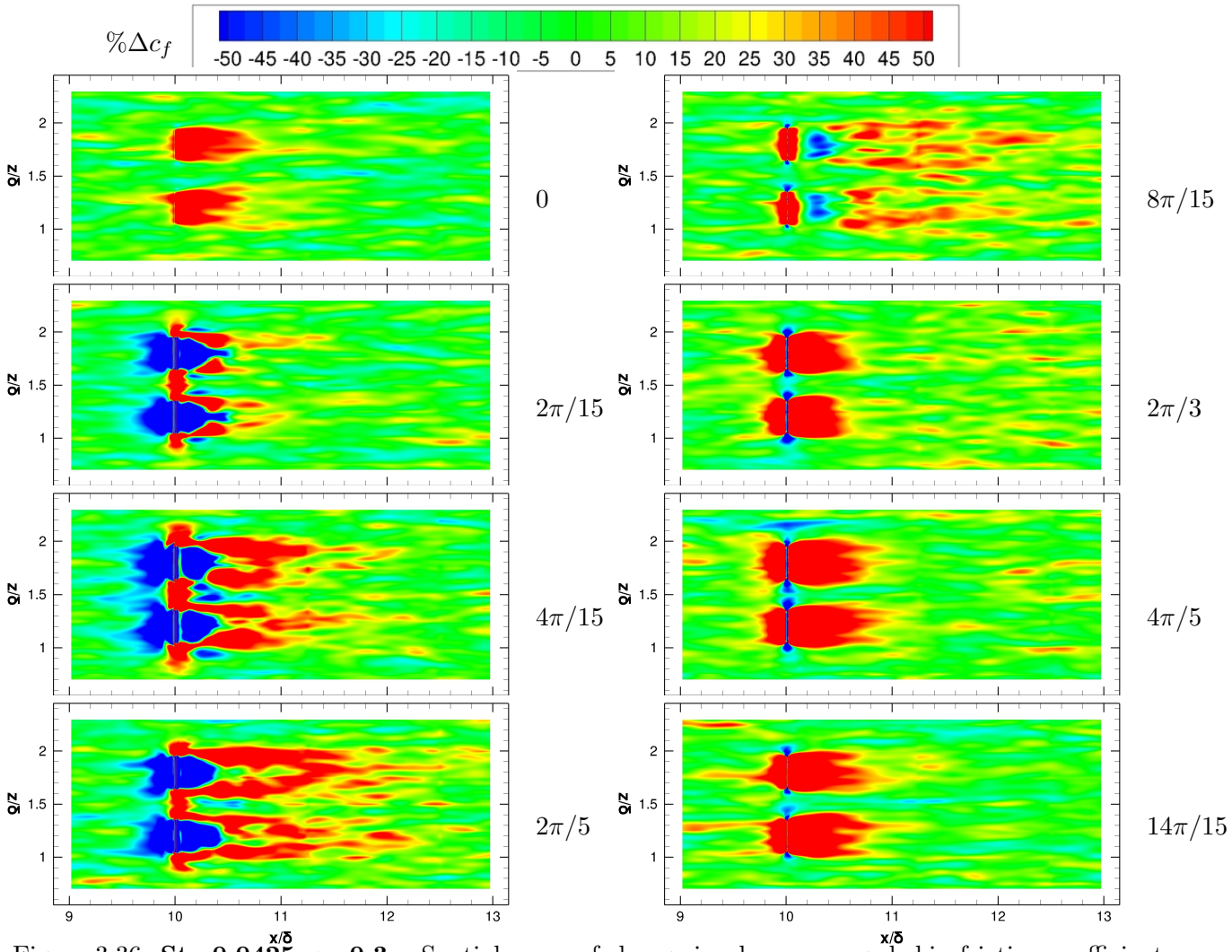

Figure 3.36: **St=0.0425, r=0.3:** Spatial maps of change in phase-averaged skin friction coefficient.

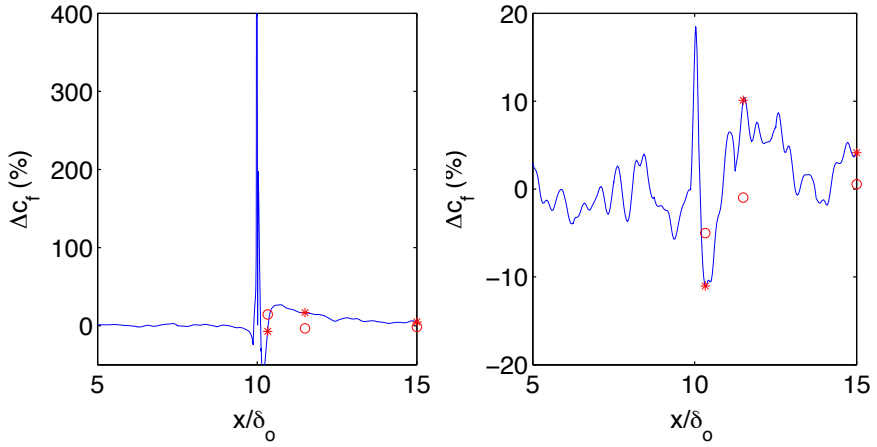

Figure 3.37: **St=0.0425, r=0.3:** Change in time-averaged skin friction coefficient along jet centerline [left] and along the streamwise line between the jets [right]. Open symbols are from the experimental data; asterisks are the same points from the computations.

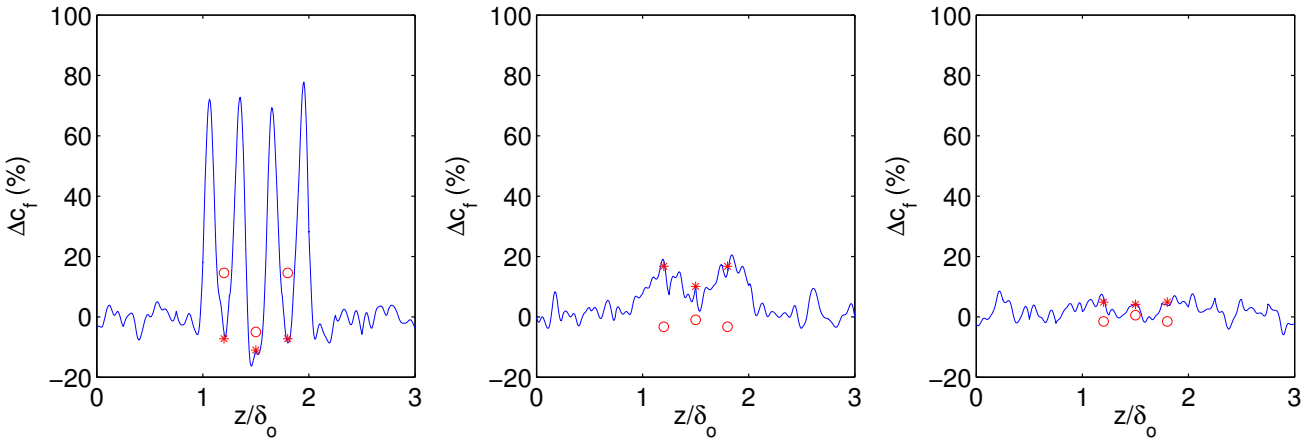

Figure 3.38: **St=0.0425, r=0.3:** Change in time-averaged skin friction coefficient along spanwise lines of $x = 10.33\delta_\circ$ [top left], $x = 11.5\delta_\circ$ [top right], and $x = 15\delta_\circ$ [bottom]. Open symbols are from the experimental data; asterisks are the same points from the simulations. The curves are also from simulation data.

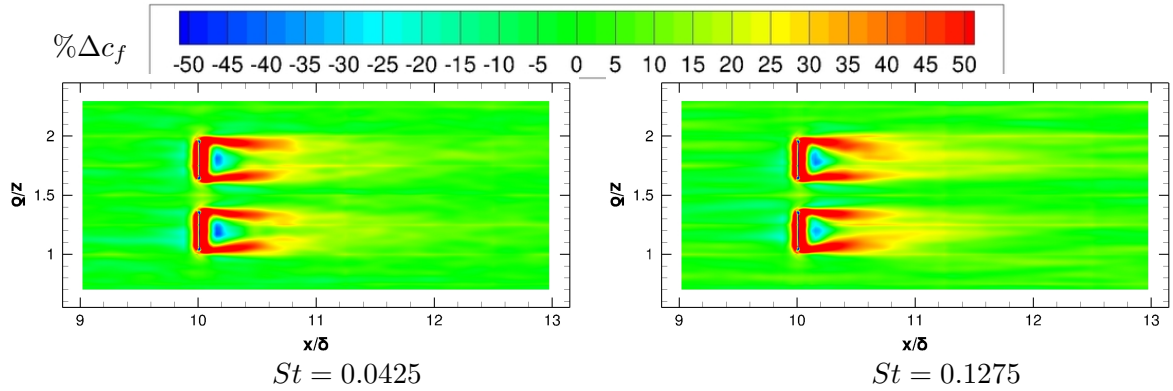

$St = 0.0425$ $St = 0.1275$

Figure 3.39: **St=0.1275, r=0.2:** Spatial map of change in time-averaged skin friction coefficient.

overpredict skin friction.

3.6.6 Two jets, $Re_\theta = 3230$, $St = 0.1275$, $r = 0.2$

In this case we increase the Strouhal number to 0.1275 with a blowing ratio of 0.2. This is one of the higher frequency cases identified in the early experimental campaign to map parameters as potentially leading to skin friction drag reduction [2]. The experiments indicate a drag reduction on the order of -0.2%.

Change in skin friction

Figure 3.39 compares maps of change in time-averaged skin friction coefficient for Strouhal numbers 0.0425 and 0.1275 with a blowing ratio of 0.2. There is a slightly smaller region of reduced skin friction behind the jet at Strouhal number 0.1275 as compared with Strouhal number 0.0425. The region of increased skin

[2]The campaign to refine the parameter map at lower frequencies and blowing ratios identified several Strouhal numbers higher than 0.1275 that also showed drag reduction.

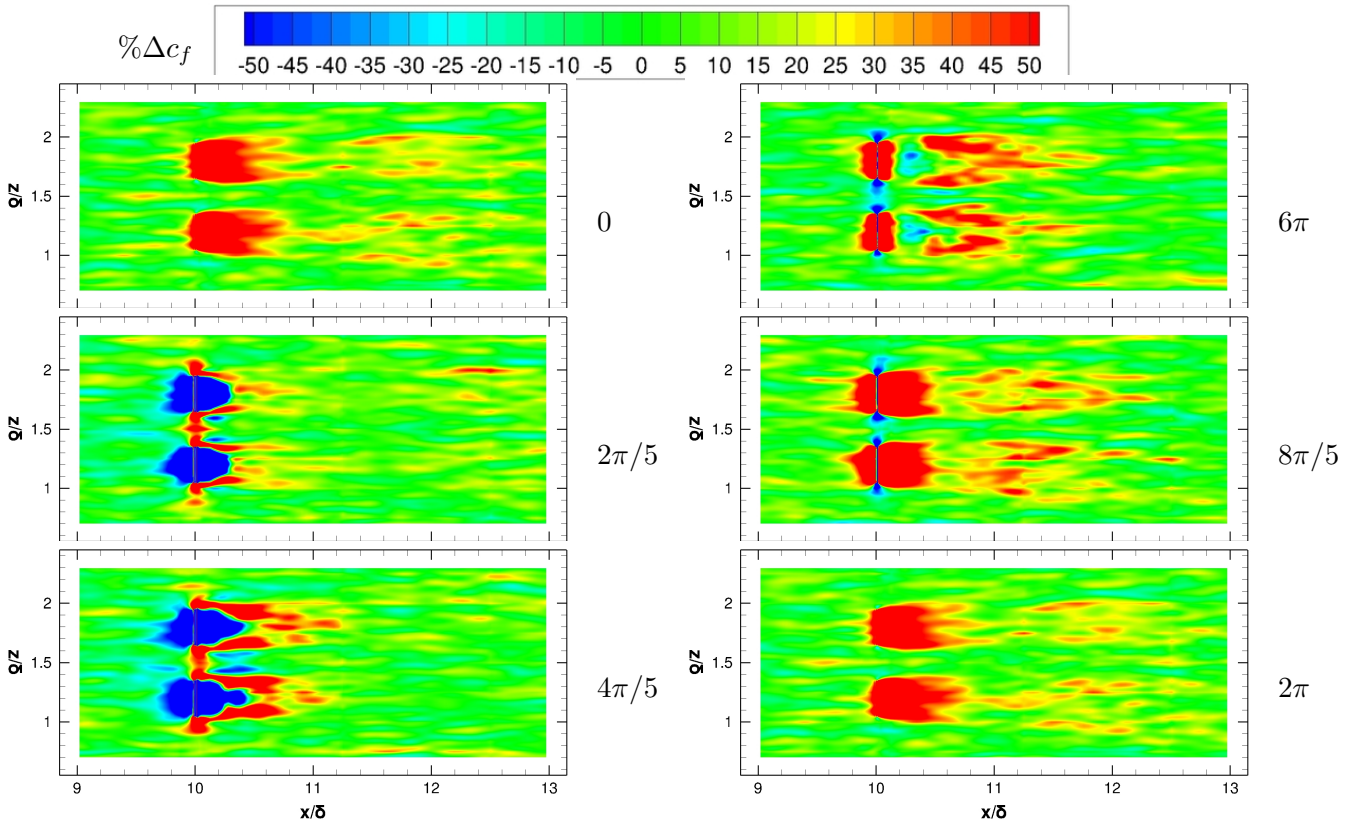

Figure 3.40: **St=0.1275, r=0.2:** Spatial maps of change in phase-averaged skin friction coefficient.

friction emanating from the sides of the jets is also slightly wider with Strouhal number 0.1275. Otherwise, the features of the two controlled flows are very similar.

The contrast between the change in phase-averaged skin friction coefficient for the two Strouhal numbers can be seen in Figures 3.32 and 3.40. The large changes in skin friction near the jet are very similar in the two cases. However, the formation of the long regions of increased skin friction emanating from the edges of the jets propagate downstream at different rates through the cycle. At the lower Strouhal number of 0.0425 this feature is much more prominent during the blowing phase and extends downstream $2\delta_\circ \rightarrow 3\delta_\circ$. It then quickly dissipates through the suction phase of the jet. In contrast, at the higher Strouhal number of 0.1275 the increase in skin friction emanating from the sides of the jet appears later in the cycle. It then convects downstream through the suction phase and into the next blowing phase. This difference in behaviour is likely due to the difference in forcing period relative to the flow velocity. It is interesting that, despite having different behaviour though the phases of the jet, the time-averaged maps are very similar.

Integrating over the region used with the experimental data to create the parameter maps, the drag increases in the computations by about 3.3%. Using the larger area spanned by $\{x \times z\} = \{[5, 15] \times [0, 3]\}\delta_\circ$, excluding the spanwise strip where the jets are located $x = [9.99, 10.01]\delta_\circ$, the drag increases by about 2.8%.

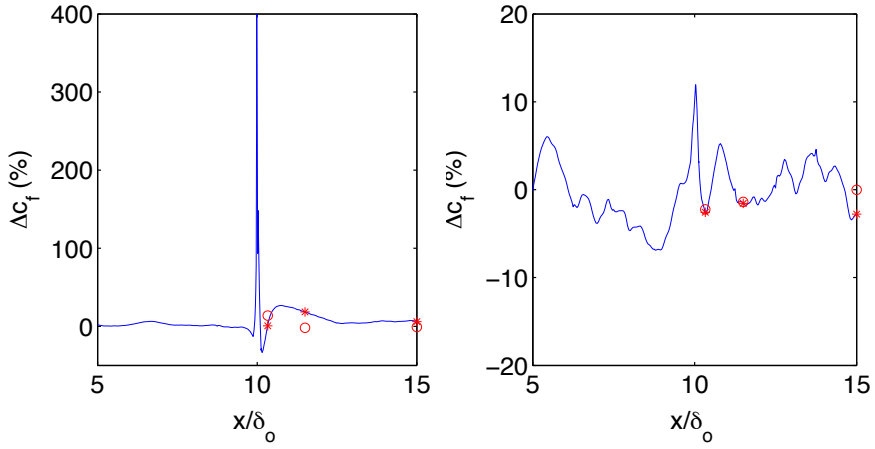

Figure 3.41: **St=0.1275, r=0.2:** Change in time-averaged skin friction coefficient along jet centerline [left] and along the streamwise line between the jets [right]. Open symbols are from the experimental data; asterisks are the same points from the computations.

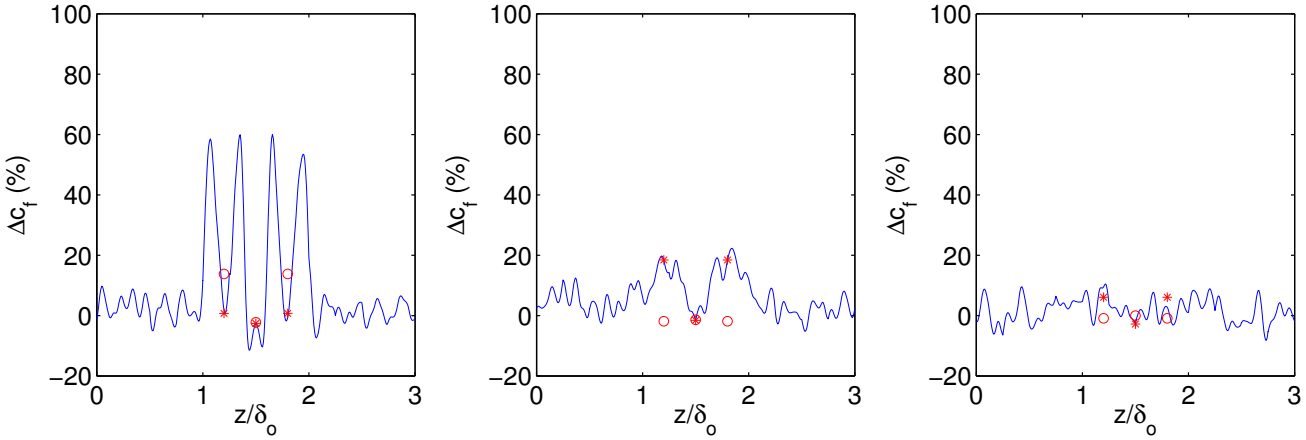

Figure 3.42: **St=0.1275, r=0.2:** Change in time-averaged skin friction coefficient along spanwise lines of $x = 10.33\delta_\circ$ [top left], $x = 11.5\delta_\circ$ [top right], and $x = 15\delta_\circ$ [bottom]. Open symbols are from the experimental data; asterisks are the same points from the simulations. The curves are also from simulation data.

Comparison with experiment

Figures 3.41 and 3.42 compare the change in time-averaged skin friction coefficient along the streamwise and spanwise lines corresponding to the experimental measurement locations. Similar features are present compared with the previous cases. Taking into account the differences in the simulations and experiments, as well as the rectification of the experimental data, good agreement is obtained.

3.6.7 Two jets, $Re_\theta = 3230$, $St = 0.2550$, $r = 0.1$

The early experimental campaign to map parameters identified Strouhal number 0.2550 and blowing ratio 0.1 as being at the edge of the region potentially leading to skin friction drag reduction. This case was chosen to see how well the computations could match this cutoff identified in the experiments. The later

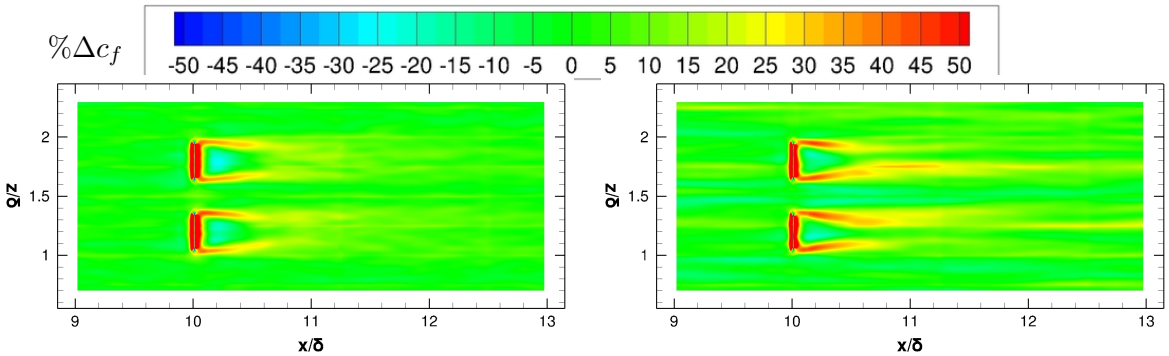

Figure 3.43: **St=0.2550, r=0.1:** Spatial map of change in time-averaged skin friction coefficient.

refined experimental study at lower frequencies and blowing ratios showed a small drag reduction with these parameters on the order of $-0.3 \pm 0.7\%$.

Change in skin friction

Figure 3.43 compares maps of change in time-averaged skin friction coefficient for Strouhal numbers 0.0425 and 0.2550 with a blowing ratio of 0.1. Similar to the Strouhal number comparison presented in the previous section, there is a slightly smaller region of reduced skin friction behind the jet at Strouhal number 0.2550 as compared with Strouhal number 0.0425. The region of increased skin friction emanating from the sides of the jets is also slightly wider and more pronounced at Strouhal number 0.2550. Otherwise, the features of the two actuated flows are very similar.

The difference in change in phase-averaged skin friction coefficient can be seen by considering Figures 3.28 and 3.44. At the higher Strouhal number the large changes in skin friction near the jet seem to be more localized. As before, the features emanating from the edges of the jets also appear later in the cycle and persist into the beginning of the next blowing phase. In this case, the features emanating from the edges of the jets appear slightly stronger, but do not convect as far downstream before dissipating. This again is likely due to the difference in the forcing period relative to the flow velocity. It is interesting that, despite having different behaviour though the phases of the jet, the time-averaged maps are very similar in this case as well.

Integrating over the region used with the experimental data to create the parameter maps, the drag increases in the computations by about 3.7%. Using the larger area spanned by $\{x \times z\} = \{[5, 15] \times [0, 3]\}\delta_\circ$, excluding the spanwise strip where the jets are located $x = [9.99, 10.01]\delta_\circ$, the drag increases by about 1.5%.

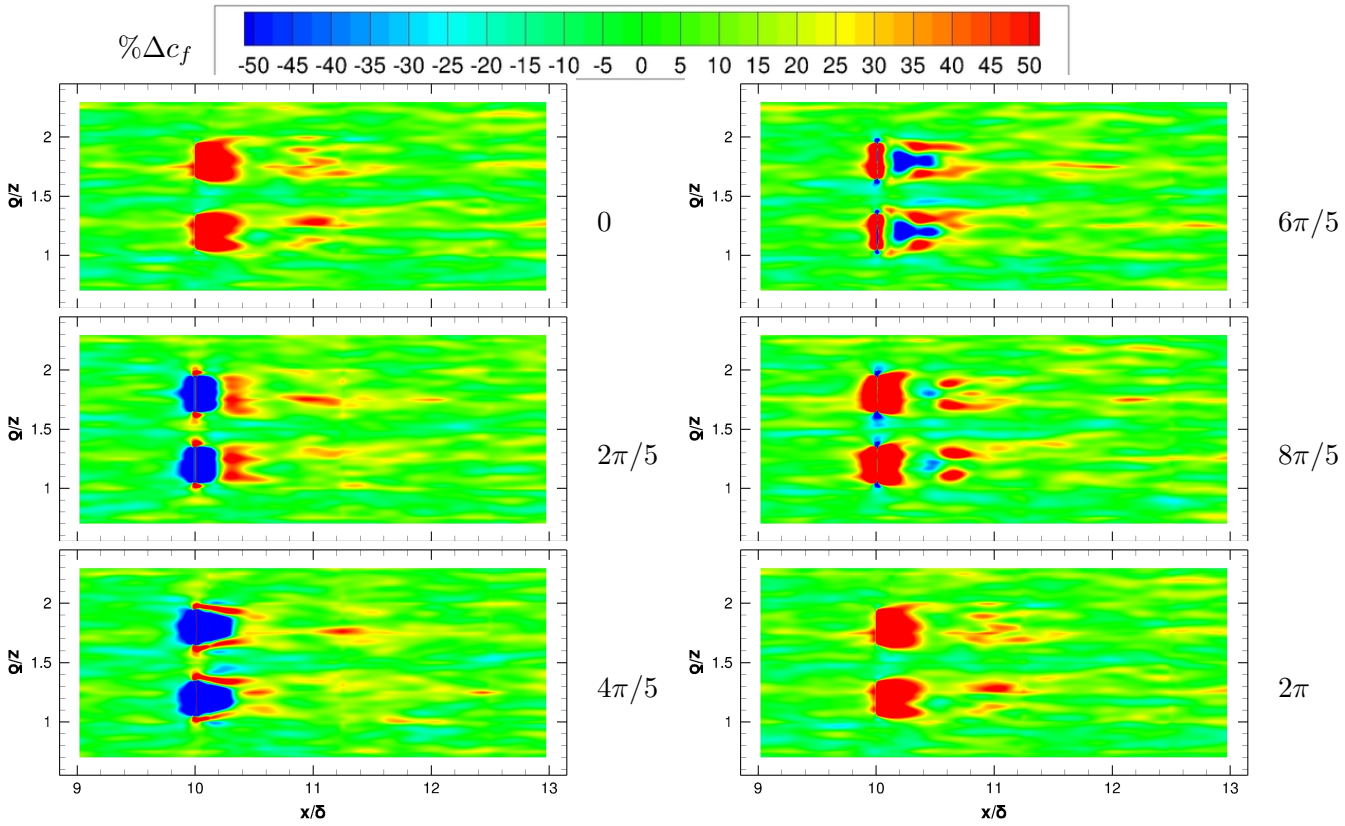

Figure 3.44: **St=0.2550, r=0.1:** Spatial maps of change in phase-averaged skin friction coefficient.

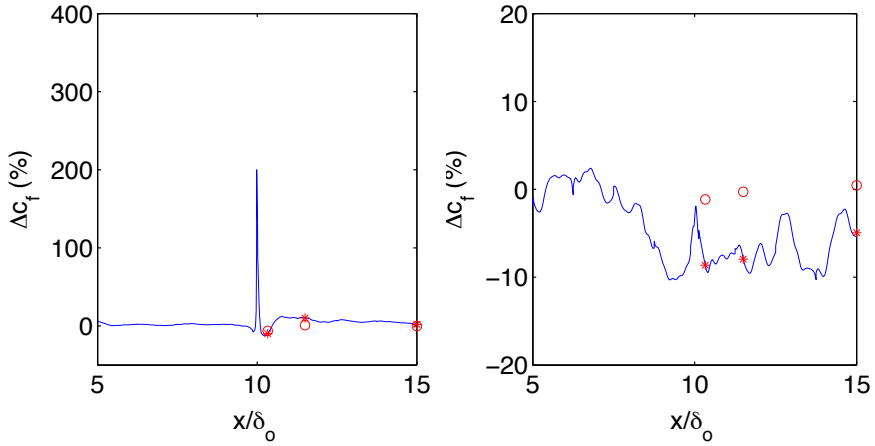

Figure 3.45: **St=0.2550, r=0.1:** Change in time-averaged skin friction coefficient along jet centerline [left] and along the streamwise line between the jets [right]. Open symbols are from the experimental data; asterisks are the same points from the computations.

Comparison with experiment

Figures 3.45 and 3.46 compare the change in time-averaged skin friction coefficient along the streamwise and spanwise lines corresponding to the experimental measurement locations. Reasonable agreement is found within the noise in the data and accounting for slight differences in the computational and experimental parameters.

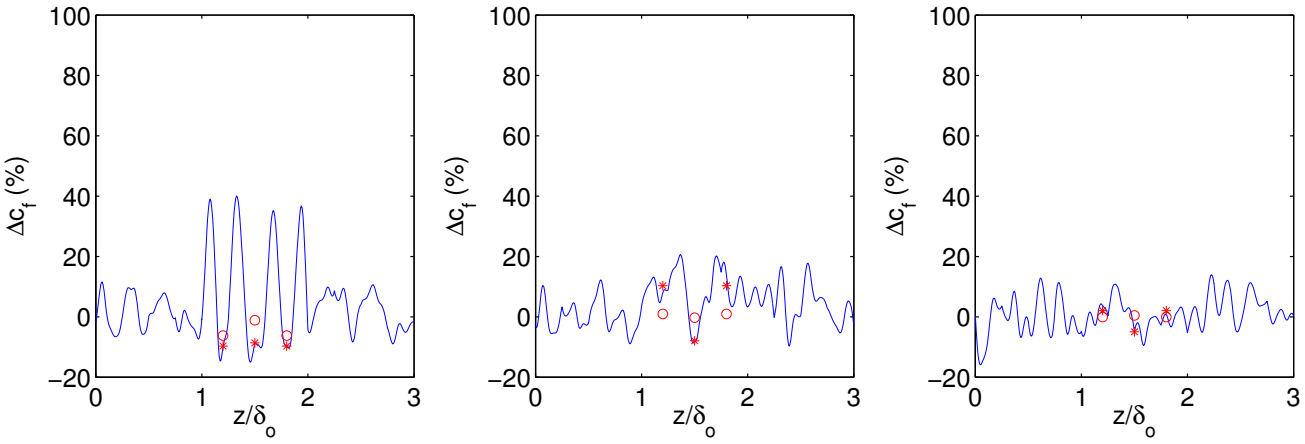

Figure 3.46: **St=0.2550, r=0.1:** Change in time-averaged skin friction coefficient along spanwise lines of $x = 10.33\delta_\circ$ [top left], $x = 11.5\delta_\circ$ [top right], and $x = 15\delta_\circ$ [bottom]. Open symbols are from the experimental data; asterisks are the same points from the simulations. The curves are also from simulation data.

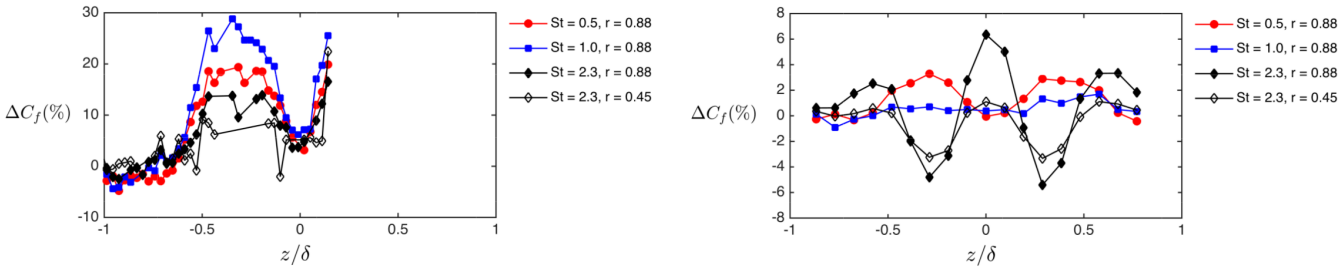

Figure 3.47: **St=2.3, r=0.44:** Change in skin friction coefficient evaluated using oil film interferometry [left] and the Clauser chart method from hot-wire data [right].

3.6.8 One jet, $Re_\theta = 4210$, $St = 2.3$, $r = 0.44$

A single jet actuated with Strouhal number 2.3 and blowing ratio 0.44 was considered in the early experimental studies discussed in Section 2.3.2. The hot-wire and oil-film interferometry identified this case as potentially yielding a reduction in skin friction far downstream of the jet, as shown in Figure 3.47. However, subsequent experimental measurements made with hot films as part of the parameter study suggest that this set of parameters will lead to an increase in skin friction drag on the order of 3 to 4%.

Change in skin friction

Figure 3.48 shows the map of the change in time-averaged skin friction coefficient. It shows an elongated strip of skin friction reduction both upstream and downstream of the jet along its centerline. The maps of the change in phase-averaged skin friction in Figure 3.49 show more detail. These show that the long region of reduced skin friction drag downstream of the jet persists throughout the entire cycle. The region of reduced skin friction upstream of the jet grows from the end of the blowing phase through to the mid

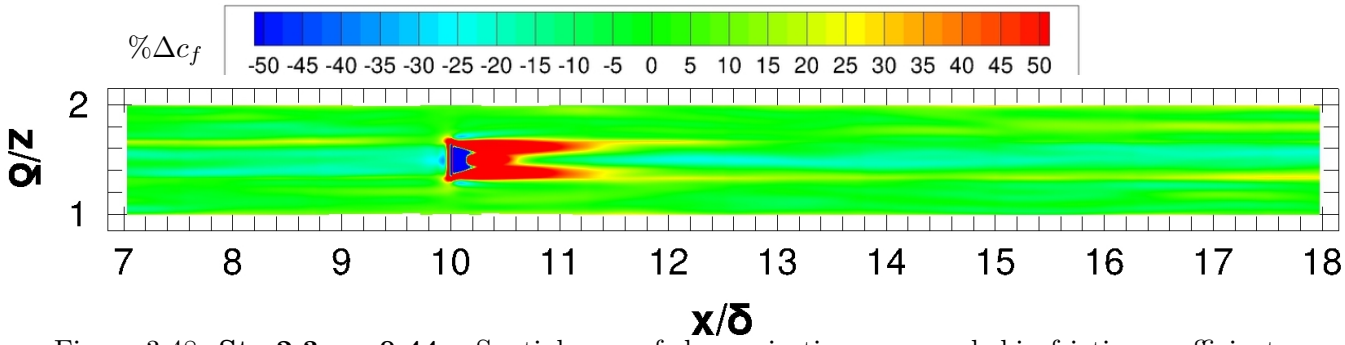

Figure 3.48: **St=2.3, r=0.44:** Spatial map of change in time-averaged skin friction coefficient.

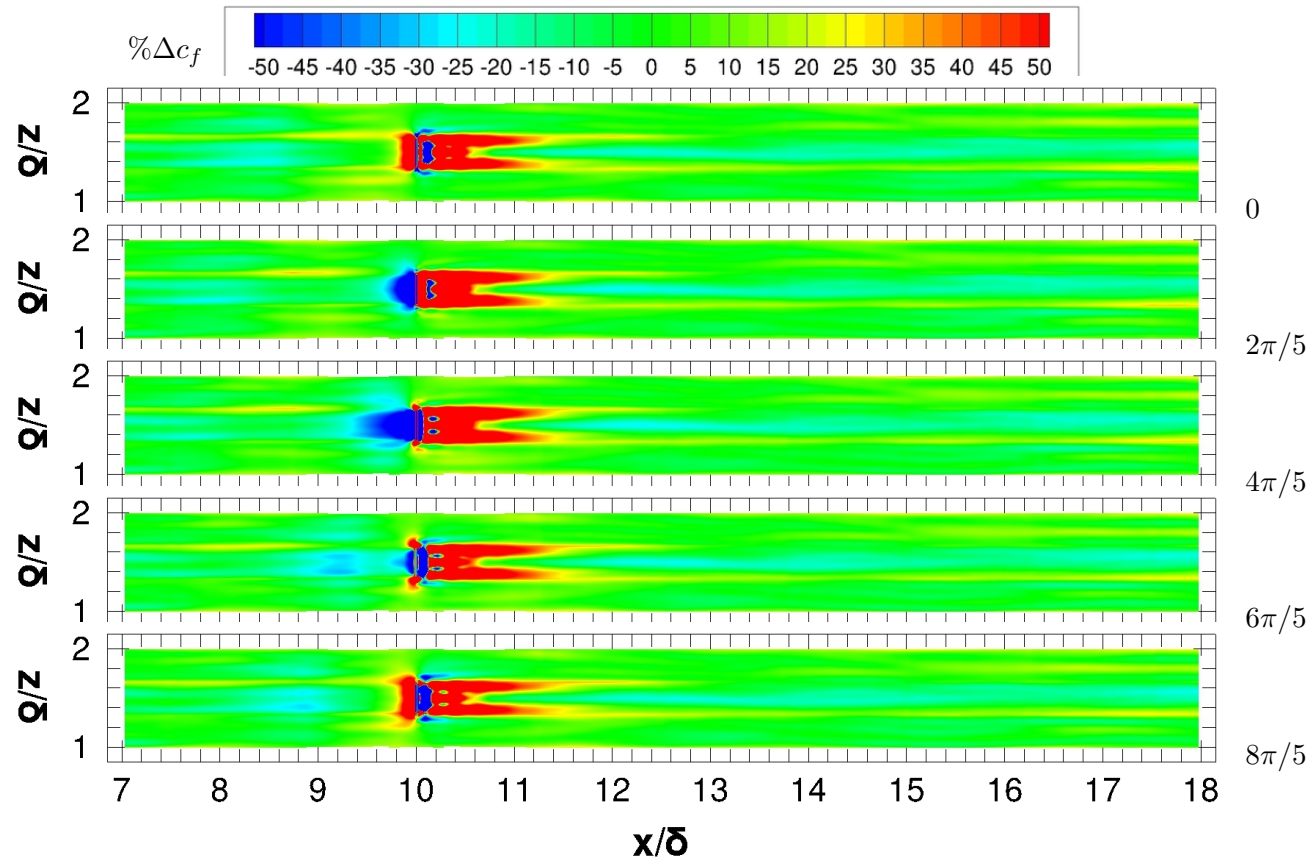

Figure 3.49: **St=2.3, r=0.44:** Spatial maps of change in phase-averaged skin friction coefficient.

point in the suction phase before decaying again.

Two long regions of increased skin friction drag emanate from the edges of the jet, and a third shorter region forms downstream along the jet's centerline. Integrating the change in skin friction coefficient over the region used with the experimental data to create the parameter maps yields a drag increase of about 3.3%. Using the larger integration area yields an increase in drag of about 1.7%.

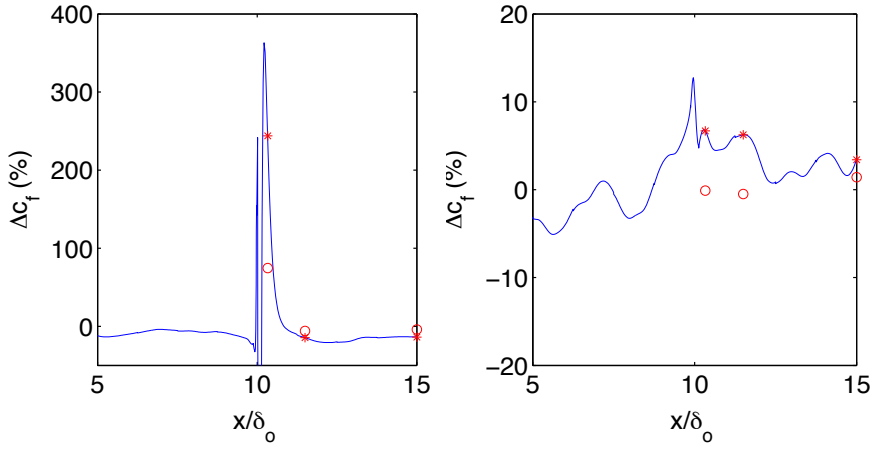

Figure 3.50: **St=2.3, r=0.44:** Change in time-averaged skin friction coefficient along jet centerline [left] and along the streamwise line between the jets [right]. Open symbols are from the experimental data; asterisks are the same points from the computations.

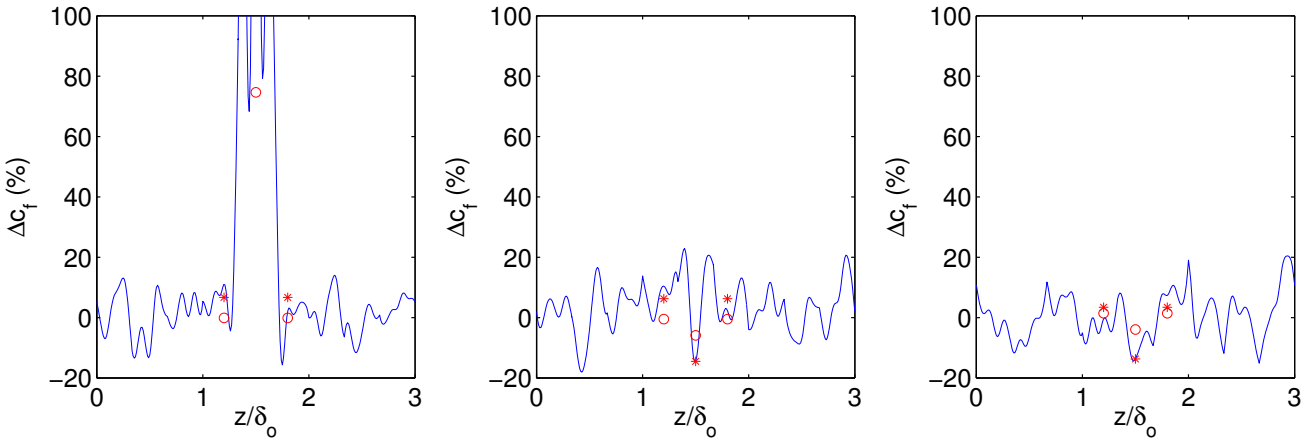

Figure 3.51: **St=2.3, r=0.44:** Change in time-averaged skin friction coefficient along spanwise lines of $x = 10.33\delta_\circ$ [top left], $x = 11.5\delta_\circ$ [top right], and $x = 15\delta_\circ$ [bottom]. Open symbols are from the experimental data; asterisks are the same points from the simulations. The curves are also from simulation data.

Comparison with experiment

Figures 3.50 and 3.51 compare the change in time-averaged skin friction coefficient along the streamwise and spanwise lines corresponding to the experimental measurement locations. In this case there is a short strong recirculation region that forms just behind the jet, then a second rapid increase in skin friction along the centerline. This was observed in the spatial maps presented above and has significant impact on the integrated change in skin friction. In general, the experimental trends are recovered and reasonable agreement is obtained at the experimental measurement locations.

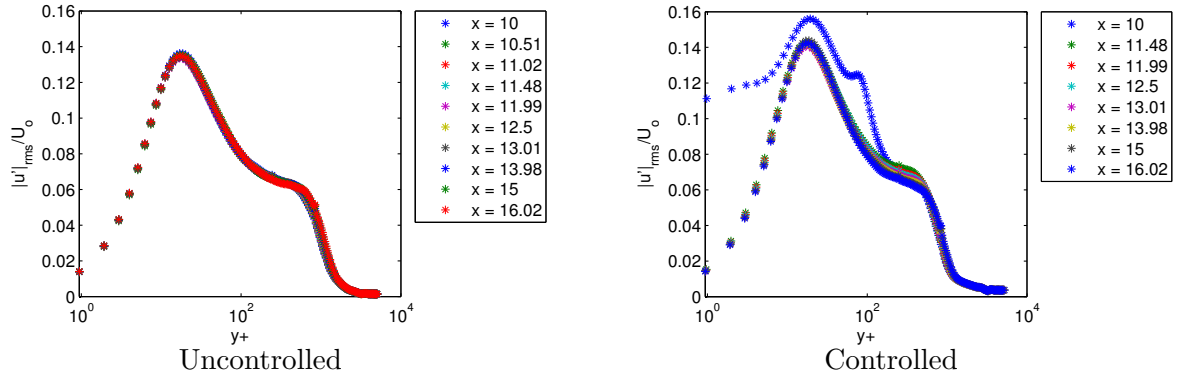

Figure 3.52: **St=0.077, r=0.675:** Fluctuating velocity profile of uncontrolled [left] and controlled [right] boundary layers.

3.6.9 One jet, $Re_\theta = 4210$, $St = 0.077$, $r = 0.675$

The motivation for this set of parameters, Strouhal number 0.077 and blowing ratio 0.675, is to introduce a second peak in the fluctuating velocity profile in the outer part of the boundary layer. Figure 3.52 compares the fluctuating velocity profiles from the uncontrolled and controlled boundary layers. The measurement at $x = 10\delta_\circ$ is taken right above the jet. This is why the profile corresponding to this location is different than the rest. These plots show that we were able to accomplish the goal of introducing a second peak in the outer part of the boundary layer through actuation. We can also see that this peak is stronger near the jet and decays downstream.

Comparison with experiment

Figure 3.53 shows the change in time-averaged skin friction drag. More detail is provided in the phase-averaged maps shown in Figure 3.54. Applying numerical quadrature to the experimental measurements give an increase in skin friction drag by about 9 to 10%. Over the same area, the computations yield an increase of about 9%. Over the larger integration area spanned by $\{x \times z\} = \{[5, 15] \times [0, 3]\}\delta_\circ$, excluding the spanwise strip where the jets are located $x = [9.99, 10.01]\delta_\circ$, the drag increases by about 3.2%.

Change in skin friction

Figures 3.55 and 3.56 compare the change in time-averaged skin friction coefficient along the streamwise and spanwise lines corresponding to the experimental measurement locations. Reasonably good agreement is found between the experimental and computational results, especially in terms of trends. This gives us increased confidence in both results.

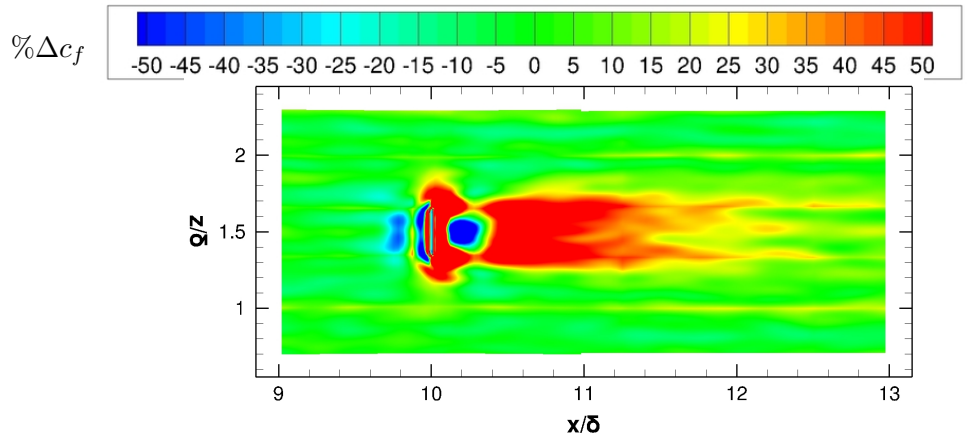

Figure 3.53: **St=0.077, r=0.675:** Spatial map of change in time-averaged skin friction coefficient.

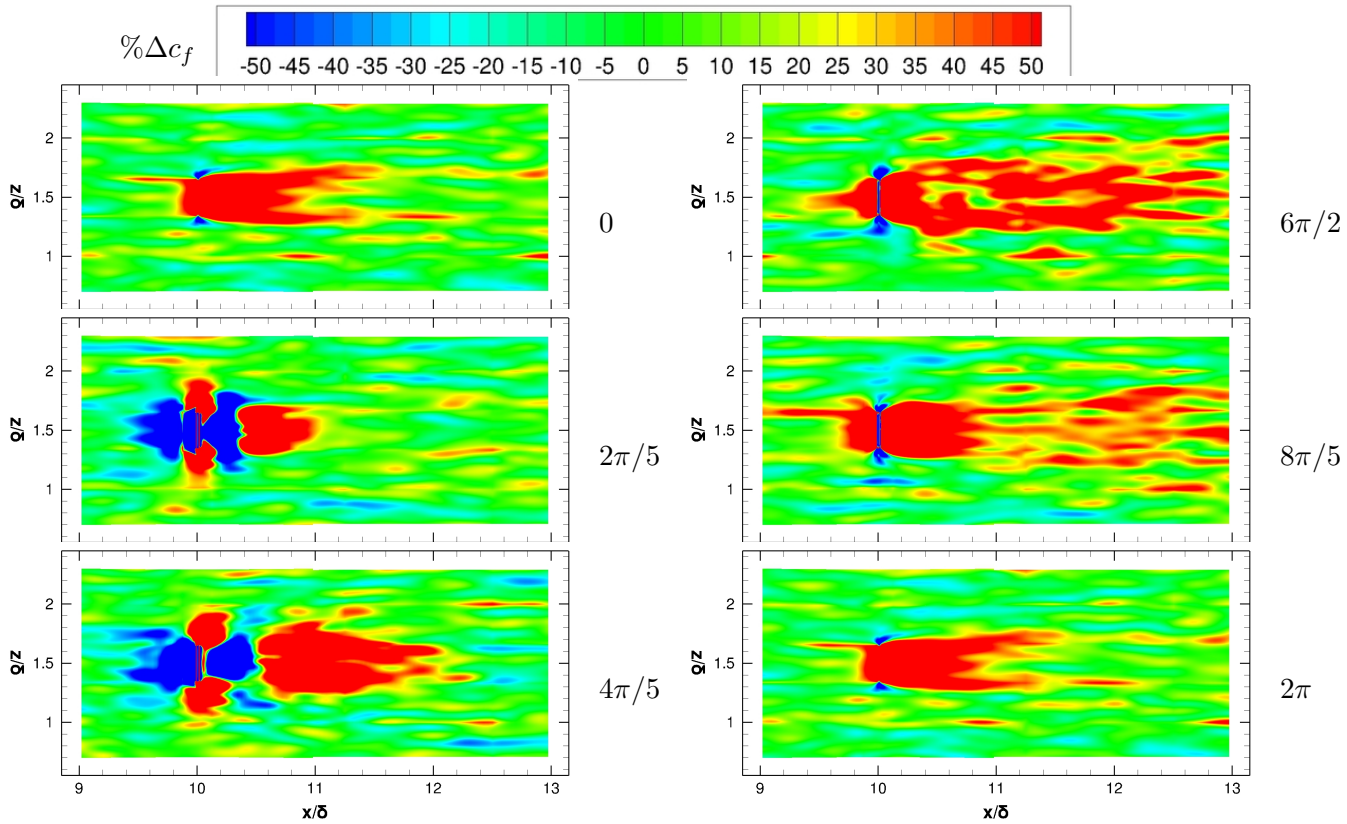

Figure 3.54: **St=0.077, r=0.675:** Spatial maps of change in phase-averaged skin friction coefficient.

3.7 Summary of Numerical Simulations

Uncontrolled simulations were performed at a variety of Reynolds numbers using the implicit large-eddy simulation (LES) technique. The motivation for these simulations was to provide a reference for the controlled simulations, the primary focus of this work, and to enable various sources of error to be assessed and addressed. The ability of the implicit LES technique to capture the relevant physics of the boundary layer was investigated, and the limitations of the technique identified. The most significant limitation is the

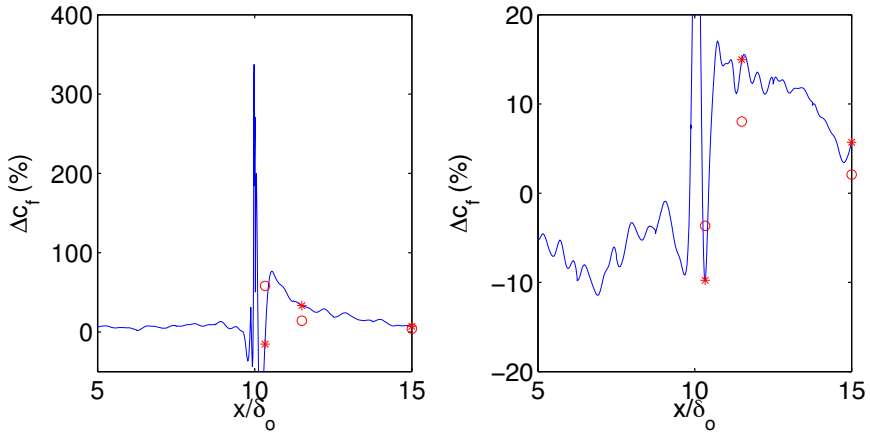

Figure 3.55: **St=0.077, r=0.675:** Change in time-averaged skin friction coefficient along jet centerline [left] and along the streamwise line between the jets [right]. Open symbols are from the experimental data; asterisks are the same points from the computations.

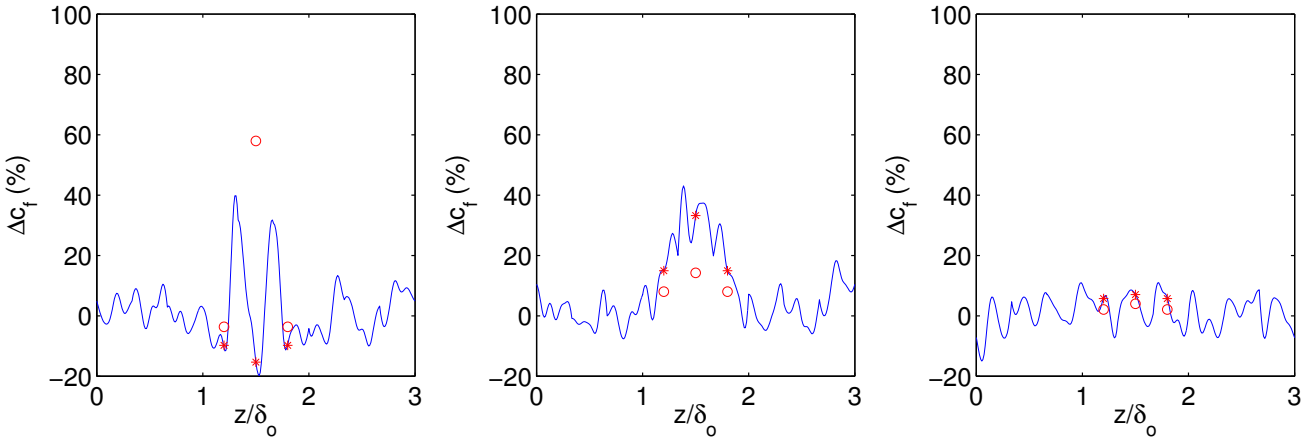

Figure 3.56: **St=0.077, r=0.675:** Change in time-averaged skin friction coefficient along spanwise lines of $x = 10.33\delta_\circ$ [top left], $x = 11.5\delta_\circ$ [top right], and $x = 15\delta_\circ$ [bottom]. Open symbols are from the experimental data; asterisks are the same points from the simulations. The curves are also from simulation data.

ability to accurately capture the magnitude of both the mean and fluctuating velocity in the buffer layer. Several diagnostics are performed at the lower Reynolds number of $Re_\theta = 1500$ to eliminate additional sources of error coming from compressibility effects and pressure gradients. Further confirmation that the limitations are due to the implicit LES technique is obtained through direct numerical simulation. Moreover our LES results are consistent with other results seen in the literature. Despite the error predicting the magnitude of the velocity in the buffer layer, the mean and fluctuating velocities correlate as expected. This is observed in simulations of the higher experimental Reynolds numbers as well.

Six sets of control parameters were selected for simulation based on the parameter maps generated using rectified experimental data. Two additional simulations were presented based on earlier experimental campaigns which showed prolonged regions of skin friction reduction in one case, and the ability to modify the fluctuating content in the outer part of the boundary layer in the other case. Accounting for steep

gradients in the vicinity of some experimental measurement locations, the numerical simulations replicate the experimental values of change in skin friction reasonably well. In addition, the simulations are able to capture spatial maps of change in skin friction over the entire domain using wall shear stress values that are not rectified as in the experiments. There is often a small region of recirculation just behind the jets along their centerlines. Thus the rectification can have a significant impact on the integrated change in skin friction. Furthermore, we observe that there are regions of increased skin friction very near the jets, as well as in strands emanating from the edges of the jets. The latter is due to the formation of counter rotating vortices drawing high momentum fluid closer to the wall. These features are not captured by the quadrature points used in the experimental campaign. Unfortunately, this means that the parameters that showed promise in the experimental campaign for drag reduction show a drag increase in the computations.

The simulations of the later experiments, largely at lower Strouhal number and blowing ratio, show many transient features throughout the jet cycle. In other words, we did not observe any persistent features. In contrast, the computations of the older experiments using the higher Strouhal number of 2.3 and blowing ratio of 0.44, showed a long persistent region of drag reduction both upstream and downstream of the jet centerline. This agrees well with the experimental measurements made using oil film interferometry and the Clauser chart method from hot wire data. Unfortunately, there is also a significant region of drag increase behind the jet emanating from the edges of the jet, and a third shorter region just downstream along the jet centerline. Integrating the change in skin friction drag yields an overall drag increase. It may be worth further exploring parameters in this neighbourhood to determine if a similar persistent area of drag reduction can be obtained with less of a penalty near the jet. It may also be worth determining how far downstream the region of drag reduction persists, as it extended to the end of the simulation domain $10\delta_\circ$ downstream of the jet.

Finally, we confirmed numerically the ability of the jet to introduce a second peak in the fluctuating velocity profile, located in the outer part of the boundary layer. This mimics the goal of the particular experimental campaign, though no drag reduction was observed in either the experiments or the computations.

Chapter 4

Conclusions

This report presents both experimental and numerical investigations of the use of spanwise oriented synthetic jets to manipulate the large structures in the logarithmic region of turbulent boundary layers and their impact on skin friction. The study increases our understanding of the interaction between synthetic jets and turbulent boundary layers. This is enabled by the experimental and computational techniques developed and validated. Finally, the results of the study provide guidance on the direction of future work.

The experimental and numerical datasets show that the flow is highly receptive to low-frequency, or low Strouhal number forcing. This implies that low-frequency forcing is required to manipulate the boundary layer dynamically in an effective manner. Low-frequency forcing is also able to cause amplitude modulation in the streamwise turbulence intensity near the wall, and the experiments show that it is able to achieve skin-friction reduction. In contrast, higher-frequency actuation creates spatially and temporally persistent features, but is unable to manipulate the lower frequency structures in the logarithmic region of the boundary layer as desired. The limited number of experimental measurement locations is likely to have caused an overestimation in the predicted drag reduction. This is shown in spatial maps of change in skin friction generated from the numerical datasets. These maps identify several flow features not present at the experimental measurement locations, such as regions of recirculation and the influence of larger counter-rotating streamwise vortices generated by the synthetic jets.

The results of the current study suggest that the degree of drag reduction that can be expected from strictly open loop forcing is limited. Therefore, it is proposed to extend the current work by adding a feedforward element to the flow control system. The purpose of the sensing would be to identify the presence of low-speed streaks in the log-region such that the control system can target specific events that occur within the boundary layer. In this scenario, the control strategy would be to cause the low-speed streaks to break down prematurely, thus leading to a reduction in turbulence production. The addition of the sensing would remove the arbitrariness of the forcing and is anticipated to reduce the actuation

power utilized, since only certain events are being targeted, which can lead not only to further reduction in skin friction but also an increase in the net energy savings resulting from the flow control strategy. The proposed future work will build on the experimental techniques and simulation capabilities which have been developed and validated in the present work.

Appendix A

Experimental Data Files

A.1 Hot-Wire Measurements of Boundary Layers Actuated at High Frequency

A.1.1 Description of files

All of the data files are stored as MATLAB (.mat) files. These are the result of processing on the raw data. Table A.1.1 contains a listing of the variables that can be found in the MATLAB files. Each filename is of the form pos$I1$_case$I2$_$I3$_$I4$.mat, where $I1$ specifies which of the 12 spanwise positions the hot-wires are set at (1-12), $I2$ specifies which actuation case (1-5), $I3$ specifies whether actuation is on or off (0,1; a baseline unactuated datafile would have $I3 = 0$), and $I4$ specifies whether phase-averaging has been performed (0,1). The last part of the folder location: data_proc32_x specifies the streamwise location of the measurements (1.5, 5, 8.5, or 10.8 δ).

A.1.2 List of files

- data_proc32_1p5\pos[1-12]_case1_0_1.mat
- data_proc32_5\pos[1-12]_case1_0_1.mat
- data_proc32_8p5\pos[1-12]_case1_0_1.mat
- data_proc32_10p8\pos[1-12]_case1_0_1.mat
- data_proc32_1p5\pos[1-12]_case[1-5]_1_1.mat
- data_proc32_5\pos[1-12]_case[1-4]_1_1.mat
- data_proc32_5\pos[1-12]_case[1-4]_1_1.mat
- data_proc32_8p5\pos[1-12]_case[1-4]_1_1.mat
- data_proc32_10p8\pos[1-12]_case[1-4]_1_1.mat

Variable	Type	Description
act_info	1×9 struct	Information about the synthetic jet actuation. Contains one field "info" which contains 10 values: F1, F2, O1, O2, PS1, PS2, the input voltages of jets 1 and 2, and the function generator time series for jet 1 and 2.
ActualRate_DAQ	1×1 double	Sampling frequency actually used by the data acquisition system [Hz].
cali_name1	1×21 char	String containing the file name of the hot-wire calibration before boundary layer trace.
cali_name2	1×21 char	String containing the file name of the hot-wire calibration after boundary layer trace.
f	1×8193 double	Vector of frequencies for use with Fourier transformed quantities [Hz].
F1	1×13 char	String containing the frequency of synthetic jet actuation for jet 1 in Hz.
F2	1×13 char	Frequency of synthetic jet actuation for jet 2 [Hz].
F_calc	1×42 double	Calculated synthetic jet actuation frequency for every point in the boundary layer trace [Hz].
FG_p	42×33 double	Phase-averaged input signal from the function generator [V].
fs	1×1 double	Sampling frequency [Hz].
hw_gain[1,2]	1×1 double	Hot-wire voltage gain for the two hot-wires.
hw_offset[1,2]	1×1 double	Hot-wire offset for the two hot-wires [V].
king_coef[1,2]	1×3 double	King's law fit coefficients for the two hot-wires.
O[1,2]	1×2 char	Flag indicating whether jet 1 and jet 2 output is turned on or off.
overlap	1×1 double	Amount of overlap between FFT bins.
P_atm	1×1 double	Atmospheric pressure [kPa].
phas_act	1×1 double	Phase of the actuation.
phas_dr	1×1 double	Half the size of the bins for phase averaging.
phas_pts	1×1 double	Number of bins, or points, in the phase averaging.
PS[1,2]	1×1 double	The phases of jet 1 and 2 from the function generator.
PT_Qa	1×42 double	Freestream velocity as measured by the Pitot tube at each y-location in the boundary layer trace [m/s].
Puu[1,2]	8193×42 double	PSD of the 2 hot-wire velocity signals at each y-location.
pxx_bin	1×1 double	Number of FFT bins.
Q[1,2]_pk	42×33 double	Phase-averaged mean streamwise velocity for each of the hot-wires at each y-location [m/s].
Q[1,2]_pk_bpf	42×33 double	Band pass filtered phase-averaged mean streamwise velocity for each of the hot-wires at each y-location [m/s].
qq[1,2]_pkm	42×33 double	Phase-averaged variance of the streamwise velocity fluctuations for each of the hot-wires at each y-location [m^2/s^2].
qq[1,2]_pkp	42×33 double	Phase-averaged variance of the streamwise velocity fluctuations for each of the hot-wires at each y-location [m^2/s^2].
rho_air	1×1 double	Density of the air in the wind tunnel [kg/m^3].
Ta	1×40 double	Temperature during each measurment [°C].
total_steps	1×1 double	Total number of steps traversed when locating the wall.

Variable	Type	Description
u2sw[1,2][a-c]	1×42 double	Variance of the streamwise velocity fluctuations for the 2 hot wires at each y-location [m^2/s^2] calibrated before (a), after (b), and using a linear interpolation of before and after (c).
Us[1,2]m_[a-c]	1×42 double	Mean streamwise velocity for the 2 hot wires [m/s] at each y-location calibrated before (a), after (b), and using a linear interpolation of before and after (c).
V[1,2]	1×13 char	String containing the input voltage to the function generator [V].
visc_air	1×1 double	Kinematic viscosity of the air in the wind tunnel [m^2/s].
wire_s	7×1 double	Array of steps traversed when locating the wall.
wire_v	7×2 double	Array of hot-wire velocities when locating the wall.
Y	1×40 double	Uncorrected wall-normal positions of the hot-wires during the boundary layer trace [mm].

Table A.1: Variables contained in high frequency actuation processed .mat data files.

A.2 Skin Friction Parameter Mapping

A.2.1 Description of files

All of the data files are stored as MATLAB (.mat) files. There is one file per forcing case. Table A.2 contains a listing of the variables that can be found in each MATLAB file.

In Table A.2 $N_{data} = f_s t_s$ is the number of data points sampled at a rate of f_s Hz and for t_s seconds. For the arrays with 6 columns, each column refers to a particular hot-film sensor. Columns 1,3, and 5 are directly behind the jet at 0.33δ, 1.5δ, and 5δ, respectively. Similarly, columns 2, 4, 6 are directly behind the spacing between the jets at 0.33δ, 1.5δ, and 5δ, respectively.

A.2.2 List of files

Jet spacing $\Delta = 26$ mm

- SFmeas_20170814_St1r[1-6].mat
- SFmeas_20170814_St2r[3-8].mat
- SFmeas_20170814_St3r[2-9].mat
- SFmeas_20170814_St4r[1-8].mat
- SFmeas_20170814_St5r[1-8].mat
- SFmeas_20170814_St6r[1-12].mat
- SFmeas_20170815_St1r[2-7].mat
- SFmeas_20170815_St2r[2-8].mat
- SFmeas_20170815_St3r[2-3].mat
- SFmeas_20170815_St7r[1-14].mat
- SFmeas_20170815_St8r[1-12].mat
- SFmeas_20170815_St9r[1-7].mat
- SFmeas_20170816_St3r[4-8].mat
- SFmeas_20170816_St4r[1-9].mat
- SFmeas_20170816_St5r[1-4].mat

Additional measurements at low St:

- SFmeas_20170831_St1r1_[1-4].mat
- SFmeas_20170831_St2r[1-3]_[1-4].mat
- SFmeas_20170831_St2r4_[1-3].mat
- SFmeas_20170831_St[3-9]r[1-8]_[1-3].mat
- SFmeas_20170901_St1r1_[5-10].mat
- SFmeas_20170901_St2r[1-3]_[5-10].mat
- SFmeas_20170901_St2r4_[4-10].mat
- SFmeas_20170901_St[3-9]r[1-8]_[4-10].mat

Variable	Type	Description
SJ_f	1×1 double	Frequency of synthetic jet excitation.
SJ_Uj	1×1 double	Half of the average synthetic jet velocity over the blowing half of the cycle (see Equation 2.2).
SJ[1,2]_v	1×1 double	Synthetic jet voltage from each of the speakers.
SJ[1,2]_phas	1×1 double	Phase of the signal from each of the speakers.
V_e	N_{data}×1 double	Time-series of the signal output by the function generator.
sf_e_meas	1×6 double	Average hot-film voltage during synthetic jet actuation for each of the 6 hot films.
sf_off_e_meas	1×6 double	Average baseline hot-film voltage for each of the 6 hot films. This is an average of two time-series taken before and after synthetic jet actuation.
sf[1-6]_e	N_{data}×1 double	Time-series hot-film voltage for each of the 6 hot films during actuation.
sf[1-6]_off_e	N_{data}×1 double	Time-series baseline hot-film voltage for each of the 6 hot films during actuation. This is an average of two time-series taken before and after synthetic jet actuation.
CALIB_PM	2×6 double	Calibration coefficients from straight line fit of U_τ vs hot-film voltage. Row 1 is the slope and row 2 is the y-intercept.
Date_meas	1×6 double	The date and time of measurement in the format [Y, M, D, H, M, S]
dUt	1×6 double	Change in skin friction velocity, ΔU_τ, calculated at the hot-film locations.
sf_off[1,2]_e_meas	1×6 double	Average baseline hot-film voltage for each of the 6 hot films. sf_off1_e_meas is measured before actuation, and sf_off2_e_meas is measured after actuation.
Ut_inf	1×6 double	Skin friction velocity calculated at each of the hot-film locations using the freestream velocity.
Ut_meas	1×6 double	Skin friction velocity calculated from the average hot-film voltage during synthetic jet actuation for each of the 6 hot films.
Ut_off_meas	1×6 double	Skin friction velocity calculated from the average baseline hot-film voltage for each of the 6 hot films.

Table A.2: Variables contained in skin friction parameter mapping .mat data files.

Jet spacing $\Delta = 19.5$ mm

- SFmeas_20170908_St1r[1-5]_[1-3].mat
- SFmeas_20170908_St2r[1-6]_[1-3].mat
- SFmeas_20170908_St3r[1-7]_[1-3].mat
- SFmeas_20170908_St4r[1-8]_[1-3].mat
- SFmeas_20170908_St5r[1-8]_[1-3].mat
- SFmeas_20170908_St6r[1-8]_[1-3].mat
- SFmeas_20170908_St7r[1-7]_[1-3].mat
- SFmeas_20170908_St8r[1-7]_[1-3].mat
- SFmeas_20170908_St9r[1-8]_[1-3].mat
- SFmeas_20170908_St10r[1-10]_[1-3].mat
- SFmeas_20170908_St11r[1-13]_[1-3].mat
- SFmeas_20170908_St12r[1-5]_[1-3].mat
- SFmeas_20170908_St12r[6-11]_[1-2].mat
- SFmeas_20170908_St13r[1-7]_[1-2].mat
- SFmeas_20170908_St14r[1-4]_[1-2].mat
- SFmeas_20170908_St1r[1-5]_[4-10].mat
- SFmeas_20170908_St2r[1-6]_[4-10].mat
- SFmeas_20170908_St3r[1-7]_[4-10].mat
- SFmeas_20170908_St4r[1-8]_[4-10].mat
- SFmeas_20170908_St5r[1-8]_[4-10].mat
- SFmeas_20170908_St6r[1-8]_[4-10].mat
- SFmeas_20170908_St7r[1-7]_[4-10].mat
- SFmeas_20170908_St8r[1-7]_[4-10].mat
- SFmeas_20170908_St9r[1-8]_[4-10].mat
- SFmeas_20170908_St10r[1-10]_[4-10].mat
- SFmeas_20170908_St11r[1-13]_[4-10].mat

- SFmeas_20170908_St12r[1-5]_[4-10].mat
- SFmeas_20170908_St12r[6-11]_[3-10].mat
- SFmeas_20170908_St13r[1-7]_[3-10].mat
- SFmeas_20170908_St14r[1-4]_[3-10].mat

Additional measurements at low St:

- SFmeas_20170911_St1r1_[1-7].mat
- SFmeas_20170911_St2r[1-4]_[1-7].mat
- SFmeas_20170911_St3r[1-7]_[1-7].mat
- SFmeas_20170911_St[4-9]r[1-8]_[1-7].mat
- SFmeas_20170911_St10r[1-6]_[1-7].mat
- SFmeas_20170911_St10r[7-8]_[1-6].mat
- SFmeas_20170911_St11r[1-8]_[1-6].mat
- SFmeas_20170911_St1r1_[8-10].mat
- SFmeas_20170911_St2r[1-4]_[8-10].mat
- SFmeas_20170911_St3r[1-7]_[8-10].mat
- SFmeas_20170911_St[4-9]r[1-8]_[8-10].mat
- SFmeas_20170911_St10r[1-6]_[8-10].mat
- SFmeas_20170911_St10r[7-8]_[7-10].mat
- SFmeas_20170911_St11r[1-8]_[7-10].mat

Jet spacing $\Delta = 32.5$ mm

- SFmeas_20170915_St1r[1-5]_[1-6].mat
- SFmeas_20170915_St2r[1-6]_[1-6].mat
- SFmeas_20170915_St3r[1-7]_[1-6].mat
- SFmeas_20170915_St4r[1-7]_[1-6].mat
- SFmeas_20170915_St5r[1-8]_[1-6].mat
- SFmeas_20170915_St6r[1-5]_[1-6].mat
- SFmeas_20170915_St6r[6-8]_[1-5].mat
- SFmeas_20170915_St7r[1-7]_[1-5].mat
- SFmeas_20170915_St8r[1-7]_[1-5].mat
- SFmeas_20170915_St9r[1-8]_[1-5].mat
- SFmeas_20170915_St10r[1-10]_[1-5].mat
- SFmeas_20170915_St11r[1-12]_[1-5].mat
- SFmeas_20170915_St12r[1-11]_[1-5].mat
- SFmeas_20170915_St13r[1-7]_[1-5].mat
- SFmeas_20170915_St14r[1-4]_[1-5].mat
- SFmeas_20170916_St1r[1-5]_[7-10].mat
- SFmeas_20170916_St2r[1-6]_[7-10].mat
- SFmeas_20170916_St3r[1-7]_[7-10].mat
- SFmeas_20170916_St4r[1-7]_[7-10].mat
- SFmeas_20170916_St5r[1-8]_[7-10].mat
- SFmeas_20170916_St6r[1-5]_[7-10].mat
- SFmeas_20170916_St6r[6-8]_[6-10].mat
- SFmeas_20170916_St7r[1-7]_[6-10].mat
- SFmeas_20170916_St8r[1-7]_[6-10].mat
- SFmeas_20170916_St9r[1-8]_[6-10].mat
- SFmeas_20170916_St10r[1-10]_[6-10].mat
- SFmeas_20170916_St11r[1-12]_[6-10].mat
- SFmeas_20170916_St12r[1-11]_[6-10].mat
- SFmeas_20170916_St13r[1-7]_[6-10].mat
- SFmeas_20170916_St14r[1-4]_[6-10].mat

Additional measurements at low St:

- SFmeas_20170918_St1r[1-3]_[1-4].mat
- SFmeas_20170918_St2r[1-7]_[1-4].mat
- SFmeas_20170918_St2r[1-7]_[1-4].mat
- SFmeas_20170918_St3r[1-9]_[1-4].mat
- SFmeas_20170918_St[4-8]r[1-10]_[1-4].mat
- SFmeas_20170918_St[9-11]r[1-8]_[1-4].mat
- SFmeas_20170918_St[12-17]r[1-8]_[1-3].mat
- SFmeas_20170919_St1r[1-3]_[5-8].mat
- SFmeas_20170918_St2r[1-7]_[5-8].mat
- SFmeas_20170918_St2r[1-7]_[5-8].mat
- SFmeas_20170918_St3r[1-9]_[5-8].mat
- SFmeas_20170918_St[4-8]r[1-10]_[5-8].mat
- SFmeas_20170918_St[9-11]r[1-8]_[5-8].mat
- SFmeas_20170918_St[12-17]r[1-8]_[4-8].mat

A.3 Hot-Wire Measurements of Boundary Layers Actuated at Low Frequency

A.3.1 Description of files

All of the data files are stored as MATLAB (.mat) files. These are the result of processing on the raw data. There are two types of files which contain (1) actuated (which contain "Spect_Filt") and (2) unactuated data (which end in "_baseline"). These files have filenames with the following form: Code2_pos$I1$_case$x$_$I2$_$I3$_$I4$. Here, $I1$ is an identifier specifying the spanwise position of the hot wire (a number between 1-3 as there were three spanwise positions of the hot wires), position of the hot wire downstream of the jets in boundary layer thicknesses (1.5 (written as 15), 3, 6, or 9), and whether the data is part of the blowing ratio study (01 for blowing ratio study); $I2$ is an identifier for whether actuation is on or off (1, 0); $I3$ is an identifier for whether phase-averaging was completed (1, 0); and $I4$ is an identifier for which hot-wires were active (1111 indicates 4 active hot-wires). Furthermore, x is the case number from 1-6. Case 1 is the unactuated case, while cases 2-6 are actuated with synthetic jets. Table A.3.1 contains a listing of the variables that can be found in the MATLAB files.

A.3.2 List of files

Unactuated jets - Low frequency

- Code2_pos[1-3]15_case1_1111_baseline.mat
- Code2_pos[1-3]3_case1_1111_baseline.mat
- Code2_pos[1-3]6_case1_1111_baseline.mat

Unactuated jets - Low frequency blowing ratio study

- Code2_pos[1-3]301_case1_1111_baseline.mat
- Code2_pos[1-3]601_case1_1111_baseline.mat
- Code2_pos[1-4]901_case1_1111_baseline.mat
- Code2_pos11501_case1_1111_baseline.mat
- Code2_pos36201_case1_1111_baseline.mat

Actuated jets - Low frequency

- Code2_Spect_Filt_pos[1-3]15_case[2-5]_1_1_1111.mat
- Code2_Spect_Filt_pos[1-3]3_case[2-5]_1_1_1111.mat
- Code2_Spect_Filt_pos[1-3]6_case[2-5]_1_1_1111.mat

Actuated jets - Low frequency blowing ratio study

- Code2_Spect_Filt_pos[1-3]301_case[2-6]_1_1_1111.mat

- Code2_Spect_Filt_pos[1-3]601_case[2-6]_1_1_1111.mat
- Code2_Spect_Filt_pos[1-3]901_case[2-6]_1_1_1111.mat
- Code2_Spect_Filt_pos4901_case[2-5]_1_1_1111.mat
- Code2_Spect_Filt_pos11501_case[2-6]_1_1_1111.mat
- Code2_Spect_Filt_pos36201_case[2-5]_1_1_1111.mat

Variable	Type	Description
act_info	1×9 struct	Information about the synthetic jet actuation. Contains one field "info" which contains 9 values: F1, F2, O1, O2, PS1, PS2, the input voltages of jets 1 and 2, and the function generator time series.
ActualRate_DAQ	1×1 double	Sampling frequency actually used by the data acquisition system [Hz].
cali_name1	1×21 char	String containing the file name of the hot-wire calibration before boundary layer trace.
cali_name2	1×21 char	String containing the file name of the hot-wire calibration after boundary layer trace.
D	1×2 digitalFilter	High pass filter object.
data_length[A,B]	1×1 double	Number of data points for each of the two halves of the data (A and B).
f	1×7384 double	Vector of frequencies for use with Fourier transformed quantities [Hz].
F1	1×13 char	String containing the frequency of synthetic jet actuation for jet 1 in Hz.
F2	1×13 char	Frequency of synthetic jet actuation for jet 2 [Hz].
F_act_calc	1×1 double	Calculated synthetic jet actuation frequency based on a sinusoidal fit of the function generator output signal [Hz].
F_calc	1×40 double	Calculated synthetic jet actuation frequency for every point in the boundary layer trace [Hz].
F_calc_b	1×40 double	Calculated synthetic jet actuation frequency for every point in the boundary layer trace for the second half of the data [Hz].
F_use	1×2 double	Actuation frequencies used [Hz].
FG_p	4×33×40 double	Phase-averaged input signal from the function generator [V].
FG_p_b	4×33×40 double	Phase-averaged input signal from the function generator for the second half of the data [V].
fs	1×1 double	Sampling frequency [Hz].
O1	1×2 char	Flag indicating whether jet 1 output is turned on or off.
O2	1×2 char	Flag indicating whether jet 2 output is turned on or off.
overlap	1×1 double	Amount of overlap between FFT bins.
P_atm	1×1 double	Atmospheric pressure [kPa].
phas_act	1×1 double	Phase of the actuation.
phas_dr	1×1 double	Half the size of the bins for phase averaging.
phas_pts	1×1 double	Number of bins, or points, in the phase averaging.
PS[1,2]	1×1 double	The phases of jet 1 and 2 from the function generator.
PT_Q	1×40 double	Freestream velocity as measured by the Pitot tube at each y-location in the boundary layer trace [m/s].
PT_Qa	1×40 double	Freestream velocity as measured by the Pitot tube at each y-location in the boundary layer trace for the first half of the data [m/s].
Puu1	7384×4×40 double	PSD of each hot-wire velocity signal at each y-location.
Puu1[a,b]	7384×4×40 double	PSD of each hot-wire velocity signal at each y-location for the first and second half of the data, respectively.
pxx_bin	1×1 double	Number of FFT bins.
Q1_[pk,pk_b]	33×4×40 double	Phase-averaged mean streamwise velocity for each of the hot-wires for both the first and second halves of the data [m/s].

Variable	Type	Description
Q_p_[uu,uu_b]	33×4×40 double	Phase-averaged variance of the streamwise velocity fluctuations for each of the hot-wires for both the first and second halves of the data [m/s]. An average is taken of the data from the first and second halves.
Q_p_[uuf1,uuf1_b]	33×4×40 double	Low pass filtered (below F_act) phase-averaged variance of the streamwise velocity fluctuations for each of the hot-wires for both the first and second halves of the data [m/s].
Q_p_[uuf123,uuf123_b]	33×4×40 double	Low pass filtered (below 3F_act) phase-averaged variance of the streamwise velocity fluctuations for each of the hot-wires for both the first and second halves of the data [m/s].
Q_p_[uum,uum_b]	33×4×40 double	Phase-averaged variance of the streamwise velocity fluctuations for each of the hot-wires for both the first and second halves of the data [m/s].
QhwSm	4×1 double	Mean streamwise velocity for each of the hot-wires at the wall-normal position closest to the wall with the actuation turned off [m^2/s^2].
QhwSuu	4×1 double	Variance of the streamwise velocity fluctuations for each of the hot-wires at the wall-normal position closest to the wall with the actuation turned off [m^2/s^2].
Qsj_a	40×4 double	Mean streamwise velocity for each hot-wire taken during measurements [m/s].
Qstdsj_a	40×4 double	Standard deviation of streamwise velocity fluctuations for each hot-wire taken during measurements [m/s].
rho_air	1×1 double	Density of the air in the wind tunnel [kg/m^3].
Ta	1×40 double	Temperature during each measurment [°C].
total_steps	1×1 double	Total number of steps traversed when locating the wall.
u2sw_3	4×40 double	Variance of the streamwise velocity fluctuations for the 4 hot wires [m^2/s^2].
Uswm_[1-3]	4×40 double	Mean streamwise velocity for the 4 hot-wires [m/s]. Uswm_1 is calibrated with the calibration before the boundary layer trace, Uswm_2 is calibrated with the calibration after, and Uswm_3 takes into account both calibrations.
uu_f	4×40×2 double	Variance of the high pass filtered streamwise velocity fluctuations for each of the hot-wires at each y-location [m^2/s^2].
uu_f1	4×40 double	Variance of the low pass filtered (below F_act) streamwise velocity fluctuations for each of the hot-wires at each y-location [m^2/s^2].
uu_f123	4×40 double	Variance of the low pass filtered (below 3F_act) streamwise velocity fluctuations for each of the hot-wires at each y-location [m^2/s^2].
visc_air	1×1 double	Kinematic viscosity of the air in the wind tunnel [m^2/s].
wire_s	10×1 double	Array of steps traversed when locating the wall.
wire_v	10×4 double	Array of hot-wire velocities when locating the wall.
Y	1×40 double	Uncorrected wall-normal positions of the hot-wires during the boundary layer trace [mm].

Table A.3: Variables contained in low frequency actuation processed .mat data files.

Appendix B

Computational Solution Files

B.1 Description of files

The computational grid (grid.gS, grid.gP) and flow solution (unsteady_XX.q*, unsteady_XX.istat*, unsteady_XX.pqp*) files are written with double-precision in FORTRAN binary plot3D format. The two grid files are distinct in that the first gives the full solution domain (grid.gS), and second a limited number of important planes in the domain (grid.gP). The second file was created, along with complementary solution files, to reduce storage requirements. Each grid file is organized as follows:

Line 1 Integer for the total number of computational blocks (N)

Line 2 Three integers for each computational block ($3N$ integers), giving the dimensions of the block ($jmax$, $kmax$, $mmax$)

Line 3 Computational block 1 ($jmax$(block 1) $\times$ $kmax$(block 1) $\times$ $mmax$(block 1) $\times$ 3 double-precision real numbers): Coordinates for each node in the computational block organized in the following order: (j, k, m, n), where n indicates the coordinate direction (x, y, z)

$\vdots$ $\vdots$ $\vdots$

Line N+2 Computational block N ($jmax$(block N) $\times$ $kmax$(block N) $\times$ $mmax$(block N) $\times$ 3 double-precision real numbers): Coordinates for each node in the computational block organized in the following order: (j, k, m, n), where n indicates the coordinate direction (x, y, z)

The solution files store: unsteady_XX.q*) the nondimensional flow variables (density (ρ), momentum (ρu, ρv, ρw), and energy (e)); unsteady_XX.q*) the nondimensional flow variables for a limited number of im-

portant planes in the domain; unsteady_XX.istat*) variables for visualizing flow structures (vorticity (ω_x, ω_y, ω_z), Q-criterion, λ2-criterion); and unsteady_XX.pqp*) fluctuating variables for a limited number of important planes in the domain (streamwise planes: (ρ', $\rho u'$, $\rho v'$, $\rho w'$, e'); and wall-normal planes: friction velocity ($q4 = u_\tau$)). Like the grid files, the flow solution files are organized as follows:

Line 1 Integer for the total number of computational blocks (N)

Line 2 Three integers for each computational block ($3N$ integers), giving the dimensions of the block ($jmax$, $kmax$, $mmax$)

Line 3 Computational block 1 (4 double-precision real numbers): [Mach number, Angle of attack, Reynolds number, Solution time]

Line 4 Computational block 1 ($jmax$(block 1) $\times$ $kmax$(block 1) $\times$ $mmax$(block 1) $\times$ 5 double precision real numbers): Solution variables for each node in the computational block organized in the following order: (j, k, m, n), where n indicates the variable ($q1$, $q2$, $q3$, $q4$, $q5$)

$\vdots$ $\vdots$ $\vdots$

Line 2N+1 Computational block N (4 double-precision real numbers): [Mach number, Angle of attack, Reynolds number, Solution time]

Line 2N+2 Computational block N ($jmax$(block N) $\times$ $kmax$(block N) $\times$ $mmax$(block N) $\times$ 5 double precision real numbers): Solution variables for each node in the computational block organized in the following order: (j, k, m, n), where n indicates the variable ($q1$, $q2$, $q3$, $q4$, $q5$)

Additional binary data files (unsteady_XXXXXXX.pd*) are included with time-averaged boundary layer properties for each of a limited number of important planes in the domain. The files are organized as follows:

Integer Total number of data planes (N)

Integer For each data plane (N integers), the number of data sets associated with that plane

For each plane and data set:

Integer streamwise direction index ($x = 1$, $y = 2$, $z = 3$)
Integer chordwise direction index ($x = 1$, $y = 2$, $z = 3$)
Integer wall-normal direction index ($x = 1$, $y = 2$, $z = 3$)
Integer streamwise direction computational index ($\xi = 1$, $\eta = 2$, $\zeta = 3$)
Integer chordwise direction computational index ($\xi = 1$, $\eta = 2$, $\zeta = 3$)
Integer wall-normal direction computational index ($\xi = 1$, $\eta = 2$, $\zeta = 3$)
Integer number of nodes in chordwise direction (**nchrd**)
Integer number of nodes in wall-normal (**nnrml**)
DP real streamwise location of plane
DP real spanwise width of plane
DP real momentum thickness (θ)
DP real boundary-layer thickness (δ_{99})
DP real displacement thickness (δ^*)
DP real shape factor (H)
DP real recycling parameter (γ)
DP real averaging time scale
DP real momentum thickness Reynolds number (Re_θ)
DP real friction velocity Reynolds number (Re_τ)
DP real friction velocity (u_τ)
DP real friction velocity (u_τ)
DP real kinematic viscosity (ν)
DP real kinematic viscosity (ν)
nnrml DP real wall-normal nodal locations (y)
nnrml DP real turbulence scaled wall-normal nodal locations ($\mathrm{y}^+ = y * u_\tau/\nu$)
nnrml DP real wall-normal nodal locations scaled by boundary-layer thickness (η)
nnrml DP real turbulence scaled mean streamwise velocity ($\mathrm{u}^+ = u/u_\tau$)
nnrml DP real rescaling weight function ($\mathcal{W}$)
4 × nnrml DP real Mean flow variables ($\bar{\rho}$, U, V, $\bar{e}$)
4 × nnrml DP real Mean flow variables ($\bar{\rho}$, U, V, $\bar{e}$)
12 × nnrml DP real Mean statistics ($\bar{u}\bar{u}$,$\bar{v}\bar{v}$,$\bar{w}\bar{w}$,$\bar{u}\bar{v}$,$\bar{v}\bar{w}$,$\bar{w}\bar{u}$,$|u'|$,$|v'|$,$|w'|$,$|u'|^2$,$|v'|^2$,$|w'|^2$)
12 × nnrml DP real Mean statistics ($\bar{u}\bar{u}$,$\bar{v}\bar{v}$,$\bar{w}\bar{w}$,$\bar{u}\bar{v}$,$\bar{v}\bar{w}$,$\bar{w}\bar{u}$,$|u'|$,$|v'|$,$|w'|$,$|u'|^2$,$|v'|^2$,$|w'|^2$)
nnrml DP real Quadrature weights in wall-normal direction
nchrd DP real Quadrature weights in chordwise direction

B.2 List of files

Uncontrolled simulation at $Re_\theta = 3230$

- grid.gS
- grid.gP
- unsteady_[0008440:10:0018720].q6
- unsteady_[0008440:10:0018720].pd6
- unsteady_[0008440:1:0018720].pq6
- unsteady_[0008440:1:0018720].pqp6

Uncontrolled simulation at $Re_\theta = 4210$

- grid.gS
- grid.gP
- unsteady_[0015000:10:0015840].q3
- unsteady_[0015000:10:0015840].pd3
- unsteady_[0015000:1:0015840].pq3
- unsteady_[0015000:1:0015840].pqp3

Controlled simulation with $St = 0.010625$ and $r = 0.15$

- grid.gS
- grid.gP
- unsteady_[0000000:10:0018153].q3
- unsteady_[0000000:10:0018153].pd3
- unsteady_[0000000:1:0018153].pq3
- unsteady_[0000000:1:0018153].pqp3

Controlled simulation with $St = 0.0425$ and $r = 0.1$

- grid.gS
- grid.gP
- unsteady_[0000000:10:0013000].q3
- unsteady_[0000000:10:0013000].pd3
- unsteady_[0000000:1:0013000].pq3
- unsteady_[0000000:1:0013000].pqp3

Controlled simulation with $St = 0.0425$ and $r = 0.2$

- grid.gS
- grid.gP
- unsteady_[0000000:10:0011480].q3
- unsteady_[0000000:10:0011480].pd3
- unsteady_[0000000:1:0011480].pq3
- unsteady_[0000000:1:0011480].pqp3

Controlled simulation with $St = 0.0425$ and $r = 0.3$

- grid.gS
- grid.gP
- unsteady_[0000000:10:0009140].q3
- unsteady_[0000000:10:0009140].pd3
- unsteady_[0000000:1:0009140].pq3
- unsteady_[0000000:1:0009140].pqp3

Controlled simulation with $St = 0.1275$ and $r = 0.2$

- grid.gS
- grid.gP
- unsteady_[0000000:10:0006890].q3
- unsteady_[0000000:10:0006890].pd3
- unsteady_[0000000:1:0006890].pq3
- unsteady_[0000000:1:0006890].pqp3

Controlled simulation with $St = 0.2550$ and $r = 0.1$

- grid.gS
- grid.gP
- unsteady_[0000000:10:0006110].q3
- unsteady_[0000000:10:0006110].pd3
- unsteady_[0000000:1:0006110].pq3
- unsteady_[0000000:1:0006110].pqp3

Controlled simulation with $St = 2.3$ and $r = 0.44$

- grid.gS
- grid.gP
- unsteady_[0006000:1:0008403].q3
- unsteady_[0006000:1:0008403].pd3
- unsteady_[0006000:1:0008403].pqp3
- unsteady_[0006000:1:0008403].istat3

Controlled simulation with $St = 0.077$ and $r = 0.675$

- grid.gS
- grid.gP
- unsteady_[0000000:10:0005830].q3
- unsteady_[0000000:10:0005830].pd3
- unsteady_[0000000:10:0005830].pqp3
- unsteady_[0000000:10:0005830].istat3

References

[1] Alfredsson, P. H., Örlü, R., Kurian, T., Fransson, J. H. M., Segalini, A., Rüedi, J. -D., and Talamelli, A., "The diagnostic plot - a new way to appraise turbulent boundary-layer data," *Advances in Turbulence XII*, Vol. 132, 2009, pp. 609-612.

[2] Alfredsson, P.H., Örlü, R. and Segalini, A., "A new formulation for the streamwise turbulence intensity distribution in wall-bounded turbulent flows," *European Journal of Mechanics - B/Fluids*, Vol. 36, 2012, pp. 167–175.

[3] Alfredsson, P.H., Segalini, A. and Örlü, R., "A new scaling for the streamwise turbulence intensity in wall-bounded turbulent flows and what it tells us about the outer peak," *Physics of Fluids*, Vol. 23, 041702, 2011.

[4] Anderson, J.D., "Fundamentals of Aerodynamics," third ed., McGraw-Hill, New York, NY, 2001.

[5] Aram, E., Mittal, R. and Cattafesta, L., "Simple Representations of Zero-Net Mass-Flux Jets in Grazing Flow for Flow-Control Simulations," *International Journal of Flow Control*, Vol. 2, No. 2, 2010, pp. 109-125.

[6] Boom, P.D., and Zingg, D.W., "Time-Accurate Flow Simulations Using an Efficient Newton-Krylov Schur Approach with High-Order Temporal and Spatial Discretization," *AIAA Paper* 2013-0383, 2013.

[7] Bruun, H. H., Khan, M. A., Al-Kayiem, H. H., and Fardad, A. A. "Velocity calibration relationshipsfor hot-wire anemometry", *Journal of Physics E: Scientific Instruments*, Vol. 21, 1988, pp. 225232.

[8] Cabrit, O. and Nicoud, F., "Direct simulations for wall modeling of multicomponent reacting compressible turbulent flows," *Physics of Fluids*, Vol. 21, No. 5, 2009, pp.055108.

[9] Cebeci, T., "Analysis of Turbulent Flows with Computer Programs," Elsevier, Waltham, MA, 2013.

[10] Del Rey Fernández, D.C., and Zingg, D.W., "High-Order Compact-Stencil Summation-By-Parts Operators for the Second Derivative with Variable Coefficients," *ICCFD7*, 2012.

[11] Ducros, F., Comte, P. and Lesieur, M., "Large-eddy simulation of transition to turbulence in a boundary layer developing spatially over a flat plate," *Journal of Fluid Mechanics*, Vol. 326, 1996, pp. 1–36.

[12] Erm, L. P. and Joubert, P. N., " Low Reynolds number turbulent boundary layers," *Journal of Fluid Mechanics*, Vol. 230, 1991, pp. 1–44.

[13] Ferziger, J. H. and Peric, M., "Computational Methods for Fluid Dynamics," *Springer*, Berlin, Germany, 2002.

[14] Galbraith, M. and Visbal, M., "Implicit Large Eddy Simulation of low Reynolds number flow past the SD7003 airfoil," *46th AIAA Aerospace Sciences Meeting and Exhibit*, Reno, Nevada, AIAA-2008-225, 2008.

[15] Ganapathisubramani, B., Hutchins, N., Hambleton, W., Longmire, E., and Marusic, I., "Investigation of large-scale coherence in a turbulent boundary layer using two-point correlations," *Journal of Fluid Mechanics*, Vol. 524, 2005, pp. 5780.

[16] Gomit, G., Berger, Z., Ganapathisubramani, B. and Lavoie, P. "Active flow control of a turbulent boundary layer with large-window and stereo-PIV", In *54th AIAA Aerospace Sciences Meeting*, AIAA-2016-1124, 2016.

[17] Hanson, R. E., Buckley, H. P. and Lavoie, P." Aerodynamic optimization of the flat plate leading edge for experimental studies of laminar and transitional boundary layers". *Experiments in Fluids*, Vol. 53 (4), 2012, pp. 863871.

[18] Hanson, R.E. and Ganapathisubramani, B. "Development of turbulent boundary layers past a step change in wall roughness", *Journal of Fluid Mechanics*, Vol. 795, 2016, pp. 494523.

[19] Hicken, J.E., and Zingg, D.W., "A Parallel Newton-Krylov Solver for the Euler Equations Discretized Using Simultaneous Approximation Terms," *AIAA Journal*, Vol. 46, No. 11, 2008, pp. 2773-2786.

[20] Hussain, A. K. M. F. and Reynolds, W. C. "The mechanics of an organized wave in turbulent shear flow", *Journal of Fluid Mechanics*, Vol. 41, 1970, pp. 241258.

[21] Hutchins, N. and Marusic, I. " Evidence of very long meandering features in the logarithmic region of turbulent boundary layers", *Journal of Fluid Mechanics*, Vol. 579, 2007, pp. 128.

[22] Hutchins, N. and Marusic, I. " Large-scale influences in near-wall turbulence", *Royal Society of London Philosophical Transactions Series A*, Vol. 365, 2007, pp. 647664.

[23] Hutchins, N., Nickels, T. B., Marusic, I. and Chong, M. S. "Hot-wire spatial resolution issues in wall-bounded turbulence", *Journal of Fluid Mechanics*, Vol. 635, 2009, pp. 103.

[24] Laurent, H., "Turbulence d'Une Interaction Onde de Choc/Couche Limite sur Une Paroi Adiabatique ou Chauffe," *PhD Thesis*, Université Aix-Marseille II, Marseille, France, May, 1996.

[25] Lund, T. S., Wu, X., and Squires, K. D., "Generation of Turbulent Inflow Data for Spatially-Developing Boundary Layer Simulations," Vol. 140, 1998, pp. 233-258.

[26] Jones, M. B., Marusic, I. and Perry, A. E. "Evolution and structure of sink-flow turbulent boundary layers", *Journal of Fluid Mechanics*, Vol. 428, 2001, pp. 127.

[27] Kennedy, C. A. and Carpenter, M. H., "Addative Runge-Kutta Schemes for Convection-Diffusion-Reaction Equations," *Applied Numerical Mathematics*, Vol. 44, 2003, pp. 139181.

[28] Kinsler, L. E., Frey, A. R., Coppens, A. B. and Sanders, J. V. "Fundamentals of Acoustics, fourth edition" edn. John Wiley and Sons, Inc, 1996

[29] Klebanoff, P. S., Cleveland, W. G. and Tidstrom, K. D. "On the evolution of a turbulent boundary layer induced by a three-dimensional roughness element". *Journal of Fluid Mechanics*, Vol. 237, 1992, pp. 101187.

[30] Miller, I. S., Shah, D. A. and Antonia, R. A. "A constant temperature hot-wire anemometer", *Journal of Physics E: Scientific Instruments*, Vol. 20 (3), 1987, pp. 311.

[31] Naughton, J. W., Robinson, J. and Durgesh, V. "Oil-film interferometry measurement of skin friction analysis summary and description of matlab program", In *Instrumentation in Aerospace Simulation Facilities*, ICIASF-03, 20th International Congress, IEEE, 2003.

[32] Osterlund, J. M., Johansson, A. V., Nagib, H. M. and Hites, M. H. "A note on the overlap region in turbulent boundary layers", *Physics of Fluids*, Vol. 12, 2000, pp. 14.

[33] Osusky, M., Boom, P.D., Del Rey Fernández, D.C., and Zingg, D.W., "An Efficient Newton-Krylov-Schur Parallel Solution Algorithm for the Steady and Unsteady Navier-Stokes Equations," *ICCFD7*, 2012.

[34] Osusky, M., and Zingg, D.W., "Parallel Newton-Krylov-Schur Solver for the Navier-Stokes Equations Discretized Using Summation-By-Parts Operators," *AIAA Journal*, Vol. 51, No. 12, 2013, pp. 2833-2851.

[35] Patel, V.C., "Calibration of the Preston tube and limitations on its use in pressure gradients," *Journal of Fluid Mechanics*, Vol. 23, No. 1, 1965, pp. 185–208.

[36] Rouhi, A., Piomelli, U., and Geurts, B. J., "Dynamic subfilter-scale stress model for large-eddy simulations," *Physical Review Fluids*, Vol. 1, No. 4, 2016, 044401.

[37] Purtell, L. P., Klebanoff, P. S. and Buckley, F. T., "Turbulent Boundary Layer at Low Reynolds Number," *Physics of Fluids*, Vol. 24, No. 5, 1981, pp. 802-811.

[38] Ritos, K., Kokkinakis, I. W., Drikakis, D. and Spottswood, S. M., "Implicit large eddy simulation of acoustic loading in supersonic turbulent boundary layers," *Physics of Fluids*, No. 29, 2017, 046101.

[39] Sagaut, P., Garnier, E., Tromeur, E., Larchevêque, L., and Labourasse, E., "Turbulent Inflow Conditions for Large-Eddy Simulation of Compressible Wall-Bounded Flows," *AIAA Journal*, Vol. 42, No. 3, 2004, pp. 469–477.

[40] Saric, W. S. "Springer Handbook of Experimental Fluid Mechanics", chap. 12, pp. 886896. Berlin-Heidelberg: Springer, 2007.

[41] Sayadi, T., Hamman, C. W. and Moin, P. "Direct numerical simulation of K-type and H-type transitions to turbulence," *Center for Turbulence Research Annual Research Briefs*, 2011.

[42] Sayadi, T., and Moin, P., "Predicting natural transition using large eddy simulation," *Center for Turbulence Research Annual Research Briefs*, 2011, pp. 97–108.

[43] Schlatter, P. "Large-eddy simulation of transition and turbulence in wall-bounded shear flow," *PhD Thesis*, Swiss Federal Institute of Technology, Zürich, Switzerland, 2005.

[44] Schultz, M.P. and Flack, K. A., "Turbulent boundary layers on a systematically varied rough wall," *Physics of Fluids*, Vol. 21, 015104, 2009.

[45] Sekhar, S. and Mansour, N., "Implicit large-eddy simulations of zero-pressure gradient, turbulent boundary layer," *53rd AIAA Aerospace Sciences Meeting*, Kissimmee, Florida, AIAA-2015-1987, 2015.

[46] Spyropoulos, E. T., and Blaisdell, G. A., "Large-Eddy Simulation of a Spatially Evolving Supersonic Turbulent Boundary-Layer Flow," *AIAA Journal*, Vol. 36, No. 11, 1998, pp. 19831990.

[47] Stolz, S., and Adams, N. A., "LES of Supersonic Boundary Layers Using the Approximate Deconvolution Model," *Direct and Large-Eddy Simulation – IV*, Kluwer Academic, Norwell, MA, 2001, pp. 269-276.

[48] Wei, L., "Direct Numerical Simulation of Compressible and Incompressible Wall Bounded Turbulent Flows with Pressure Gradients", *PhD Thesis*, Queen's University, Kingston, ON, Canada, 2009.

[49] Wu, X. and Moin, P., "Direct Numerical Simulation of Turbulence in a Nominally Zero-Pressure-Gradient Flat-Plate Boundary Layer", *Journal of Fluid Mechanics*, Vol. 630, 2009, pp. 5-41.